ABSTRACT

Title of Document: UNDERSTANDING CO OXIDATION IN SOFC'S USING NICKEL PATTERNED ANODE

Bahman Habibzadeh, PhD, 2007

Directed By: Professor, Gregory S. Jackson, Dept. of Mechanical Engineering

The ability of solid oxide fuel cells (SOFC's) to operate with carbonaceous fuels depends on their ability to oxidize CO through direct electrochemical oxidation and/or water-gas-shift reactions with subsequent H_2 electrochemical oxidation. Many recent SOFC studies assume that in porous Ni/YSZ anodes, gaseous CO with H_2O is converted to H_2 through the water-gas-shift reaction and all charge transfer involves H_2. This assumption seems questionable when comparing literature rates of charge transfer for dry CO and H_2 in porous Ni/YSZ anodes. However, electrochemical reaction rates are clouded by transport-controlled, gas-phase concentration gradients and non-electrochemical surface reactions in porous anodes. To eliminate those complicating factors, this study has implemented micro-fabricated, patterned Ni anodes on single crystal YSZ electrolytes to evaluate CO electrochemical oxidation under dry and wet conditions. Electrochemical impedance spectroscopy (EIS) and voltammetry were used to quantify the patterned anode performance. *Ex situ* surface analysis including SEM and Raman spectroscopy were conducted to explore how CO impacted the stability of the Ni microstructure.

Adding ~ 3% H_2O (by mole) to CO/CO_2 anode flows increased electrochemical oxidation rates by almost 2X for temperatures between 700 and 800 °C. This can suggest a role in water gas shift for creating H_2 to increased charge transfer reaction rates. Fitting experimental results from EIS studies with equivalent circuit models elucidates the role of charge transfer activation in high frequency impedance and the impact of surface diffusion and adsorption on low-frequency impedance.

A surface mechanism was developed to predict electrochemical oxidation of CO and H_2 on Ni surface. This mechanism was implemented into a numerical model which integrated the transient governing equations of the patterned anodes and provided a linearization for rapid impedance spectra calculations. Model results, utilizing surface chemistry adapted and modified from the literature, tracked the dependency of current per unit length of three-phase boundary for dry CO and also predicted qualitatively the influence of H_2O on electrochemical oxidation rates with CO feeds. The increase in charge transfer due to H_2O in CO feeds appears to be driven not only by water-gas-shift but also by a reduction in CO_2 and O on the Ni surface caused by the presence of H_2O. Predicted characteristic frequencies for the impedance spectra were too high by an order of magnitude or more. Further assessment with this and other patterned anode studies will be critical for refining the mechanism for CO oxidation on Ni/YSZ anodes and such a refined mechanisms will provide a basis for improved design and operation of porous Ni/YSZ anodes with CO rich streams. This study has provided a basis for continuing development of that mechanism.

UNDERSTANDING THE CO OXIDATION IN SOLID OXIDE FULE CELLS USING NICKEL PATTERNED ANODE

By

Bahman Habibzadeh

Dissertation submitted to the Faculty of the Graduate School of the
University of Maryland, College Park, in partial fulfillment
of the requirements for the degree of
Doctor of Philosophy
2007

Advisory Committee:
Associate Professor Gregory S. Jackson, Chair
Professor Bryan Eichhorn
Professor Ashwani K. Gupta
Associate Professor Kenneth Kiger
Professor Michael Zachariah

To my parents
To whom I am forever grateful
For their unconditional love and support

To my beloved wife, Fatemeh, and
my beautiful daughter, Kimia,
whose presence and love makes everything else
meaningful and worthwhile

Acknowledgements

First and foremost, I would like to immensely thank my advisor Professor Gregory S. Jackson for his support and guidance throughout the preparation of this thesis and my time as a graduate student. He dedicated time and effort, much more than expected to help me learn and succeed. His flexibility, friendliness and encouragement made completing my work at the University of Maryland very pleasant and rewarding. It has truly been an honor to know and work with someone whose masterful knowledge, intelligence, and achievements in science and technology is only completed with his exemplar passion and efforts towards family, humanity, and morality values. He has provided an opportunity and appreciation for learning that I will always carry with me. Once more I thank him for his patience in helping me complete this endeavor.

Also it is my great pleasure to thank my thesis advisory committee: Professor Bryan Eichhorn, whom I was privileged to have his advice on a weekly basis during SOFC group meetings. Professor Ashwani K. Gupta, my M.S. thesis advisor, who was my first mentor in graduate studies. Under his supervision I learnt how to conduct applied research and not get discouraged until the job is done. Professor Kenneth Kiger, who taught me how to be a teacher and guided me through tough stage of teaching with encouragement and patience. Professor Michael Zachariah, whom I have had the honor of having him as one of my committee members to enlighten me with his experiences and fruitful advices.

I would also like to thank my colleagues at The Center for Fuel Cell Research *Dr.* Mary Sukeshini, Benjamin P. Becker, Steven C. DeCaluwe and Dr. Seyed Abdolreza

S. Reihani for their contributions to this work. Dr. Sukeshini was always willing to explain the physics associated with fuel cells and help interpret electrochemical data. Ben Becker shared the work of constructing and running experiments. Steven DeCaluwe supported me in developing my model. And Dr Seyed Reihani was always there to help in understanding the analytical concepts in heterogeneous reactions.

Thanks go to my colleagues at the Biochemistry Department: Oktay Demerican, Mike Pomfret , Prof. Bryan Eichhorn and Prof. Rob Walker. Oktay Demircan provided the materials and procedure necessary for cathode fabrication and assisted in analysis of XRD data. Mike Pomfret operated the Raman spectrometer on post-experimental patterned anodes and helped interpret the results.

Thanks to my friend at Reacting Flow laboratory, Tom McGrath, Roxanna Sai, Fletcher Robbins, Jason McGill, Eric Shields, Joshua Pearlman, Douglas Crane, Joseph Plaia, Atul Bharga, Paul Jawlik and Young Kyong Jo.

I wish to thank Tom Loughran and Jon Hummel who deposited many Ni coatings and shared their expertise in photolithographic techniques, John Barry, Nolan Ballew for their help in sputtering Ni coatings and finally Tim Maugel for operating the SEM and EDX instrument.

Above all, I am especially grateful to my kind and loving family for their love, warmth, support, and patience throughout all my endeavors. My parents who bore, raised, and selflessly loved me as the youngest member of the kind, united, and successful family that they raised. My eldest sisters Raziyeh and Mehraneh, and my brother Mohammad whom I learnt from as my school teachers at my early years of education and I continue to do so in life. And my other siblings Marzieh, Akbar, and Maryam whose kindness and love I have always had with me.

I would also like to extend my respect and appreciation to my sisters-in-law and most especially to the memory of my late mother and father in law, Akhtar Bahri and Mirgholam, Mir Rashed, whose exemplar passion, sacrifice, and support towards higher education of their children was truly inspirational.

And lastly, but most importantly, I wish to express my gratitude to my lovely wife, Fatemeh, whose vision and endless help, support, and encouragement gave me the ability to pursue and complete my graduate studies. She with whom I share the joyful happiness of our most beautiful and precious gift of heaven, *Kimia.* It is to her and to my parents that I dedicate this work.

Table of Contents

List of Tables

List of Figures

Nomenclature

	Description	Unit
Variables		
a_{cat}	area of catalyst per unit volume	1/cm
a_{elec}	area of electrolyte per unit volume	1/cm
D	diffusion constant	m^2/s
F	Faraday's constant (= 96485)	C/gmol
i	current density per unit area of electrode or electrolyte	Amp/cm^2
i^0	exchange current density per unit area or per unit length	
k	rate constant	
l_{TPB}	length of three-phase boundary per unit volume	$1/cm^2$
n	gmol of electrons	
P	total pressure	kPa
p_k	partial pressure of species k	bar
$\overline{R}$	universal gas constant (= 8.3415)	J/gmol*K
R_{bulk}	bulk area specific resistance associated with electrolyte ion transport	$\Omega*cm^2$
R_{pol}	polarization area specific resistance for an electrode	$\Omega*cm^2$
$\dot{s}_k$	surface rate of formation per unit of surface area	$gmol/cm^3*s$
T	temperature	°C, K
V_{cell}	electric potential difference across fuel cell	V
V_{OCV}	open circuit potential difference across fuel cell	V
$\dot{w}$	power density per unit area of electrode or electrolyte	W/cm^2
w	width	mm
Z	impedance	Ω
Greek		
α	charge transfer coefficient	
γ	sticking coefficient	
η	overpotential	mV
σ	ionic or electronic conductivity	S/cm
σ	occupied site	
χ	measure of fit goodness	
β	charge transfer coefficient	
ω	relaxation frequency	Hz
$\dot{\omega}_k$	gas phase rate of formation per unit of gas phase volume	$gmol/cm^3*s$
ν	stoichiometric factor	
Γ	surface site density	$gmol/cm^2$
θ	fraction of surface sites	
Subscripts		
a, anode	anode	
c, cath	cathode	
cell	MEA assembly	

f	forward	
i	for reaction i	
k	for species k	
mem	Membrane	
r	reverse	

1. Introduction

1.1. Introduction to Solid Oxide Fuel Cells

Fuel cells are electrochemical devices that directly convert fuel chemical energy to electricity. William R. Grove (1881-1896) first demonstrated a fuel cell using a proton conducting fuel cell with a dilute sulfuric acid electrolyte in 1839 [1]. However, the first solid oxide fuel cell was built in 1937 by Baur and Preis [2], who recognized that some oxides can be used as electrolytes to conduct oxygen ions, O^{2-}, while preventing free electron conduction. The O^{2-} flux from the cathode to the anode is used to oxidize a fuel stream on the anode catalyst and establish a voltage across the cell which drives free electrons from the anode reaction through an external circuit for energy production which was the first solid oxide fuel cell. These principle of the SOFC are illustrated Figure 1.1.

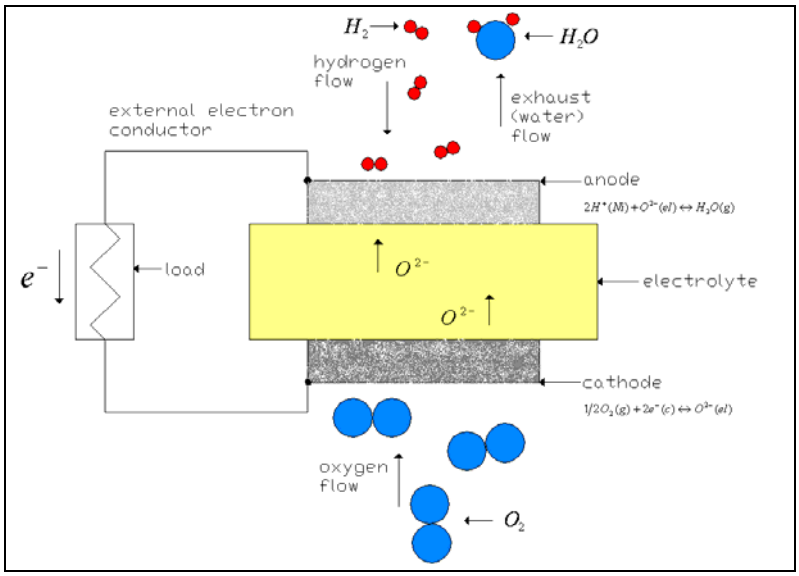

Figure 1.1 – Schematic of a solid oxide fuel cell showing O_2 reduction, O^{2-} flow through the electrolyte membrane, and H_2 as fuel

Figure1.1 shows the major components of a single cell SOFC membrane electrode assembly (MEA): notably the anode, the cathode, and the electrolyte. Typically the anode and cathode are porous matrices with mixtures of electronic-conducting catalysts and O^{2-} conducting electrolyte material to encourage the half reaction at both electrodes. The global half reaction happening at each electrode for three typical fuels and oxygen as oxidant can be written as below [3].

Anode Half Reactions:

$$H_2 + O^{2-}_{el(b)} \leftrightarrow H_2O + 2e^- \quad \text{(R.1.1)}$$

$$CO + O^{2-}_{el(b)} \leftrightarrow CO_2 + 2e^- \quad \text{(R. 1.2)}$$

$$CH_4 + 4\,O^{2-}_{el(b)} \leftrightarrow CO_2 + 2H_2O + 8e^- \quad \text{(R. 1.3)}$$

Cathode Half Reaction:

$$O_2 + 2e^- \leftrightarrow 2\,O^{2-}_{el(b)} \quad \text{(R. 1.4)}$$

O_2 molecules adsorb dissociatively on the cathode catalyst in the SOFC before undergoing a charge transfer reaction in which they change phases from the cathode catalyst surface to the electrolyte surface [4-6]. When current is drawn from the cell, the resulting O^{2-} ions move into the solid oxide electrolyte across to the anode. At the anode, the fuel (H_2, CO, or other fuel species) adsorbs on the electrode catalyst and reacts at the electrolyte/catalyst/gas interface, known as the three-phase boundary (TPB), to produce fuel oxidation products and two electrons per O^{2-} ion reacted. The difference in oxygen chemical potential at the cathode and the anode establishes a voltage drop V_{cell} between the cathode and the anode according to equation 1.1.

$$V_{cell} = \frac{\overline{R}T}{nF} \ln\left(\frac{p_{O_2,Cathode}}{p_{O_2,Anode}} \right) \quad \text{(Eq. 1.1)}$$

where p_{O2} is the partial pressure of O_2 in bars, n is the moles of electrons produced per mole of O_2 reduced (= 4), and F is Faraday's constant. V_{cell} can be used to drive electrons from the anode through an electric circuit to the cathode for useful work and further production of O^{2-} ions.

Optimal SOFC performance is measured by the cell voltage V_{cell} and the current density i per unit area of electrolyte. Several important material requirements must be satisfied for good cell performance as listed here:

- proper electronic and O^{2-} conductivities for anode, cathode, electrolyte and any connecting interlayers,
- adequate gas transport to the electrolyte/electrode interfaces,
- thermo-mechanical and structural stability under operating conditions,
- minimal reactivity and inter-diffusion between the phases.

These requirements have lead to a wide array of materials being used for anodes and cathodes. For the anode, the most commonly implemented materials to date are nickel metal catalyst mixed in a porous cermet with yttria-stabilized zirconia (YSZ). Typically, this porous Ni/YSZ anode is fairly thick (500-1000 μm) in order to provide structural support. While the cathode materials are more varied, one of the most common materials is the electron-conduction ceramic LSM (strontium-doped lanthanum manganate) mixed with YSZ in a thin porous cathode (< 50 μm).

SOFC's provide many advantages over other energy conversion systems: high energy conversion efficiency, potential for fuel flexibility, very low levels of NO_x emissions, scalable plant design, and potentially long lifetime relative to other fuel cells due to the elimination of corrosive liquids. However, outstanding challenges in SOFC development remain – including high-temperature sealing, durability, and operability. High operating temperatures are needed because the O^{2-} conductivity of current YSZ electrolytes falls off rapidly with temperature $T < 700$ °C. At high T, sealing and chemical stability of multicomponent electrodes become a real challenge [7-9]. Improved mechanical stability and compatibility of the materials at these temperatures is an area of significant research [10-12].

Recent developments in SOFC design have focused significantly on lowering operating temperature, reducing the costs of materials and fabrication, and extending the operating life cycle of the cells. These efforts are aimed on (1) decreasing electrolyte resistance by production of thin YSZ electrolytes or more conductive CeO_2 or gallate-based electrolytes and (2) increasing electrode O_2 reduction activity using improved mixed conductors such as LSC and/or optimizing electrode microstructure. [13]. More recently increased focus has been given to new anode material systems and designs for developing stable designs for direct utilization of hydrocarbon fuels in SOFC's [14-16]. This latter area has in part motivated the work presented in the current study.

1.2. SOFC Materials

Like all other fuel cells, the name "solid oxide fuel cell" indicates the nature of the electrolyte, a solid oxide-ion-conducting ceramic. This ceramic must conduct O^{2-} ions through its bulk phase without conducting significant amount of electrons. The conduction and associated V_{cell} is driven by external O_2 chemical potential differences across the electrolyte, and the two electrodes on each side of the electrolyte must be good at creating (cathode) and destroying (anode) the O^{2-} ions in order to maintain the flux and chemical potential difference. More detail specification about the SOFC's materials is in the following sections.

1.2.1 SOFC Electrolytes

As stated before, the SOFC electrolyte must be a good O^{2-} conductor without being a good electronic conductor. It also must be stable in both reducing (anode-side) and oxidizing (cathode-side) environments. In addition to the chemical and electrochemical properties, the electrolytes must be easily and cost-effectively fabricated into thin and strong films and gas tight structure..

To date, stabilized Zirconia (ZrO_2), primarily Yttria-Stabilized Zirconia (YSZ), with fluorite structure has been widely used as an electrolyte for SOFC's being developed in industry. The fluorite structure can be stabilized by doping with divalent or trivalent cations such as Yttrium. O^{2-} conduction is provided by oxide vacancies and interstitial oxide ions. In a pure compound, the intrinsic defects are fixed by thermodynamic equilibrium, while extrinsic defects are established by the

presence of dopants [2]. The O^{2-} conductivity σ_{O2-} for YSZ (in S/cm) can be estimated by the following equation [17].:

$$\sigma_{O2-} = \frac{36000}{T} \exp\left(-\frac{83910}{\overline{R}T}\right) \qquad \text{(Eq. 1.2)}$$

At this value, a typical electrolyte membrane thickness of 10 μm will have area specific resistances of 0.148, 0.053, and 0.023 Ω*cm^2 of electrolyte at 600, 700, and 800 °C respectively. Since it is desirous for high power densities to keep area specific resistances << 0.1 Ω*cm^2, this explains why YSZ electrolytes of typical thicknesses require operating temperatures > 700 °C. In addition to the good O^{2-} conductivity, electrolytes must have good thermomechanical properties such as matching coefficient of thermal expansion (CTE) with electrodes or inter-layers (active layers placed between porous electrodes and the dense electrolytes).

Although YSZ is the SOFC electrolyte used in most industrially developed cells and in this study, other fluorite structured oxide ion conductors, such as doped ceria, have also been developed as the electrolyte materials for SOFC's, especially for reduced temperatures operations. The temperature dependence of several O^{2-} conductivity for several oxides has been reported in the literature [2], and several oxides have higher conductivity than YSZ. For instant, Bismuth oxide mixtures and some other oxides show as much as an order of magnitude higher conductivity than YSZ < 800 °C. However some disadvantages, such as electronic conductivity, high cost, or difficulties in processing, still make YSZ among the most common electrolyte in SOFC's. Nonetheless, there are many research programs seeking new stable material systems that can work at lower *T* and replace YSZ.

1.2.2 SOFC Cathode Materials

For high power density performance, SOFC must meet the following criteria:

- high activity for O_2 reduction to O^{2-}
- stable in an oxidizing environment and high temperatures
- high electronic conductivity
- matching CTE with SOFC electrolytes

SOFC developers have focused on semi-conductor materials for cathodes. Strontium-doped lanthanum manganate, $La_{1-x}Sr_xMnO_{3-\delta}$ (LSM), is a commonly used perovskite material for cathode electrolcatalyst. LSM has an acceptable electronic conductivity of 80 S/cm at 800°C [18] and is stable in oxidizing environments even above 1100 ºC. Increasing the strontium dopant level *x* up to 0.5 increases cathode electronic conductivity [19]. In general to provide adequate O^{2-} conductivity in LSM cathodes, the LSM is mixed with YSZ in a porous matrix (as in this study) because LSM has limited bulk phase O^{2-} conductivity. Adjustment of mixture stoichiometry and powder characteristics must be met to yield a CTE and porosity that match other cell components. A typically accepted level of porosity for cathodes is 30% [18].

The reactivity of LSM for O_2 reduction has been well characterized and although it has good reactivity at high temperatures [20], the high activation energy barrier for the O_2 reduction on LSM means that reaction rates fall off rapidly with decreasing temperature. There has been a great development in recent years on producing higher activity cathode materials and materials which provide mixed electronic/ionic conduction such as strontium-doped lanthanum cobaltate (LSC). The mixed ionic

conductivity will mitigate the need for high temperatures because YSZ is no longer needed to bring the O^{2-} ions into the bulk phase electrolyte [21]. Long-term durability and chemical stability of other cathode materials is still being optimized.

1.2.3 SOFC Anode Materials

The most common anode material system used for SOFC's is porous Ni/YSZ cermets. Ni/YSZ cermets provide low cost, relatively good chemically stability in reducing atmospheres at high temperatures, and compatible CTE's with dense YSZ-electrolytes. Ni provides the electronic conductivity and high catalyst activity for electrochemical oxidation of H_2 and CO. YSZ provides the ionic conductivity to bring O^{2-} ions into contact with the Ni electrocatalyst. The charge transfer resistance of Ni/YSZ cermets can be made low with appropriate microstructure. Because anodes are typically made thick (500 – 1000 μm), porosities ≥ 30% are needed to permit transport of gas-phase reactants and products through the anode structure. Various methods involving co-processing of YSZ and NiO powder followed by an NiO reduction step have been developed to make these cermet anodes [22].

The movement toward developing SOFC's that run on direct hydrocarbon feeds has led to the search for alternative anode materials since hydrocarbon feeds in Ni-based anodes lead to carbon deposition and electrocatalyst deposition at SOFC operating temperatures [23]. For hydrocarbons specially for methane, ceria-based anodes, such as Cu/CeO_2 cermets [22], have been developed and show a tendency to minimize carbon deposition and provide long-term stable performance. Other anode materials have also been explored and a few of those materials systems are listed in the Table 1.1

Table 1.1 – Some anode material systems tested for SOFC operation.

#	Material	Name	Fuel	Reference
1	$CuO–ZrO_2$	copper stabilized-zirconia	-	[10]
2	$Sr_{0.88}Y_{0.08}TiO_{3-\delta}$(YST) and (YSZ)	-	H_2 and Methane	[24]
3	$Sc_{0.15}Y_{0.05}Zr_{0.62}Ti_{0.18}O_{1.9}$ (ScYZT)	Oxide ScYZT	5% H_2 in Ar	[25]
4	MoS_2 , CoS, FeS, NiS	metal sulfides	H_2S-Air	[26]
5	CeO_2-doped Ni/Al_2O_3	-	ethane/ propane	[16]
6	-	Cu-Co Bimetallic	Methane	[27]
7	$La_{0.8}Sr_{0.2}CrO_{3-\delta}$ $LaCr_{0.95}Ru_{0.05}O_{3-\delta}$ $La_{0.8}Sr_{0.2}Cr_{0.8}Mn_{0.2}O_{3-\delta}$	Doped Lanthanum Chromites	H_2 and Methane	[28]

Despite the variety of materials being explored as anode for the SOFC's as listed in Table 1.1, Ni/YSZ and slight variations on this system remain the primary anode for most SOFC applications in industry. For many systems requiring operation with hydrocarbons, pre-reforming reactors or anode barrier layers that promote internal reforming [29] are implemented to alleviate the carbon deposition problem. Under such operating conditions, the effectiveness of the SOFC anode will depend primarily on its ability to promote electrochemical oxidation of the reformate products (H_2 and CO). These operating conditions motivate the current study of such oxidation processes on well-characterized Ni anodes.

The fuel diversity in SOFC systems in particular to allow for direct utilization of hydrocarbons [15, 30-35] for small power (< 100 kW) applications requires high power density and stable operation without carbon build-up or sulfur poisoning. This has pushed anode material research and further characterization of conventional Ni-based anodes. Direct hydrocarbons feeds makes SOFC's to be among the highest

power densities power generation. There is variety of fuels that have been applied in laboratory or practically as fuel in SOFC's including methane (or natural gas) [14, 15, 36-39], ethane [16], propane [16, 39, 40], small alcohols [32, 41, 42], biomass fuels [33, 43, 44] and H_2S [45, 46]. Some studies have explored direct feeds of heavy hydrocarbons like jet fuels or crude oil [34].

In general, anode development has focused on ways to avoid carbon build up on the electrocatalyst surface. Although some report a positive effect of deposited carbon on porous anodes [47, 48], accumulation of carbon deposits will prevent the long-term stability of the fuel cell. One way of controlling the carbon build up at the anode surface is injecting steam into the fuel flow. Steam to carbon ratios ≥ 2 are typically recommended for preventing carbon formation in Ni-based catalyst systems [49, 50], but utilization of barrier layers or other microstructures can be used to reduced this steam requirement by relying on H_2O produced from the electrochemical oxidation processes [29]. Either way, the importance of understanding the electrochemical oxidation of H_2 and CO on Ni becomes critical for developing a better understanding of anode operation with hydrocarbon feeds.

1.3. Electrochemical Oxidation in SOFC Anodes

The nature of the electrochemical oxidation of fuel species – either through direct or indirect (via internal reforming) means – remains a topic of discussion in the literature. To assess the importance of internal reforming of hydrocarbons for successful SOFC implementation, a more complete understanding of the electrochemical oxidation for reformate species (H_2 and CO) must first be

established. While significant research has tried to establish an understanding of H_2 and CO electrochemical oxidation on preferred anode materials such as Ni/YSZ, only recently has research begun to develop a quantitative description of the complex processes involved in the electrochemical oxidation of H_2 and to a lesser extent CO [51-53]. This section will discuss the basic level of understanding on electrochemical oxidation in SOFC anodes of these simple fuel molecules.

The electrochemical (or charge transfer) reactions in SOFC's are known to take place at the regions that three phases – electrode, electrolyte, and gas – meet each other. This region is known as three phase boundary (TPB). Figure 1.2 illustrates the H_2 electrochemical oxidation at an SOFC TPB.

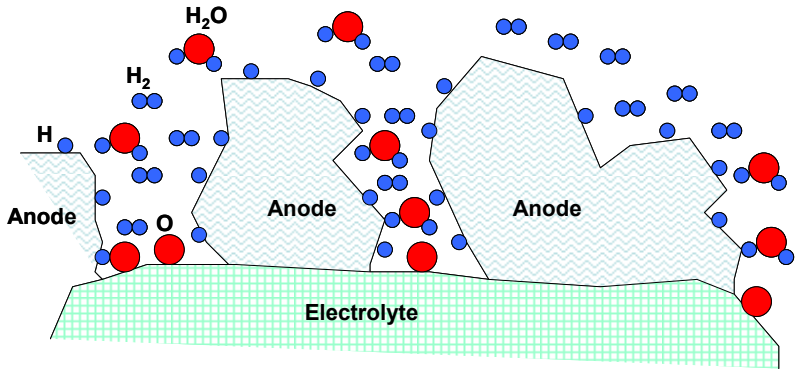

Figure 1.2 – H_2 electrochemical oxidation at an SOFC three phase boundary

The charge transfer happens when a charged species is transferred from one phase to another. In general, the two phases have a voltage difference between them established by a double layer of charge at the solid interface between them. In SOFC's, because gaseous products must be evolved after electrochemical oxidation of the fuel, the charge transfer processes must occur at the TPB where there is gas phase access for the evolved products.

However, the electrochemical oxidation process involves many other steps which may impact electrochemical reaction rates. These steps are listed here:

On the anode electrocatalyst surface

- mass transport of gaseous fuel to electrochemically active region of porous anode
- adsorption of fuel species onto electrocatalyst
- surface diffusion of active adsorbate species to the TPB region
- desorption (if necessary) of any electrocatalyst-adsorbed oxidation products

On the electrolyte surface near the anode

- O^{2-} transport from the bulk of the electrolyte up to the electrolyte surface
- surface diffusion (if necessary) of ionic species to the TPB region
- desorption (if necessary) of any electrolyte-adsorbed oxidation products

At the three-phase boundary

- charge transfer reactions releasing electrons into the electrocatalyst bulk

Using H_2 as a reference fuel, the schematic Figure 1.3 shows some of the above steps in a proposed mechanism for H_2 electrochemical oxidation at a Ni/YSZ three-phase boundary interface. Figure 1.3 provides a visualization of how steps other than the charge transfer reaction step may actually impact the actual rate of current generation.

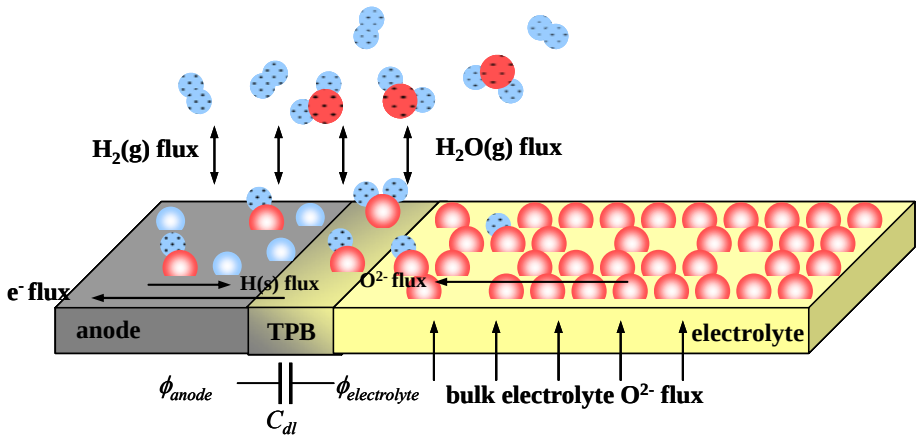

Figure 1.3 – Illustration of processes involved in H_2 electrochemical oxidation at an SOFC TPB.

In general, increasing the TPB length per unit volume l_{TPB} increases charge transfer reaction rates, and thus the current generated. To increase l_{TPB} in porous electrodes, electrolyte material will be mixed with catalyst material in the porous electrode structure. If the electrocatalyst is a metal, the mixed phases will form a porous cermet material which is fabricated to enhance the diffusion of O^{2-} ions into or out of the electrode. In the anode, gas diffusion of the fuel molecule through the pores is also required and can limit the high current densities for thick cermet anode structures. Fabrication of the cermet anodes must be done carefully such that it not only offers enough pores for diffusion of the fuel, but also adequate O^{2-} transport through the electrochemically active region of the anode, which has been estimated to be 10 – 20 μm [53, 54] thick from the dense electrolyte/porous anode interface.

The development of porous anodes has continued evolved in recent year in order to implement direct utilization of hydrocarbons in SOFC's [55]. For Ni/YSZ anodes, the amount of carbon atoms in the fuel can seriously reduce V_{cell} from thermodynamic expectations and overall conversion efficiency. Currently, for long-term operation,

most developers have preferred to use hydrocarbons in SOFC's in conjunction with an external reformer (with partial oxidation and/or steam reforming) [49, 56]. This is because of the lack of durability of most fuel catalysts under conditions where carbon build-up can occur. Improved knowledge of the fundamental electrochemistry and physics within the porous electrocatalyst layers may assist in optimizing porous anode microstructures to minimize surface carbon build-up. For Ni-based anodes, internal steam reforming has been used to prevent carbon deposits at the anode [49, 50, 57-59], but more recently efforts have been ongoing to develop architectures with so-called diffusion barrier layers to enhance steam concentrations in Ni anodes from internally produced H_2O and it is being suggested that all of the steam necessary for reforming may be obtained from the electrochemical reactions themselves[29, 60].

H_2 and CO are the principal fuel-derived products from steam reforming (internal or external to the SOFC) and/or partial oxidation (from an upstream reactor). Thus, H_2 and CO are the likely fuel species participating in the fuel oxidation in the electrochemically active region of SOFC anodes. Numerous on electrodes using Ni as well as Au or Pt instead of Ni have shown that CO (and in some cases CH_4) have much lower electrochemical reaction rates than H_2 [61-63]. Some have shown that CO and CH_4 are less electrochemically active than H_2 even with 12% H_2O in the anode flow [64]. These issues are discussed further in subsequent chapters.

Mizusaki et al. [4, 65] studied H_2 electrochemical oxidation on well-defined Ni anodes with YSZ electrolytes to experimentally reveal the pathway of H_2 reaction in SOFC anodes. By changing p_{H2} and p_{H2O} in their anode feeds, they explored the dependence of H_2 electrochemical oxidation. They proposed a stepwise

chemical/electrochemical reaction for H_2 on Ni anode and suggested that rate limiting steps are O^{2-} spillover from YSZ to the Ni surface and/or surface diffusion of the O^{2-} ions on the YSZ surface. Later, De Boer [66] and Bieberle [67] explored alternative reaction steps to understand measured impedances and voltage-current curves. Bieberle proposed a single charge-step reaction process involving H^+ spillover onto YSZ followed by reactions with 2 OH^- to form an O^{2-} ion and an H_2O molecule which desorbs from the YSZ surface. Bessler [68] applied a computational approach to explore Bieberle's reaction mechanism and his result was in good agreement with Bieberle. However, more recent studies by Bessler et al. [51] give strong evidence that the proposed O^{2-} charge transfer step by Mizusaki et al does not properly capture the p_{H2} and p_{H2O} dependence. Rather, H^+ spillover from the Ni surface onto YSZ with a two-step charge transfer process, as indicated here, best captures the p_{H2} and p_{H2O} dependence observed by Mizusaki et al. [4, 65] and De Boer [66] . This recent advance in understanding electrochemical oxidation of H_2 on Ni/YSZ electrodes will be explained further in detail in chapters 4, and a modified version of this mechanism [69] will be implemented as part of a model in this study.

CO electrochemical oxidation is not as well understood as that of H_2, even though several investigations of CO reactions in SOFC anodes have been performed either with CO as the only fuel [70-74] or with CO mixed with other fuel species [62, 75-77]. Holtappels et al. [78] were amongst the first researchers to study pure CO electrochemical oxidation on Ni/YSZ anodes. Although no stepwise electrochemical mechanism for CO oxidation was provided, results indicated that the overall reaction rate is more than one order of magnitude slower than H_2. To avoid the complications

with Ni anodes, Mizusaki et al.[71] tried a range of temperatures and CO partial pressures on porous Pt/YSZ electrode. They concluded from their experiments that the charge transfer reaction step at the TPB was rate-limiting as opposed to adsorption, desorption, or surface diffusion. Matsuzaki and Yasuda [75] have done a wide range of experiments on Ni/YSZ electrodes with H_2, H_2O, CO and CO_2 at different *T*. They concluded that electrochemical oxidation of H_2 is only 2-3X faster than of CO, and in contrast to Mizusaki et al. explained that the lower rates of CO electrochemical oxidation were caused by mass transfer. Weber et al. [70] reported unstable reactions for pure CO electrochemical oxidation due to carbon deposition and micro-structural changes within the anode, although it was unclear whether these results could be generalized.

Probably the most comprehensive study on CO electrochemical oxidation to date has been performed by Lauvstad et al. [72, 73], who suggested four different models of electrochemical reaction of CO on Pt and Ni surfaces. They arranged a series of experiments changing p_{CO} and p_{CO2} and temperatures to explore the validity of the different proposed mechanisms. In contrast to the other studies, Lauvstad et al. concluded that CO adsorption and CO_2 desorption are like rate limiting at high temperatures. Costa-Nunes et al.[62] compared two different anodes including one Ni/YSZ anode operating with H_2, CO and syngas. In agreement with Lauvstad et al. they concluded that for Ni/YSZ anodes, charge transfer cannot be a rate limiting step but rather adsorption and desorption control the rate of CO electrochemical oxidation.

The disagreement in the understanding of electrochemical oxidation of CO suggests that there is not a clear consensus on the mechanisms. There are also some

difficulties in utilizing CO with Ni anodes under some conditions where carbon deposition due to the Boudouard reaction [79, 80] may occur:

$$2CO_{Ni} \rightarrow CO_2 + C_{Ni} + []_{Ni} \quad \text{(R. 1.5)}$$

When steam is added to a CO-rich stream, there is additional uncertainty as to the role of water-gas-shift reactions, reaction 1.6, transitioning the fuel from CO to H_2.

$$CO + H_2O \rightarrow CO_2 + H_2 \quad \text{(R. 1.6)}$$

While some researchers have utilized models that assume water-gas shift completely transforms the CO to H_2 before electrochemical oxidation [53], but if the electrochemical oxidation rates are no more than 2-3X faster for H_2 [75], such an assumption seems questionable. A major focus of this study is to provide a clear understanding of CO oxidation on dense Ni anode by experiments and modeling.

1.4. Patterned Anodes for Exploring SOFC Chemistry

To isolate surface chemistry and diffusion processes from gas-phase transport, thin-film pattern anodes [4, 5, 66] have been employed. These patterned anodes, first introduced by Mizusaki et al. [4], provide well-controlled geometries as well such that quantification of rates from experimental measurements. The patterns are usually densely deposited films of electrocatalyst metals such as Ni, which are microfabricated using photolithography in order to provide the well-characterized geometries for the electrochemical kinetic studies.

Since charge transfer reaction occurs at TPB of the catalyst, electrolyte and gas phase, it is useful to know parameters such as electrocatalyst surface area per unit volume a_{cat}, electrolyte area per unit volume a_{elec}, and length of three-phase boundary per unit volume l_{tpb}. However, quantifying these parameters in porous cermet anodes

is difficult and this combined with the complications of the gas-phase transport make conventional porous anodes non-ideal for quantifying electrochemical oxidation rates. This limitation has led to the use of various types of electrodes including patterned anodes [81-83] and micro-point electrodes [73] where parameters like a_{cat}, a_{elec}, and l_{TPB} can be readily estimated.

Mizusaki et al.[4, 65] have investigated the kinetics of H_2-H_2O reaction at the nickel pattern anodes on YSZ electrolyte substrate using platinum as their cathode and reference electrode. They made a set of Ni patterns of width 5μm to 100 μm in area of 7 mm diameter on 8% mole YSZ single crystal disks of 1.0 mm thickness and 1 cm^2 area. They changed the p_{H2} from 0.25 to 19 kPa and partial pressure of p_{H2O} from 0.25 to 1.7 kPa. To avoid Ni oxidation, the ratio of p_{H2O}/ p_{H2} was kept < 10. They observed a change in resistance of Ni with time until Ni grain growth is stabilized in the pattern. By changing the YSZ spacing they didn't notice of any resistance variation, and thus, they suggested that there is no dependency to the open YSZ area. They then suggested that controlling reactions happen on the Ni surface near the TPB. A comparison of proposed mechanisms for H_2 electrochemical reaction suggested that the critical step in H_2/H_2O electrochemistry is the removal of adsorbed H_{Ni} by reactions with O^{2-} ions spilling over to the Ni surface.

De Boer [66] also studied the H_2 oxidation on Ni patterned anodes on YSZ electrolytes. He has used 4 mm thick polycrystalline YSZ disk and Pt paste cathodes the voltammetry and impedance measurements were used to investigate the effect of TPB and anode area on the electrochemical oxidation rates as a function of p_{H2} and p_{H2O}. In this work, conductivities associated with the currents per overpotential

scaled with the l_{TPB}, but the observed p_{H2} and p_{H2O} could not be reconciled with the results of Mizusaki [83].

Bieberle et al. [5, 84] have experimented Ni patterns on single crystal 9.5% mole YSZ disk, 0.5 mm thick. They performed a wide range of experiments on variation of p_{H2O} and temperature. Unlike Mizusaki [4], two semi-circle arcs were observed in the impedance vs. frequency curves. Beiberle et al. suggested that the electrode process consists of at least three potential rate-limiting processes depending on conditions, but surface diffusion on the Ni or YSZ was not considered one of them. Comparing the activation energy of H_2 adsorption with that value from the literature they suggested that the main impedance arc in the impedance spectra might be related to H_2 adsorption. Finally they suggested an stepwise reaction of hydrogen at the interface of patterned nickel and YSZ surface such that H_2 dissociatively adsorbs on the Ni surface and then each hydrogen atom after losing one electron jump on the YSZ surface and produce OH^-, and in two steps, OH^- turns to be adsorbed H_2O on the YSZ surface and consequently these water molecule desorbs from the YSZ surface. A major focus of the program for this research has been to expand the Ni patterned anode research to explore electrochemical oxidation of fuels other than H_2 [85, 86].

1.5. Objectives of Thesis

The numerous efforts to sustain direct utilization of hydrocarbons in SOFC's have indicated that conventional Ni/YSZ SOFC anodes are prone to uncontrolled carbon deposition under conditions for dry hydrocarbon feeds, particularly for species with multiple carbon atoms[87]. With the addition of steam and/or O_2 in a hydrocarbon feed, a porous Ni/YSZ anode matrix can provide catalytic internal reforming and

thereby convert some, if not all, of the hydrocarbon to H_2 and CO either through steam reforming or partial oxidation [34, 88]. Internal reforming reactions have been shown to work well under some conditions even with dry feed and diffusion barriers at alleviating carbon deposition in conventional Ni/YSZ anodes [29, 70, 89, 90]. Nonetheless, it remains an outstanding question as to whether internal reforming can be sustained such that otherwise unacceptable Ni/YSZ anodes may be viable with some carbonaceous fuels. Reforming of hydrocarbons in SOFC's or even in upstream reactors suggests the importance of electrochemical oxidation of H_2 and CO mixtures [75, 76, 91] for understanding the performance of SOFC's even with hydrocarbon feeds as well as with other feeds such as coal gas which provide H_2 and CO directly. In this study, to remove the complexity of the porous anode and for limiting the effects of geometry, the Ni patterned anode is the strategy to investigate the electrochemical reaction of H_2 and CO as fuel in SOFC's.

The first question that this research is trying to answer is to investigate the dependency of the charge transfer to the available TPB. Although this has been weakly shown by other researchers [65, 84] for electrochemical reaction of H_2, still there is room for double check those results. Also check if the exact same result holds for CO. The most important questions are yet to be answered include:

- On what phase do the surface species adsorb/desorb?
- What is the effect of surface diffusion on reaction rates?
- What are the specific charge transfer reactions?

To answer to these questions the outline is a primary objective of this research.

An outline of the thesis can be seen in the flowchart in Figure 1.4. The first step is to design a set of patterned anode experiments that can isolate the key reactions in electrochemical oxidation of the fuel (principally CO here). The patterned anode results will provide key dependency relationships that will elucidate the charge transfer and detailed surface chemistry in all SOFC anodes (Ni/YSZ here). The experimental interpretations will be compared with results from a state-space model of the patterned anode surfaces as shown in chapter 6.

A descriptive outline of this thesis shows how the objectives were addressed. Chapter 2 explains the experimental set-up for the patterned anode experiments. Chapter 3 discusses some of the experimental methods and challenges in implementing patterned anodes and focuses on the obstacles on preparing the MEA, designed experiments, and all efforts which has been done on characterization of the patterns. Chapter 4 focuses on some initial experiments with patterned anodes studying H_2 electrochemical oxidation on patterned Ni anodes to compare with past studies discussed in this chapter. Chapter 5 focuses on experiments involving CO electrochemical oxidation on patterned anodes under both dry and humidified conditions. Chapter 6 describes the development of a numerical model with detailed surface chemistry to assess rate-limiting processes in CO electrochemical oxidation on the patterned anodes. Finally, chapter 7 summarizes the results of this dissertation and provides recommendation on how further research can help to further our understanding of fundamental electrochemical oxidation in SOFC's and how it can be used to improve future SOFC microstructure design.

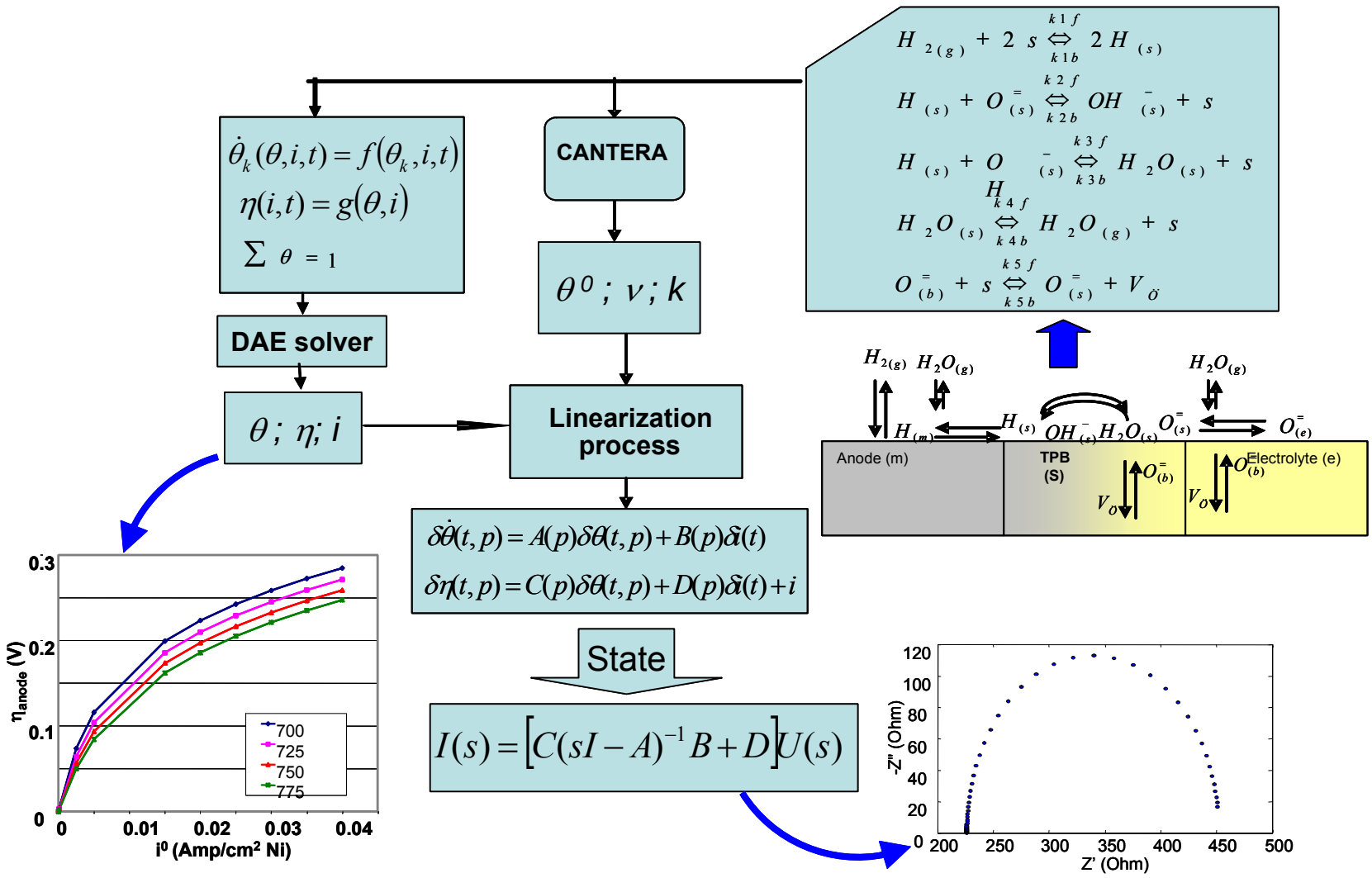

Figure 1.4 – A visual diagram showing the steps of the research program in this dissertation.

2. Experimental Setup

To characterize the electrochemical oxidation of H_2 and/or CO on Ni/YSZ anodes for a wide range or conditions, microfabricated Ni patterned anodes were fabricated on single crystal YSZ electrolyte discs. The YSZ discs were ~ 1 mm thick and thereby provided a support for the entire assembly. To minimize the effect of the cathode on the electrochemical measurement, a high-surface-area porous LSM/YSZ cathode was deposited on the counter side of the electrolyte disc. In the experimental set-up described here, the electrolyte disc was used to support four independent patterned anodes, which were tested simultaneously under typical SOFC temperatures for various fuel compositions. The four patterns provided both a means to explore simultaneously anode geometry effects on electrochemical oxidation rates and impedances and also the multiple electrodes provided redundancy for measurements in case an electrode film failed during set-up or operation. Both electrochemical impedance spectroscopy (EIS) and linear voltammetry measurements were implemented as described in this chapter. The following sections further describe the fabrication process, the experimental setup, and the experimental procedures.

2.1. MEA Fabrication Assembly

2.1.1. Electrolyte and Cathode Fabrication

SOFC MEA's must be supported by having one element – either anode, cathode, or electrolyte – adequately thick enough to maintain structural integrity. The choice of the supporting component greatly influences the MEA performance as well as the

fabrication process. Usually the thick component will support the other components which will be deposited as very thin films. There are different methods of depositions being used by researchers but most thin-film depositions will fall under one of the following methods:

- physical coating with a paste [64] or colloidal suspension[37]
- tape casting [92] or centrifugal casting [93]
- DC sputtering [86]
- ionized cluster beam [65]

In this research, all the experiments done were electrolyte supported. High surface area porous LSM/YSZ was used for the cathodes and thin-film microfabricated Ni patterns were used as anodes. The electrolyte support was a fully dense 9 % mole yttria ($(Y_2O_3)_{0.09}(ZrO_2)_{0.91}$) with orientation of 100 (from MTI Corporation). These electrolytes were ordered in 1"x1" square size and thickness of 1 mm and one sided polish for the best adhesion of the deposited nickel at the polished side and slurry-coated LSM/YSZ at the rough side.

The porous LSM/YSZ cathodes were fabricated on the non-polished side of the single crystal YSZ electrolyte to provide good adherence between the dense electrolyte and the porous electrode. The cathode material was a mixture of 50% (by weight) LSM ($La_{0.85}Sr_{0.15}MnO_{3-\delta}$) and 50% YSZ ($(Y_2O_3)_{0.08}(ZrO_2)_{0.92}$) and preparation followed a previously described approach in the literature [94]. The exact recipe of preparation and treatment of the cathode is presented in a previous reference [77]. After mixing the LSM/YSZ with the adequate binder and pore former, the cathode material comes out as a jet black liquid with viscosity comparable to that of

vegetable oil. As the volatile binder material evaporates upon exposure to air, the cathode materials turns into a gooey paste less than one minute. The method of applying the cathode mixture on rough side of the single crystal YSZ disc is similar to tape casting. A section of Kapton tape with a centered 12 mm diameter hole was placed on the electrolyte and the cathode material was painted cast onto the electrolyte to fill this center hole and then scraped off to be approximately the thickness of the Kapton tape which approximately is 50 μm. After cathode material was dried in the air, the tape template is removed and the cathode was ready to be sintered. The cathode sintering process was done in air with an initial temperature ramp from 25 ˚C to 400 ˚C at 0.3 ˚C/min, a hold for 1 hr at 400 ˚C, a second ramp from 400 ˚C to 1300 ˚C at 3.0 ˚C/min, and a hold at 1300 ˚C for 1 hr before a cool-down to 25 ˚C at a rate of 3.0 ˚C/min. 99.9% pure platinum gauze of 52 mesh woven from 0.1mm (0.004in) diameter (Alfa Aesar) was cut to cover the cathode surface as a current collector and was attached to the surface by platinum paste. A 99.9% pure platinum wire of 0.25 diameter was attached to the platinum mesh as current collector for the cathode.

2.1.2. Patterned Anode Fabrication

To deposit Ni on the anode side of the YSZ electrolyte support, the smooth side of the electrolyte was cleaned of particles and organics by acetone and plasma etching. This smooth-polished side was found by profilometry to have a roughness of approximately 0.5 nm before deposition of the Ni film for the patterns. The Ni films were deposited on this polished side to increase the probability of creating a sharp, quantifiable TPB with the photolithographic fabrication process described here. A Ni

film was sputter-deposited as indicated in Table 2.1 to 1.0 μm thickness which was found to be the optimal thickness for maintaining film integrity and adhesion on the YSZ surface [77]. It was shown by testing a range of thickness of deposited anode that 1 μm thickness provides continuity and a surface free of pores and cracks after undergoing electrochemical and temperature cycles up to 800 °C. The plasma etching and sputtering was done via DC magnetron sputtering (AJA International, ATC 1800-V). The parameters of plasma etching and sputtering processes used to produce the anode coatings of the MEA's are listed in Table 2.1.

Table 2.1 – Plasma etching and magnetron sputtering process parameters used to produce nickel coatings

Parameter	Unit	RF Plasma Etching	DC Magnetron Sputtering
Power	W	20	200
Film Growth Rate	nm/min	–	11.3
DC bias	V	170	–
Chamber Pressure	mTorr	30	5
Bath Gas	sccm of N_2	20	20
Time	min	5	100
Working Distance	mm	111	111

After Ni was deposited on the polished side of the YSZ disk, a set of geometrically well-defined patterns were etched out of them by photolithography process. Detail of this process are provided by Becker [77]. First, a photoresist (Microposit S1813, Rohm and Haas) was brought to room temperature then coated on the Ni surface using a spin coater (Headway Research Inc.) at 40,000 rev/min for 40 seconds. The resist was soft-baked on a hot plate at 90 ˚C for 1 min. The cell was cooled back to room temperature and then placed in a mask aligner (MJB3 Mask Aligner, Karl Suss) and brought into contact with a chrome-patterned-on-glass mask

(Microtronics) having our desired anode geometry. Ultra-violet light (365 nm, 8 mW/cm^2) was exposed over the mask for 12 s, exposing the portions of the photoresist to be washed away. The cell was submerged in CD-30 for approximately 1 min to wash away all the exposed resist. The cell was then hard baked at 110 ˚C for at least 2 hrs before the excess Ni was etched away. A nitric acid based etch (Type TFB, Transene Company, Inc.) was poured into a beaker and heated on a hot plate to 55 ˚C. The cell was submerged in the acid for typically 2-5 min until the excess nickel was completely etched away. The remaining photoresist was removed by rinsing in acetone, ethanol, methanol, and distilled water. The time periods for UV light exposure and submersion in CD-30 and the acid bath were optimized to prevent significant over-etching or under-etching of the desired Ni patterns.

Each MEA assembly carried four independent Ni patterns, each with parallel Ni lines with widths generally of 10, 20, 50 and/or 100 μm. The number of lines ranged from 10 to 100 depending on what geometric variation was being pursued in a given set of experiments. These patterns were often used to establish equal Ni surface area a_{cat} and varying l_{TPB} or with equal l_{TPB} and varying a_{cat}. The area of the electrolyte a_{elec} was determined by the spacing between the Ni lines (with exposed electrolyte) and the equivalent of one electrolyte disc thickness around the pattern perimeter which was calculated to be an integral averaged area that contributed to the electrolyte resistance for each pattern.

The schematic in Figure 2.1 and a picture of the MEA assembly in Figure 2.2 show examples of the patterned anode designs. Both Figures show a set of patterned electrodes with equal l_{TPB} and varying a_{cat}. Figure 2.2 shows the entire Ni patterned

anode on the MEA. The cathode on the opposite side of the electrolyte can be seen through the translucent (single crystal) electrolyte.

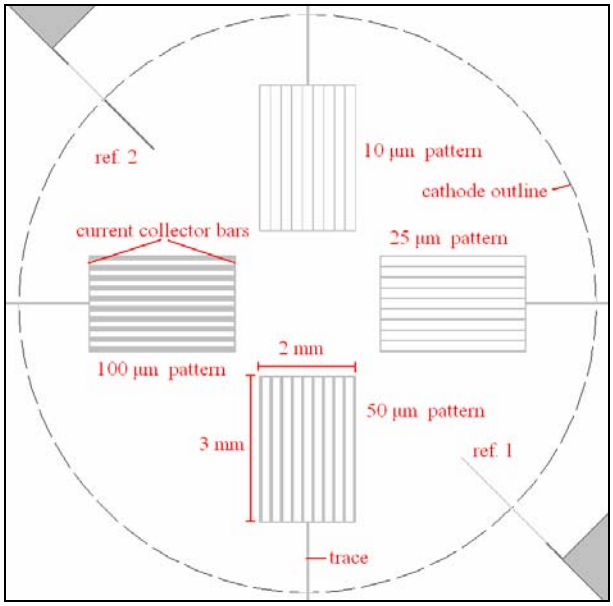

Figure 2.1 – Schematic of the patterns with equal l_{TPB} and varying a_{cat}, is showing Group B from the Table 2.2

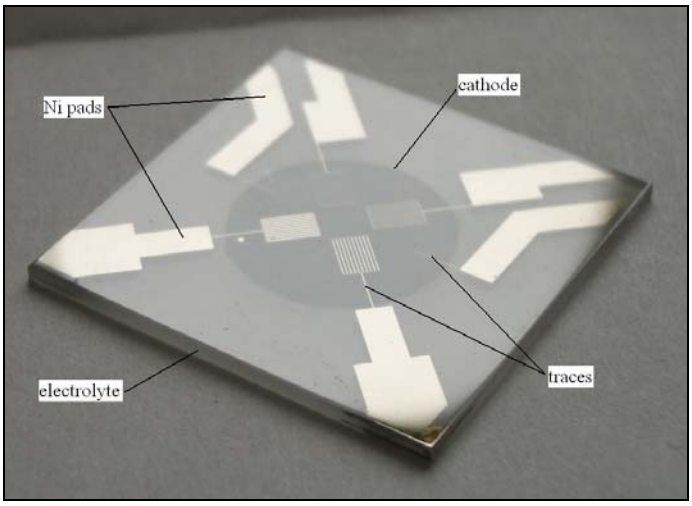

Figure 2.2 – A representative MEA with four Ni patterned anodes. The dark circle in the center is the cathode on the opposite side of the translucent electrolyte disc.

For a better understanding of the geometry of the patterns, Table 2.2 provides detailed information on the prepared Ni patterned anodes. Figure 2.3 clarifies

different variables in Table 2.2. In the result part of this dissertation, the naming group numbers showing in the Table 2.2 will be used to show the correspondence results taken under different pattern geometry combination.

Table 2.2 – Geometric properties of different simultaneous pattern groups explored in this study of the patterns in new mask geometry

	Group A				Group B			
Nickel width – δ_{Ni} (μm)	10	25	50	100	10	25	50	100
# of Ni lines	50	20	10	5	10	10	10	10
YSZ gap width δ_{YSZ} (mm)	0.039	0.092	0.167	0.250	0.211	0.194	0.167	0.111
electrolyte area - a_{elec} (mm^2)	20.0	20.0	20.0	20.0	20.0	20.0	20.0	20.0
Nickel area – a_{cat} (mm^2)	1.95	1.77	1.72	1.69	0.556	0.991	1.720	3.160
TPB length - l_{TPB} (mm)	298	124	65.2	35.2	66.0	65.7	65.2	64.2

	Group C				Group D			
Nickel width – δ_{Ni} (μm)	10	20	50	100	100	100	100	100
# of Ni lines	100	50	20	10	10	10	10	10
YSZ gap width δ_{YSZ} (mm)	0.05	0.05	0.05	0.05	0.111	0.111	0.111	0.333
electrolyte area - a_{elec} (mm^2)	39.8	27.3	19.8	17.3	20.0	20.0	20.0	30.0
Nickel area – a_{cat} (mm^2)	4.10	3.55	3.22	3.11	3.160	3.160	3.160	3.370
TPB length - l_{TPB} (mm)	602	302	122	62	64.2	64.2	64.2	72.2

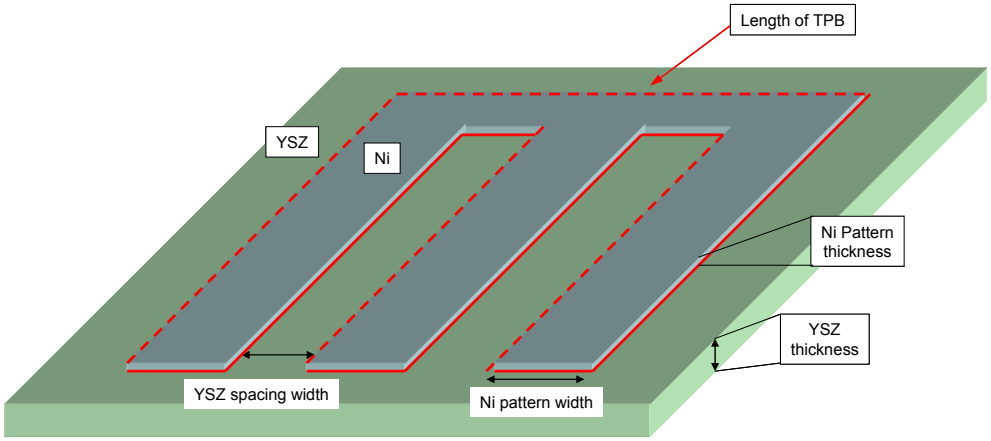

Figure 2.3 – Schematic geometry of Ni pattern to show each parameter in Table 2.2

To evaluate the patterned anode fabrication and assist in interpreting the electrochemical measurements, characterization of the patterned anodes and the

electrolyte surface was undertaken with both pre- and post-experimental microscopy and surface spectroscopy. Characterization tools employed in this study included: 1) optical microscopy, 2) SEM (scanning electron microscopy), 3) EDX (energy dispersive spectroscopy), 4) XRD (X-ray diffraction), and 5) Raman spectroscopy. Results from these characterization techniques are presented in subsequent chapters.

2.2. Experimental Setup

To establish an experimental testing procedure for the patterned anode MEA's, significant effort was applied to establishing not only a reliable fabrication protocol for the MEA but also a repeatable experimental configuration for meaningful measurements. The fragile and expensive YSZ-electrolyte supports required significant care during both fabrication and experiments to ensure that the YSZ disk did not crack either due to temperature shocks or excessive uneven pressure. These challenges were complicated by the fact that the MEA must be mounted inside a high-temperature furnace with sealing on the anode side to ensure that the fuel flow did not leak out into the furnace and cause unwanted gas phase reactions with the air inside the furnace.

The first attempted rig designs were set-up to provide optical access to the patterned anodes but these rigs were prone to unwanted gas leaks at the optical window seals. An alternative design involving optical access through the fuel tube was built, but the stress on the electrolyte-supported MEA's in these rigs did not provide reliability to achieve good measurements. This led toward a simpler rig

which did not attempt to have optical access to the patterned anodes. Optical access was achieved in another set-up at the University of Maryland in a parallel study [95].

The simpler rig design consisted of two sets of concentric alumina tubing mounted together on each side of the electrolyte disc. The inner tubes were the feeds for the cathode air and the anode fuel feed respectively. The outer tube was pasted with ceramic paste to the single crystal YSZ disc as shown in the schematic of Figure 2.4. The ceramic paste (Ultra-Temp 516 from Aremco Products, Inc.) was picked because of its high-temperature durability and it provided a good CTE ($7.4*10^{-6}$/°C) close to that of alumina ($7.4\text{-}8.2*10^{-6}$/°C) and only slight less than that of YSZ ($10\text{-}11*10^{-6}$/°C).

All experimental results presented were taken from the so-called compression rig represented by Figure 2.5. The final version of the rig eliminated the ceramic paste and relied on spring-loading with mica seals at the tube electrolyte interface. Details of this compression rig design and its assembly are described further here.

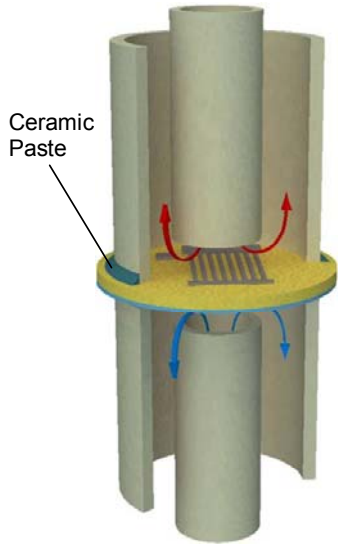

Figure 2.4 – Schematic of the simplified design of rig demonstrating the outer alumina tube pasted to the YSZ single crystal

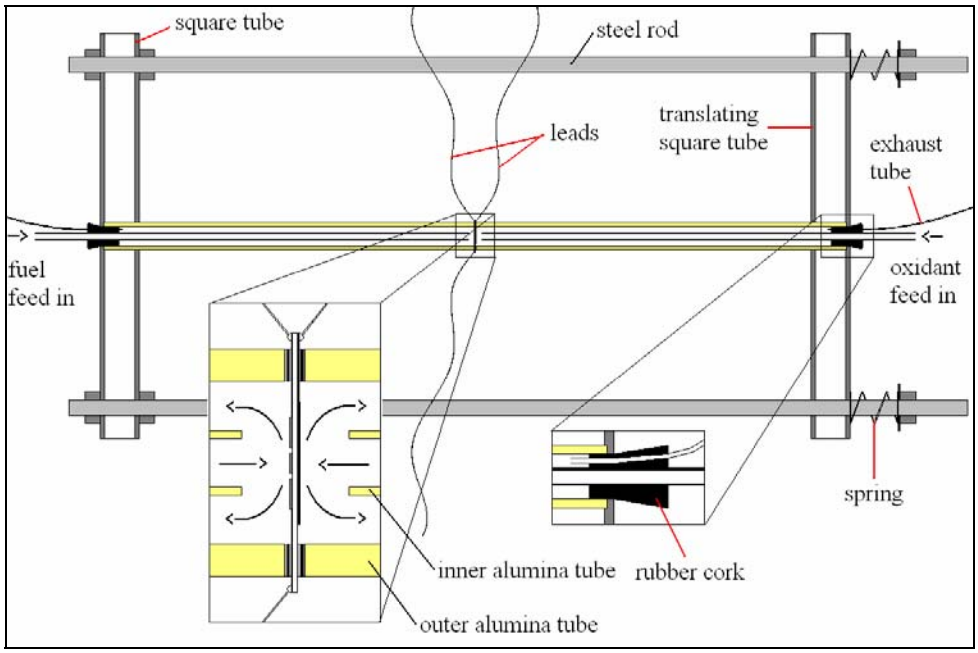

Figure 2.5 – Schematic of compression rig with inset of MEA and rubber cork.

For the anode, gold wires from the electronic current collector were insulated using small ceramic tubes (Ceramic TC Insulators, Omega Engineering) inside the furnace and PTFE tubing outside of the furnace. At the interface with the disk, the gold leads were flattened to minimize leakage under the outer alumina tube. Layers of circular glass (Borosilicate glass filter, Cole-Parmer Instrument Company) and mica (muscovite mica, McMaster Carr) gaskets were attached to the both anode and cathode sides of the electrolyte using high temperature ceramic paste. Figures 2.6 and 2.7 show the layouts as used in the compression rig. An unshielded K-type thermocouple (0.25 mm diameter, Omega Engineering), was pasted with the ceramic paste to the side of the disc. This thermocouple was used to control the furnace and thus the MEA temperature.

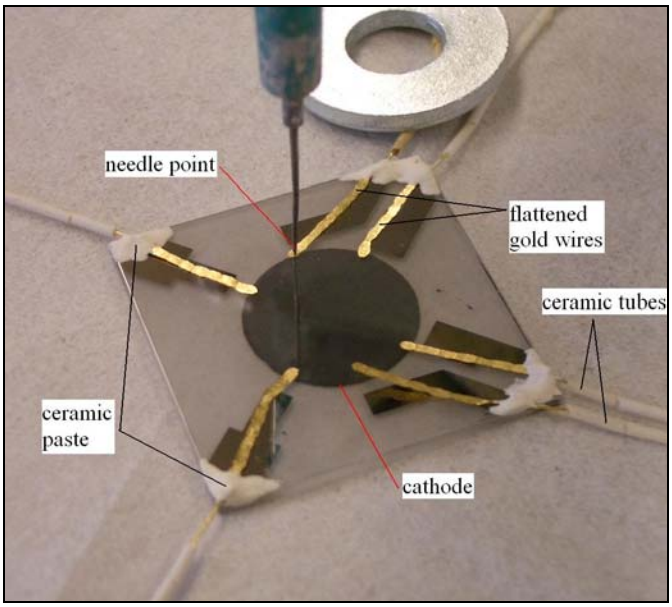

Figure 2.6 – Attachment of gold leads to patterns and reference electrodes via ceramic paste at the anode side of MEA

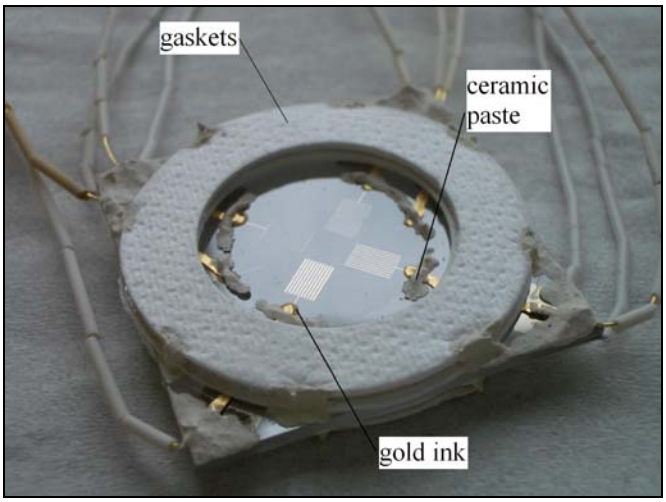

.

Figure 2.7 – Leads and gaskets arrangement on the patterned anode MEA

A fully wired MEA was placed between two fully dense cast alumina tubes (AC Technologies, Inc.) as it can be seen in Figure 2.8. The alumina tubes were supported by a furnace vertically and by the compression rig horizontally. The springs of the rig provided the force that pushed together by spring load the way it is shown in Figure

2.9. The MEA and gasket assembly was compressed between these two outer alumina tubes; a compressive force of 2 lbf distributed over the tube / gasket interface was sufficient to preventing leaks. This force was applied by means of tightening two bolts to compress two sets of springs. As the alumina tubes expand during heat up the square tube translates such that the external springs are additionally compressed thereby preventing excessive loading of the MEA and subsequent fracture.

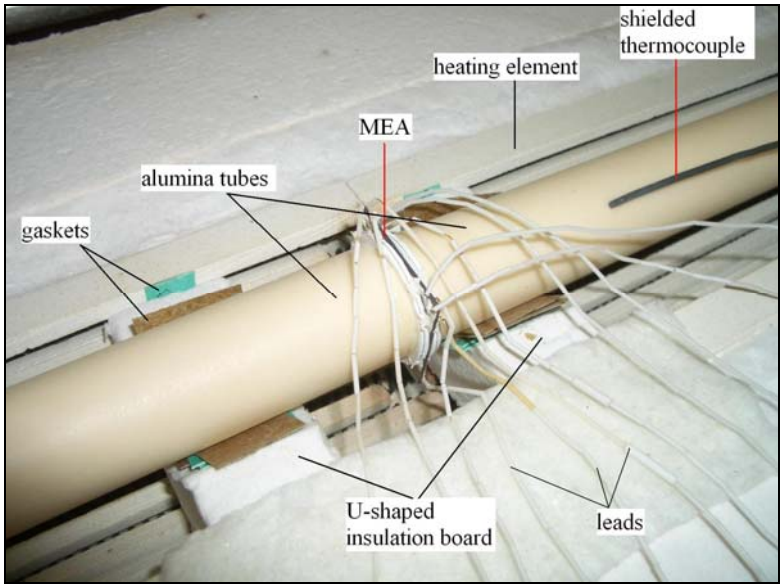

Figure 2.8 – Picture of a MEA and alumina tubes separated by gaskets and supported by the furnace.

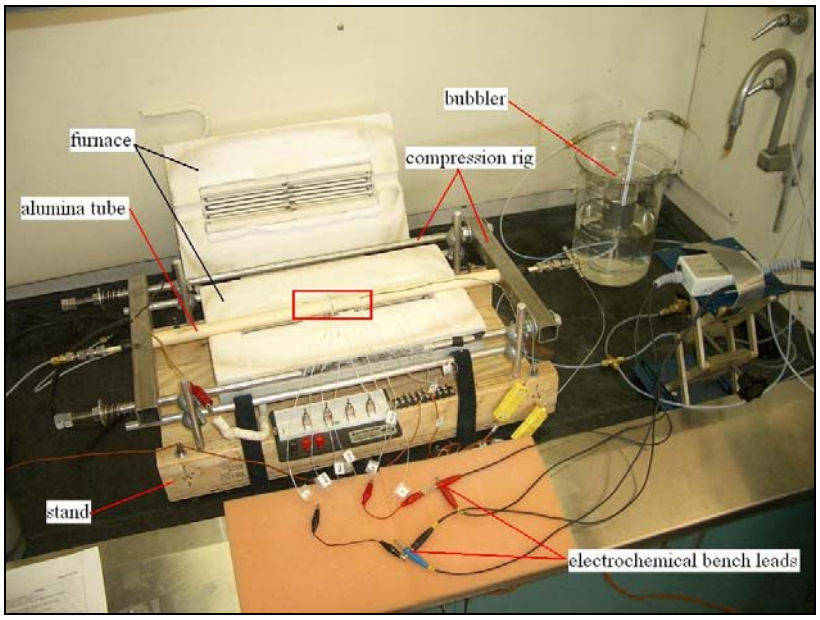

Figure 2.9 – The furnace fixed on a wooden structure and spring loaded rig supported by the furnace.

The outer alumina tubes were 30.5 cm long with an OD = 22.2 mm and ID = 15.9 mm. Outside the furnace the ends of the outer tubes were sealed from the atmosphere using a rubber cork. An inner alumina tube (OD = 6.3 mm, ID = 4.8 mm, length = 35.5 cm) was positioned inside the outer tube to deliver the fuel feed to the anode and the oxidant feed to the cathode. The inner tubes were passed through a hole in each rubber cork and were positioned 5 mm away from their respective electrodes. These inner tubes were also supported by a star shape machined ceramic bracket to assure to be concentric with the outer tubes and to force the impinging feed flow to the outer edges of the MEA. After impinging on the electrodes the exhaust gases were vented to the atmosphere in PTFE tubes that passed through each rubber cork.

2.3. Electrochemical Measurements

After having the rig set up the next step is setup of the flows, measurements instrumentations and data acquisition systems. Figure 2.10 shows a schematic of the experimental setup including the fuel and oxidizer tubing, bubbler, test rig, furnace, electrochemical bench and data acquisition system. The temperature of the cell was controlled by a thermocouple attached to the MEA surface and was used as the furnace controller input temperature. In all the experiments the temperature were raised from the room temperature to the desired temperature with a slope of 1 °C/min. Also the experimental gases were directed from compressed bottles through PTFE tubing to appropriately designed mass flow controllers (MFC's – 5850E's from Brooks Instrument). MFC's regulated the flow of fuels and argon to the anode and one other regulated the flow of air, as oxidant gas, to the cathode. A water bubbler was placed in a bypass line to provide saturated flow for portions of the experiment with the wet fuel flow. The bubbler and a mercury thermometer were partially submerged in a beaker which provided the temperature of water at around 25 ºC for all experiments to ensure the 2.5 – 3.0% humidity in the flow gas.

The signals to and from mass flow controllers and thermocouples were handled by two data acquisition boards (SCXI 1102 Thermocouple Amplifier, National Instruments and a PCI-6034 multifunction I/O board, National Instruments). Labview software controlled the MFC's and read the MFC and thermocouple outputs. Two electrochemical measurement techniques were used in this electrochemical impedance spectroscopy (EIS) and linear sweep voltammetry. The electrochemical

data was collected by an electrochemical bench (Gamry MultEchem™) with both a potentiostat and a frequency response analyzer (FRA).

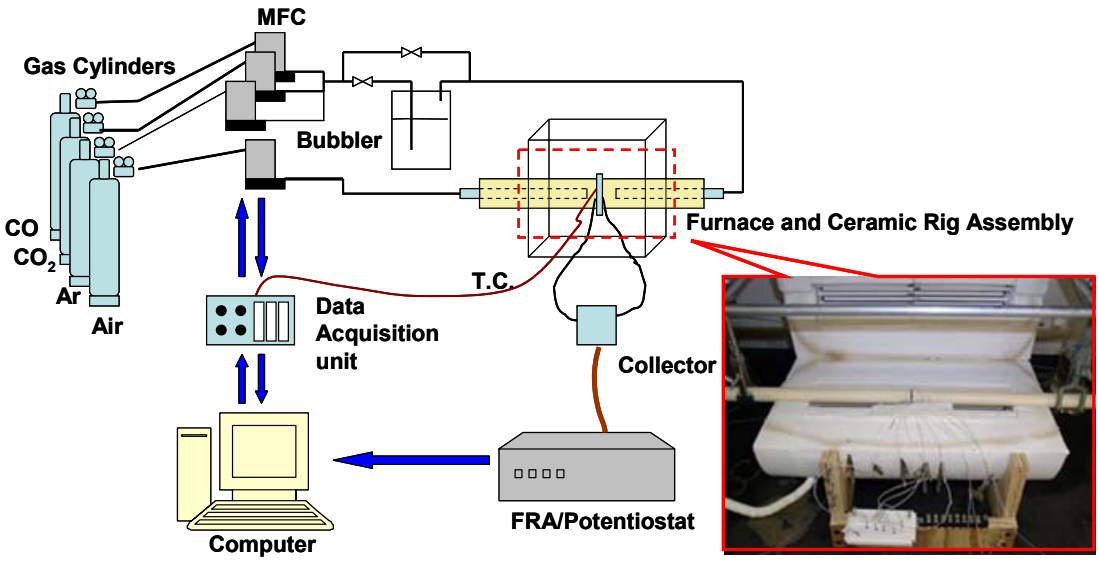

Figure 2.10 – Schematic of the SOFC experimental setup showing measurement system.

2.3.1. Impedance Spectroscopy Measurements

Electrochemical Impedance Spectroscopy (EIS) is a very useful tool to study a possible electrochemical pathway of reaction steps, particularly when EIS data is fit to equivalent circuit models. Electrochemical impedance is usually measured by applying a small excitation AC signal to an electrochemical cell and measuring the current through the cell. Suppose that a sinusoidal potential excitation is applied to the cell, the response to this potential is an AC current signal containing the excitation frequency and it's harmonics. The excitation signal is small so that the cell's response can be considered linear. In a linear system, the current response to a sinusoidal potential will be a sinusoid at the same frequency but shifted in phase.

The excitation signal which is a function of time can be shown in form of $V(t) = V_0 + V_1 \cos(\omega t)$ with V_1 as the magnitude of an oscillatory excitation at radial frequency ω superimposed over the baseline steady voltage V_0. The current response $I(t) = I_0 + I_1 \cos(\omega t - \phi)$ is used with Ohm's law to determine the impedance of a system can be calculated:

$$Z = \frac{V_1 \cos(\omega t)}{I_1 \cos(\omega t - \phi)} = Z_0 \frac{\cos(\omega t)}{\cos(\omega t - \phi)}. \qquad \text{(Eq. 2.1)}$$

Using Euler relationship one can write the excitation voltage and response current in form of $V_1 \exp(j\omega t)$ and $I_1 \exp(j\omega t - j\phi)$ that in turn the impedance equation would be in form of:

$$Z = \frac{V}{I} = Z_0 \exp(j\phi) = Z_0(\cos\phi + j\sin\phi) \qquad \text{(Eq. 2.2)}$$

By plotting the applied sinusoidal signal on the x-axis of a graph and the sinusoidal response signal $I(t)$ on the y-axis, will have an oval shape plot known as a "Lissajous figure" [96]. Analysis of Lissajous figures on oscilloscope screens was the accepted method of impedance measurement prior to the availability of lock-in amplifiers and FRA's.

In potentiostatic electrochemical measurement, the input is the potential and the output is the current. Electrochemical cell is not linear, however an electrochemical system can be considered linear when small enough portion of a cell's current versus voltage curve is considered. In normal EIS experiment, a small (1 to 10 mV) AC signal is applied to the cell. If the system is non-linear, the current response will contain harmonics of the excitation frequency. Linear systems should not generate harmonics, so the presence or absence of significant harmonic response allows one to

determine the system's linearity. In the current study only linear response measurements were made and the excitation voltage was assumed to be adequately small to only produce linear responses.

Often, an equivalent circuit model which fits the data will suggest some chemical model, process, or mechanism which can be proposed and tested. EIS data and the equivalent circuit model have been studied [96, 97] over years and the provided data are useful tool to think about the electrochemical problem.

EIS data is commonly analyzed by fitting it to an equivalent electrical circuit model. Most of the circuit elements in the model are common electrical elements such as resistors, capacitors, and inductors. To be useful, the elements in the model should have a basis in the physical electrochemistry of the system. As an example, most models contain a resistor that models the cell's electrolyte resistance. Table 2.3 shows the elements that are used in an equivalent circuit fitting in this study.

Table 2.3 – Major components for fitting equivalent circuits used in this study.

Symbol	Element	Impedance	Admittance
R	Resistance	R	$1/R$
C	Capacitance	$1/(j\omega C)$	$j\omega C$
L	Inductance	$j\omega L$	$1/(j\omega L)$
Q	Constant Phase Element (CPE)	$1/(Y_{\circ} j\omega)^{n}$	$(Y_{\circ} j\omega)^{n}$

2.3.2. Voltammetry

Linear sweep voltammetry is a general term applied to any voltammetric method in which the potential applied to the working electrode is varied linearly in time. The value of the scan rate may be varied depending to the nature of the study. In this research the rate was 10 mV/s or lower. That is an useful method to study the amount

of the electrical energy are obtained from a fuel cell when a reasonably current is drawn, but the actual cell potential is decreased from its equilibrium potential because of irreversible losses incorporated with the anode, cathode, electrolyte, concentration, interlayers and electrical connectors. The losses are often called polarization or overpotential. These overpotentials can be categorized in three types of irreversibility including activation polarization, ohmic polarization and concentration polarization. These losses make the cell voltage to be less than its ideal potential. Equation 2.3 gives the overall cell voltage equation showing the overpotential losses on both the anode and the cathode side η_a and η_{cath} due to activation of the charge transfer reaction η_{act} and due to concentration losses from mass transport η_{conc}.

$$V_{cell} = V_{OCV} - \eta_{conc,an} - \eta_{act,an} - \eta_{conc,cath} - \eta_{act,cath} - \eta_{ohmic} \qquad \text{(Eq. 2.3)}$$

In Equation 2.3, V_{OCV} is the ideal open circuit voltage (or Nernst potential) and can be calculated from the equation 2.4 if the gases are assumed to be ideal as generally true in SOFC environments.

$$V_{OCV} = \frac{-\Delta G^0_{reac}}{nF} + \frac{RT}{nF}\ln\left(\prod_k p_k^{-\nu_k}\right) \qquad \text{(Eq. 2.4)}$$

in which ΔG^0_{reac} is the change in free energy due to the electrochemical reaction when all species are at P^0 , n is number of electron in the charge transfer process, F is Faraday's constant, and ν_k are the stoichiometric coefficients for the reactants and products. For H_2 electrochemical oxidation, Equation 2.4 gives the following expression for V_{OCV}:

$$V_{OCV} = \frac{\mu^0_{H2,a} + 0.5\mu^0_{O2,c} - \mu^0_{H2O,a}}{2F} + \frac{RT}{2F}\ln\left(\frac{p_{H2,a}p^{1/2}_{O2,c}}{p_{H2O,a}}\right) \qquad \text{(Eq. 2.5)}$$

The V_{OCV} can also be calculated from the equilibrium p_{O2} at the anode as listed in Table 2.4 by employing Eq 1.1 as reiterated here.

$$V_{OCV} = \frac{RT}{nF} \ln\left(\frac{p_{O_2,Cathode}}{p_{O_2,Anode}} \right) \quad \text{(Eq. 1.1)}$$

p_{H2O} in the anode side of the SOFC plays a major role in open circuit voltage. The observed V_{OCV} of the H_2/H_2O is listed in the Table 2.4 [98]:

Table 2.4 – Effect of humidity on V_{OCV} for H_2 fuel on Ni or Pt anode at SOFC

p_{H2} (bar)	p_{H2O} (bar)	equilibrium p_{O2} (bar) at anode	V_{OCV} (V)
100	0	1.62×10^{-16}	1.270
99.14	0.86	2.87×10^{-14}	1.128
98	2	1.65×10^{-13}	1.080

When current is flowed through the SOFC, the various overpotentials began to drop the realized voltage from the reversible V_{OCV} value. Activation polarization is directly related to the rates of electrochemical reactions. There is a close similarity between electrochemical and chemical reactions in that both involve an activation barrier that must be overcome by the reacting species. General equations for the activation overpotential is shown in Equation 2.5 provides an implicit equation using a modified Butler-Volmer equation that can be solved to get η_{act} for each electrode

$$i = i^0 \left[\exp\left(\frac{\beta_f nF\eta_{act}}{\overline{RT}} \right) - \exp\left(-\frac{\beta_r nF\eta_{act}}{\overline{RT}} \right) \right] \quad \text{(Eq. 2.6)}$$

in which β_f and β_r are fitted forward and reverse charge transfer coefficients and i^0 is the exchange current density of the cell which will have at T and reactant and product p_k dependencies as suggested in other references [53] and shown here:

$$i^0 = i_\infty^0 \exp\left(-\frac{E_{act}^0}{\overline{R}T}\right)\prod_k\left(\frac{p_k}{\overline{R}T}\right)^{n_k} \quad \text{(Eq. 2.7)}$$

where n_k are empirically derived power dependencies which are ignored if there is not significant p_k variation of the important reactants and products in the measurements performed. Equations 2.6 and 2.7 are used to fit the patterned anode η_{act} measured in this thesis as well as to evaluate the η_{act} of the cathode which is subtracted from the total cell overpotential measurements in order to isolate the anode $\eta_{act.}$

Ohmic polarization occurs because of resistance to the flow of ions in the electrolyte and resistance to flow of electrons through the electrode materials. The dominant ohmic losses, through the electrolyte, are reduced by decreasing the electrode separation and enhancing the ionic conductivity of the electrolyte. Both the electrolyte and fuel cell electrodes obey Ohm's law and the ohmic overpotential can be written in the form of the equation 2.8.

$$\eta_{ohmic} = iR_{el} \quad \text{(Eq. 2.8)}$$

in which the R_{el} is the electrolyte resistance.

Concentration polarization is caused by drops in reactant concentrations and increases in product concentrations due to mass transport limitations to and from the electrochemically active regions of the electrodes. Processes that contribute to these concentration-driven polarizations include gas diffusion in the electrode pores, solution/dissolution of reactants/products into/out of the electrolyte, or diffusion of reactants/products through the electrolyte to/from the electrochemical reaction site. At practical current densities, slow transport of reactants/products to/from the

electrochemical reaction site is a major contributor to concentration polarization. The concentration overpotential can be written in the form of equation 2.9 [99].

$$\eta_{conc} = \frac{\overline{R}T}{nF}\ln\left(1 - \frac{i}{i_L}\right) \qquad \text{(Eq. 2.9)}$$

where $i_L = \frac{nFD}{\delta}\left(\frac{PX_{ch}}{\overline{R}T}\right)$; and D is the diffusion coefficient of the reacting species, X_{ch} is the feed mole fraction of the principal reactant, and δ is the thickness of the diffusion layer. Since this research is using patterned anode electrode and highly porous cathode also in both anode and cathode excessive amount of fuel and oxidant is being fed, the effect of the concentration overpotential does not appear to be significant in these results.

For voltammetry and impedance measurements, two different wiring configurations can be used to record electrochemical data: a 3-probe configuration with a reference electrode and the 2-probe configuration with just a working and a counter electrode. In SOFC experiments, it is difficult to place a reference electrode on the electrolyte surface that does not have a variation in voltage as current density changes through the electrolyte. Thus, while a 3-probe provides the potential of isolating anode overpotentials, the variation in the reference electrode voltage with current density was found to cloud the measurements. Thus, two probe measurements were made exclusively and the cathode and electrolyte contributions to measured overpotentials across the whole cell were subtracted as described in Chapter 3.

Under equilibrium conditions, the working and the reference electrode are at the same potential, i.e. η_{anode} = 0 mV. In order to study the polarization characteristic of

the working electrode, a certain potential, the so-called overpotential, is applied between the working and the reference electrode. A positive potential signifies an anodic overpotential, whereas a negative potential signifies a cathodic overpotential. The working electrode is polarized with respect to the reference electrode and due to the electrical driving force, oxygen ions are forced through the electrolyte so does the electricity. The structure of the two probe measurement is the same as three probe measurement without the reference electrode. In EIS measurements, the excitation voltage is applied at two ends of the electrodes and the current is measured at the same two ends. If desired, an overpotential voltage can be applied across the cell.

In the *V-i* sweeps, the user specifies beginning and ending voltages between the working and reference probes. The potentiostat steps through this voltage range recording the current flowing from working the counter probe at each voltage.

Since two-probe measurements were performed, it was important to subtract the Ohmic losses associated with the resistance of the electrolyte phase and also the cathode losses which were measured as discussed below. The contribution of the electrode could easily be reduced by knowing the bulk resistance out of the impedance curves. The overpotential contribution from the LSM/YSZ cathodes on the other hand required additional experiments using a symmetric cathode cell to experiments were design to evaluate that. To this end, a single crystal disk was coated with LSM/YSZ cathodes in a symmetric cell configuration. The symmetric cell experiments with air and cathodes on both sides provided a basis for measuring the cathode overpotentials η_{cath} as a function of i. Also EIS measurements of the symmetric cathodes were performed in order to remove cathode impedances from the

full cells measurements with the patterned Ni anodes. Results from the symmetric cell studies were used to remove the cathode contributions to overpotentials and impedance spectra as presented in subsequent chapters.

2.4. Experimental Conditions

The experiments are designed to reveal the electrochemical reaction steps at the surface of the patterned nickel anode as well as their dependency to geometry and working conditions. Table 2.5 shows a range of conditions designed to address the electrochemical dependency of each parameter. Detailed matrix of the experiments is shown in chapter 5.

Table 2.5 – Range of parameters in experimental condition

Parameter	Unit	Minimum	Maximum
Fuel partial pressure*	kPa	8.44	33.77
Humidity in fuel	%	Dry (0%)	Wet (4%)
Cell temperature	°C	700	775
Pattern width	μm	10	100
Overpotential	mV	0	300

* Fuel diluted by Ar or reaction products

The Ni patterned anode was first introduced by Mizusaki et al. [4] to isolate the location where electrochemistry happens. They suggested reaction steps for electrochemical oxidation of hydrogen and proportionality between the length of three phase boundary and rate of reactions. Other researchers [5, 52, 66] have also implemented patterned Ni anodes, and re-examined Mizusaki suggestions. In all these studies data based on length of three phase boundary per unit area of electrolyte. Different experiments were conducted to assess the effect of the electrode width, l_{TPB}, and a_{cat}. As listed in Table 2.2, groups of patterns each containing 4 different patterns

were used to explore variations in these parameters and their impact on overall charge transfer reaction rates vs. overpotentials.

Although the increasing the temperature helps to lower the electrolyte resistance and at the same time facilitate the consumption of hydrocarbons as fuels, there is some disadvantages as well, like non matching coefficient of thermal expansion (CTE) and in case of deposited nickel structure, degradation and agglomeration of the nickel electrode. Due to the degradation of the Ni patterned anode in high temperature [38, 77] the working temperature was kept below 800 °C in most of the experiments. It is well understood that the electrolyte (bulk) resistance decreases almost linearly with increase of temperature [2]. The effect of temperature on charge transfer, adsorption/desorption and surface diffusion needs to be investigated.

3. Experimental Challenges of Patterned Anodes

In this chapter, the experimental methods are discussed along with the challenges and modifications implemented such that the patterned anodes provided the desired fundamental data. The Ni patterned anode experiments with CO as the primary fuel presented significant challenges both in conducting the experiments and analyzing experimental results. To address each of these obstacle series of experiments were considered. By means of each set of experiments an experimental base was built to conduct the basic experiments as was determined in the objective of the thesis. The target was to either overcome the difficulties or compensate for the shortcomings such that the result does not disturb.

3.1. Patterned Anode Stability

A significant effort was undertaken to determine patterned-anode fabrication techniques and architectures which provided microstructural stability for testing. Figure 3.1 shows an SEM image of a particular region of one pattern before electrochemical testing along with the schematic drawing of the microfabricated pattern showing which part is shown by SEM. Figure 3.1 shows the Ni microfabricated anodes before electrochemical testing with a pin-hole free structure on the surface of the single crystal YSZ electrolyte.

Careful optical inspection of the entire area of the patterns indicated almost no holes or cracks within the patterns at room temperature and extremely sharp anode-electrolyte interfaces with the photolithographic etching suggested that pre-test l_{TPB} may be approximated by the geometric value assuming a sharp transition between the

patterned anodes and the electrolyte. Figure 3.2 shows a magnification of 13500X by SEM of the edge of Ni pattern on YSZ surface.

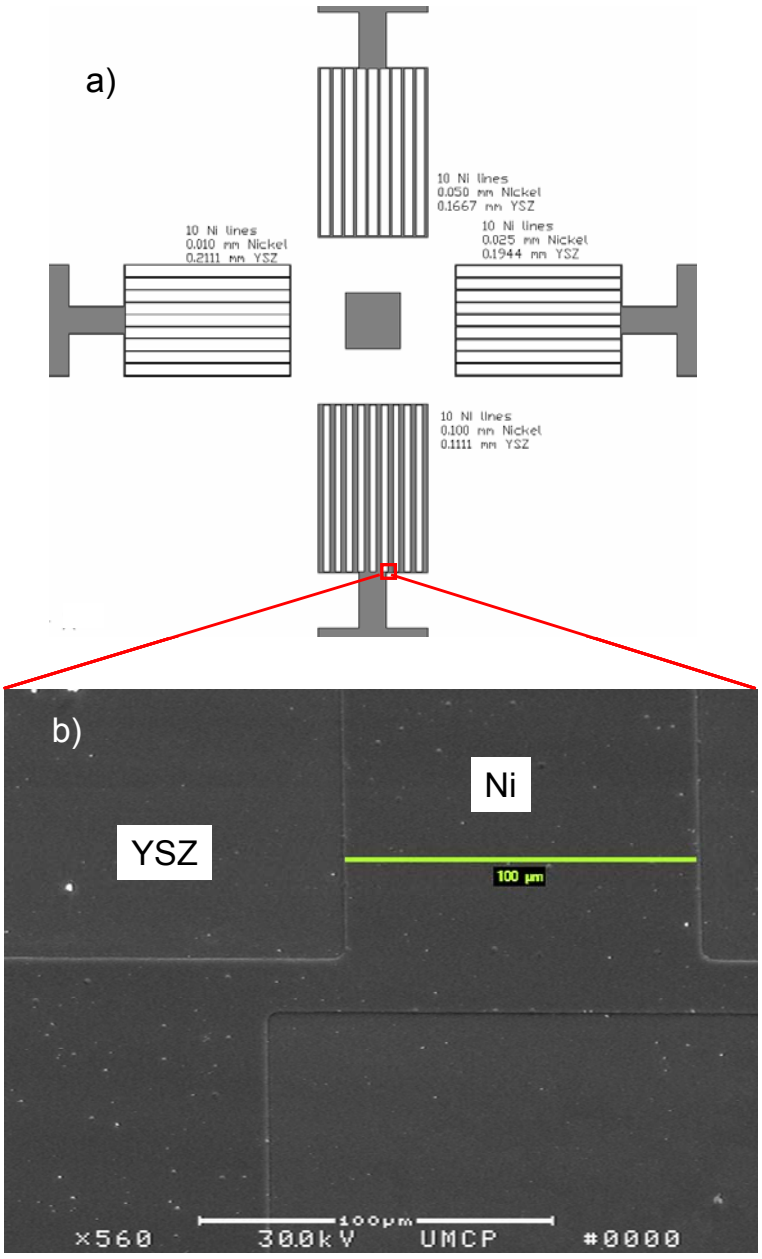

Figure 3.1 – A Ni pattern anode before undergoing electrochemistry: a) Schematic of a 4 pattern layout on MEA; b) 560X magnified SEM image of a pattern feature.

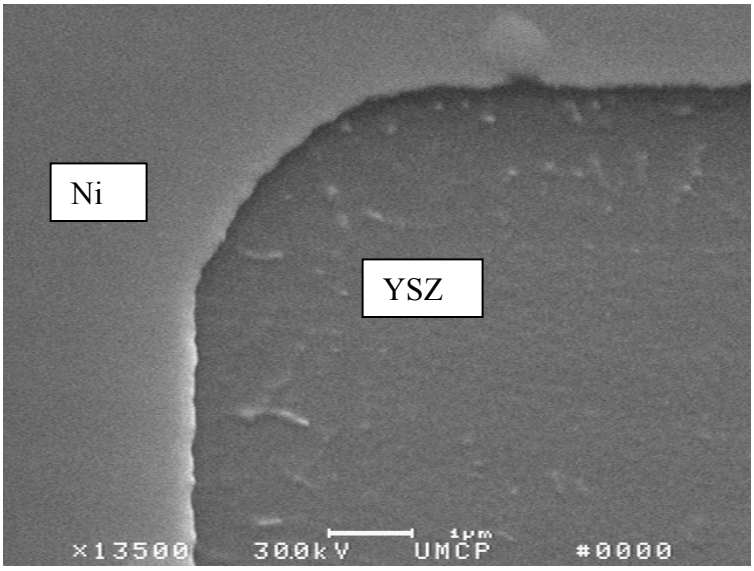

Figure 3.2 – The TPB of a Ni pattern before undergoing electrochemistry shows straight line TPB with 13500X magnified SEM image

During testing, an MEA undergoes cyclic oxidation and reduction due to electrochemical processes under different gaseous flow and applied current and voltages, as well as varying physical phenomena like temperature and CTE variation. The imposed environments to the Ni patterns make them physically and chemically affected which may sometimes lead to losing the patterns and whole cell. In this section some of these effects and the challenges to overcome or address each of those are described. Initial experiments were started by depositing a very thin layer of Ni on single crystal YSZ disc of 100 – 150 nm. Although this pattern thickness adhered well to the YSZ surface as indicated in Figure 3.3 (a-b), electrochemical testing at high T caused the thin films to break up into Ni agglomerates such that l_{TPB} could no longer be easily defined as indicated in Figure 3.3 (c).

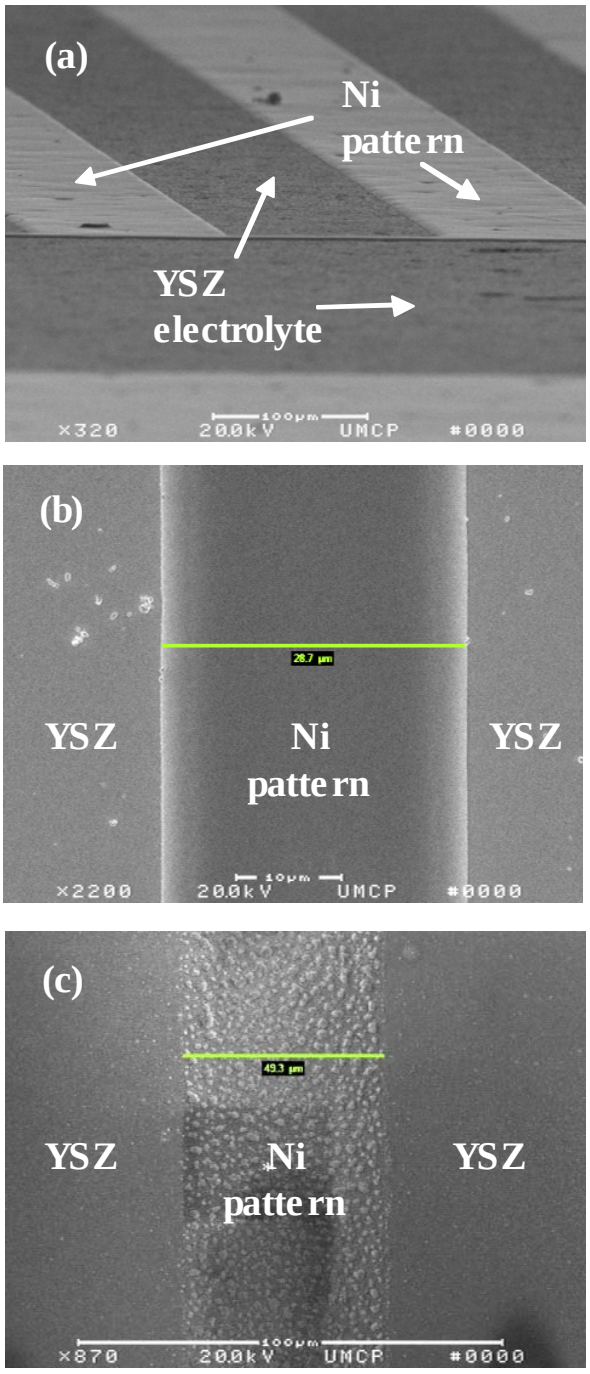

Figure 3.3 – SEM images of patterned anodes before and after testing: (a) angled image of 100 µm lines showing dense films before testing, (b) top-down image of 25 µm line before testing with dense Ni pattern with sharp Ni/YSZ interface, (c) top down image of 50 µm pattern after testing with agglomeration of Ni.

These agglomerated patterns arising from the 100 – 150 nm thick films still provided electronic conductivity and produced qualitative data without the obscuring

of mass transport effects as in porous anodes. However, since the l_{TPB} was not predictable under such condition, quantifying the result in terms of a per l_{TPB} basis was not possible. These results are published [86] and discussed briefly in chapter 4.

It was found that the thicker patterns maintained their architecture but just showed grain boundary growth as it is presented in the Figure 3.4. Detail on pattern stability criteria is presented as a master's thesis [77]. Thicker patterns eliminated the pattern disintegration and allowed for more stable l_{TPB} and allowed for some comparison of geometry dependent electrochemical characterization of the anodes.

However, evaluations of the patterns post electrochemical characterization revealed that the sharp lines of TPB in the pre-test patterned anodes were not maintained after exposure to reducing environments at the test temperatures (T = 750-850 ºC). Under these conditions, the Ni surface forms roughened surfaces which corrugates the Ni pattern edge and increases the original l_{TPB}. The maximum loss of Ni area for a pattern was estimated [77] to be 0.0110 mm^2 ± 0.0002 mm^2 or 2.5 % ± 0.04 % of the expected Ni area. The maximum loss of geometric l_{TPB} was estimated to be 960 μm ± 40 μm or 1.36 % ± 0.06 % of the expected TPB. The losses were assumed to have minimal impact on anode performance and were therefore neglected when normalizing electrochemical measurements with respect to Ni area or geometric TPB length. This effect is illustrated in a post-test SEM image in Figure 3.4.

The roughened surface of the pattern was observed repeatedly and explains a steady drop in $R_{pol,a}$ to a near steady value with the initial exposure of the thin patterns to the high temperature reducing environment at open circuit conditions. As explained in the results and discussion, the resulting increase in l_{TPB} due to this break-

up of the dense films resulted in a correlation between initial pattern area a_{cat} and l_{TPB} such that all of the patterns gave similar l_{TPB}/a_{cat}.

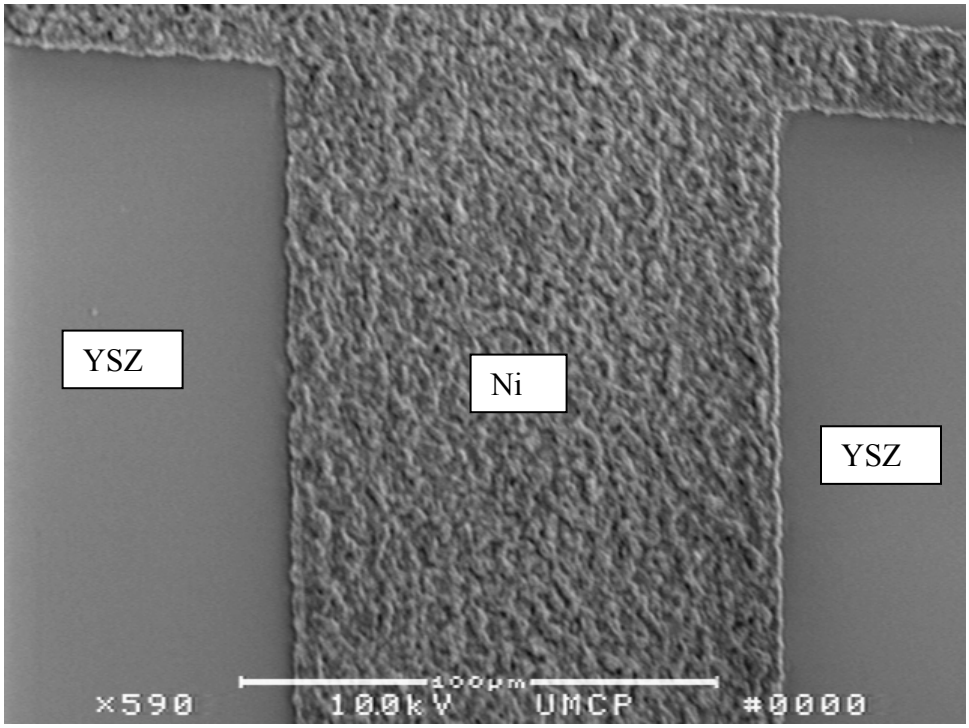

Figure 3.4 – SEM picture shows the rough surface of a 100 µm pattern strip being exposed to CO/Ar stream (P_{CO} = 0.33 bar) carrying 1.6% humidity with 200 mV applied overpotential

In general, type of the material and their physical properties, cell operating conditions such as T, $p_{H2O,anode}$, and η_{anode} as well as duration of operation impact the stability / integrity of the Ni anode patterns. It was explained in chapter 2 that for collecting current from the patterns they were connected to a collector bar and guided to the outer boundaries of the cell. Au wires were attached to the Ni collector bar, as in Figure 2.6, and these collectors were covered by gold paste to minimize their contribution to electrochemical reactions. The Au/Ni interface caused some failures of the patterns as shown in Figure 3.5, where the connection between gold paste and

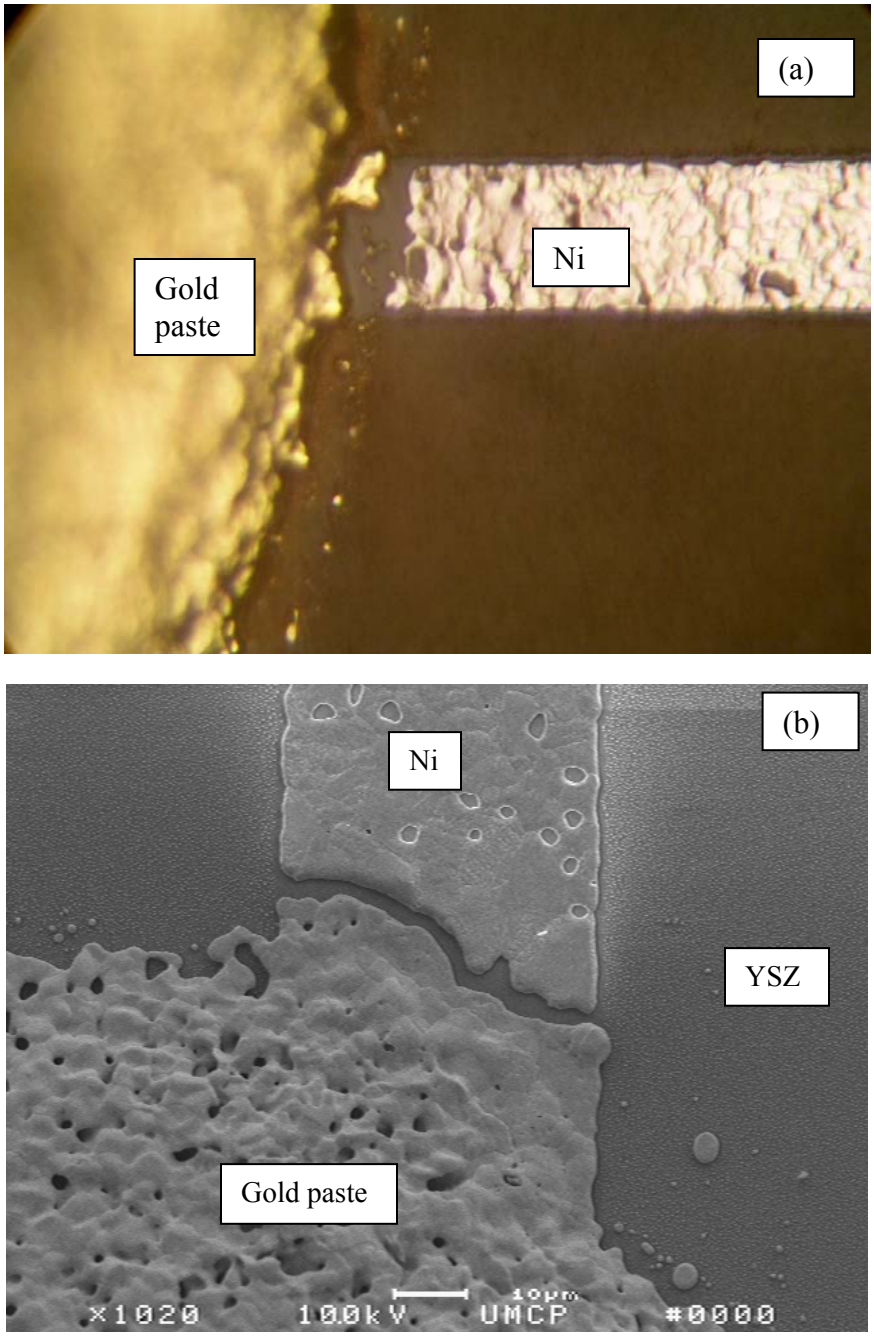

Figure 3.5 – Pattern failures near the Au paste, patterns were exposed to diluted CO/CO_2 in Ar (1:2) at the range of T ~750 °C. a) Optical picture b) SEM picture

sputtered nickel clearly caused a separation between the collector an which in such cases no more data could be collected. To eliminate the pattern failures caused by the

gold paste, a flattened gold wire was tacked to the YSZ surface by ceramic paste, as illustrated in Figure 2.8, and gold paste was used to attach gold wire to the wide part of the Ni collector bar.

The residual stresses in the Ni pattern during the sputtering process sometimes will lead to peeling off the Ni stripes from the polished surface of the YSZ disc under the high working temperatures. Although this was not a general case in the series of experiment was conducted in this research, it has been observed once. Figure 3.6 shows a picture of this effect. To avoid any further problem with the residual stresses the heating rate of the furnace was decreased to 1 °C/min.

Under the working temperature of the SOFC, Ni metal is very susceptive to react with oxygen to turn into NiO. Turning Ni into NiO will stop the cell from working as an electrochemical converter. Sometimes this could happen by leaking oxygen through the cell sealant at the anode side. It can be seen from Figure 3.7 that in parts

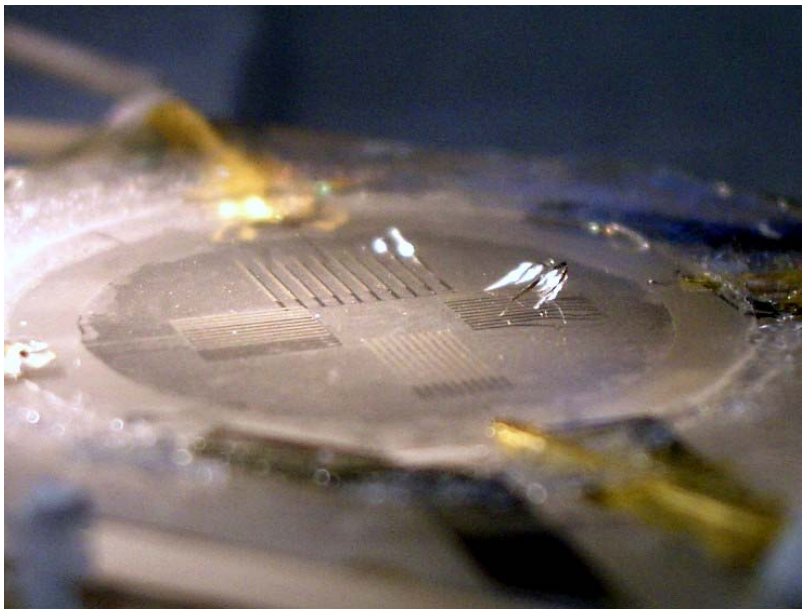

Figure 3.6 – Residual stress in Ni stripes causes pealing off from the surface while heating up the MEA.

of the cell close to an opening to the atmosphere shiny surface of the metallic Ni has turned into green color NiO. Also there has been some observation [100] that Ni anode could be used as a secondary fuel in case of shortage of the main stream fuel. Since in our designed experiences efficiency is not being studied fuel is fed excessively to avoid such phenomena.

To overcome leakage of the air into the anode chamber a couple of actions were taken. The first action was to use flattened gold lead and set of glass and mica which were explained in detail in chapter 2. The next action was increasing the relative pressure in the anode chamber by flowing more gas. Also in the compression rig, as long as the MEA could tolerate the extra pressure, increasing the pressure of the spring by few percent could help avoiding leakages into the cell.

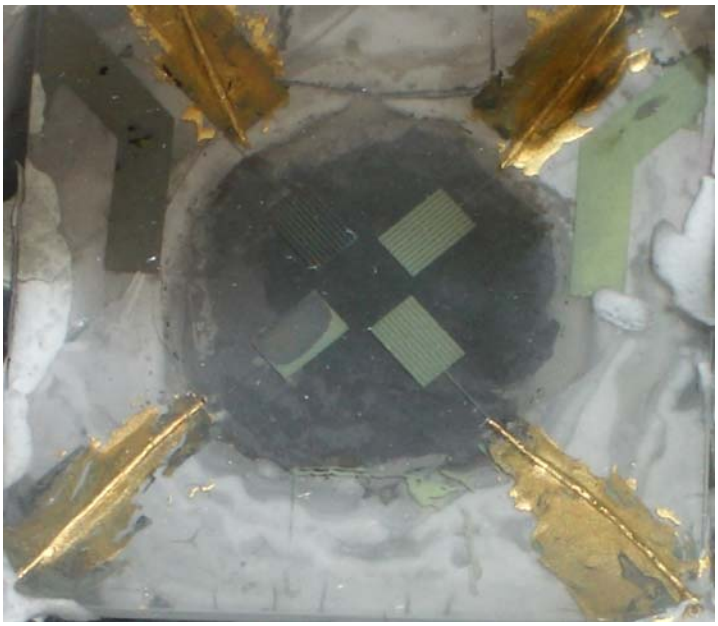

Figure 3.7 – Effect of the exposure of Ni to atmosphere/oxygen turning it into NiO due to leakage in the cell

While direct exposure of O_2 to the Ni anodes will cause structural damage due to rapid NiO production, applying significant anode overpotentials (> 0.5 V) for excessive periods of time can have a similar effect. Figure 3.8 shows Raman spectra from two Ni anodes which were cooled under different environments. The first spectra was obtained for a Ni patterned anode which was cooled down with the Ni anode at OCV conditions while exposed to a reducing environment with $p_{H2} \sim 5$ kPa. The second spectra was taken for a Ni-patterned anode that was cooled in a neutral gas stream (Ar) with a significant overpotential of 400 mV. The Raman spectra of the second case (case b) show few clear peaks which after matching those with the result reported by Pomfret et al. [101] these peaks are NiO peaks. Since Ni was only exposed to Ar gas, there has been no oxidant available to turn the Ni into NiO. The

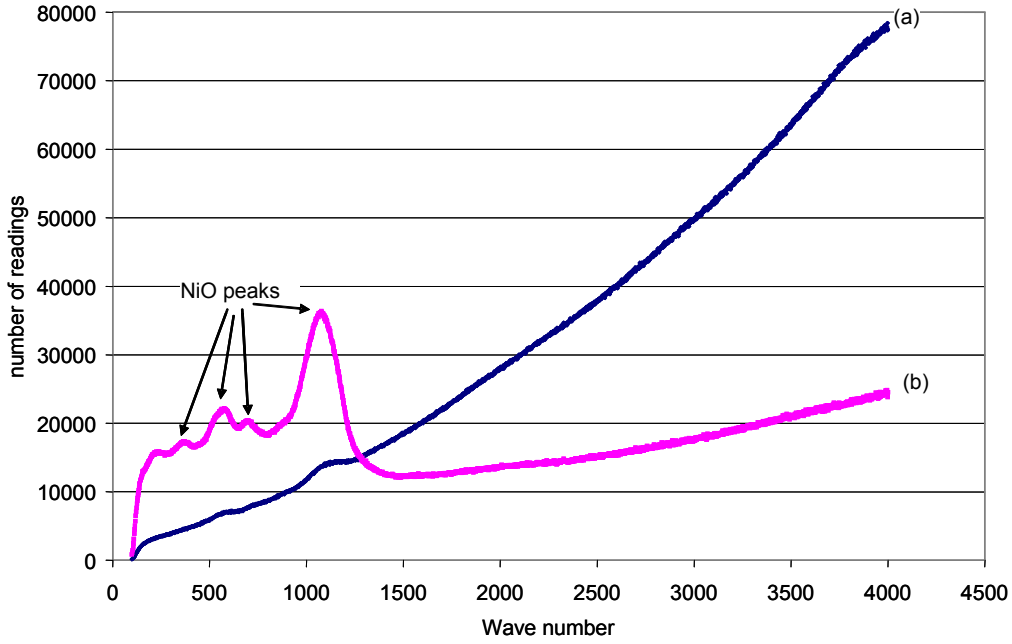

Figure 3.8 – Raman spectra of the Ni anode surface after being cooled down a) Under reducing environment of diluted H_2 and OCV; b) under inert environment of Ar and overpotential of 400 mV.

applied overpotential of 400 mV has forced the bulk oxygen inside the YSZ move toward the anode; hence react with the Ni at the surface to form NiO. However, Raman spectra of Ni surface when MEA was cooled down under OCV condition does not show any NiO peaks on it.

At low oxidation potentials, pure CO can react with Ni metal and form volatile Ni carbonyls as discussed in earlier references [102, 103]. This can result in removal of Ni material under high partial pressures of CO, $p_{CO,}$. Under high $p_{CO,}$ approaching 1.0 bar, the Ni surface is etched by CO resulting in holes or pocks in the Ni patterned anodes as shown in Figure 3.8. To overcome this effect diluted the CO with Ar and CO_2 was utilized. A CO/CO_2 mixture as fuel stream mixed with twice as Ar generating $p_{CO} < 0.3$ bar showed that Ni metal can be stable with no hole on the surface even after two days of continues experiment.

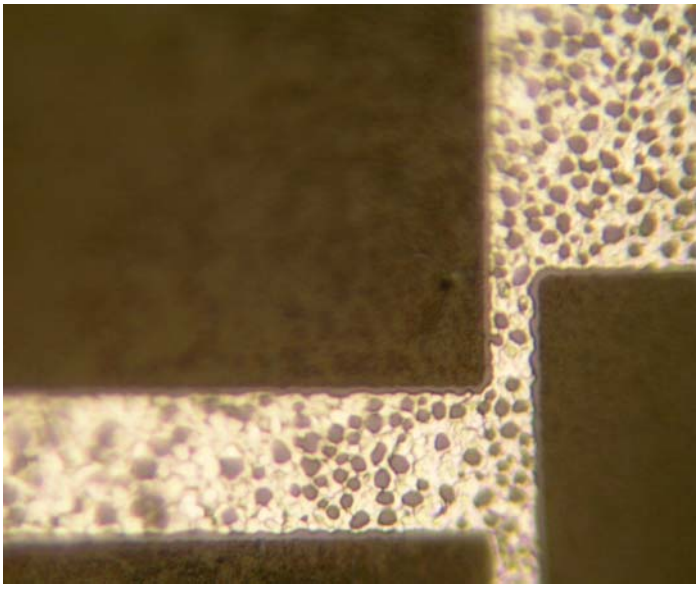

Figure 3.9 – Corrosive effect of pure CO on Ni patterns which is the effect of Ni carbonyl production

3.2. Isolating Anode Contributions

Because the research objectives were focused on anode electrochemistry, there was a need to isolated anode overpotentials and impedances from the contributions of both the cathode and the electrolyte. For this purpose normally the method of three probes is being used, while in the conducted experiments in this research due to the some technical problem that was not possible. The problem is that the reference voltage depends on the current density through the electrolyte and the voltage at the reference electrode may change for different anodes operating at the same overpotentials. Thus, the difference between the anode and reference voltage are not consistent between the different anodes. Also for a given anode, as the overpotential increases, the reference voltage changes because of the voltage distribution in the electrolyte and as such the voltage does not serve as a real reference.

Adler [104] has also stated the problem as the complex potential distribution in a thin electrolyte. In such cases even small errors in alignment of anode and cathode will generate significant errors in measured overpotential which are normally involve quantitative scaling factors and cross contamination of measured frequency response of anode and cathode. By using finite-element calculations of the real and imaginary potential distributions in the electrolyte he showed that even if the electrodes are perfectly aligned, different kinetics in anode and cathode will provide different frequency responses that cause distortion of the impedance including frequency dispersion and inductive artifacts. He concluded that in thin 2D geometry these types of distortions are inevitable.

To overcome this shortcoming, an experimental method was designed and conducted such that the contribution of the cathode can be measured individually and to be altered for the overall cell's data. A single crystal disc was picked and was painted at both sides with the cathode material, LSM/YSZ. Then it was sintered and a set of electrochemical experiments was done on this uniform symmetrical cell under different temperature to characterize the nature of the LSM/YSZ electrochemistry and its contribution into the overall impedance spectra and overpotential. Figure 3.10 shows the result of the impedance spectra of this cell under a wide range of temperature. It is clear from these data that the electrolyte contribution varies as the temperature changes. To see the clear effect of cathodic resistance first the electrolyte resistance can be reduced from the data. Needless to say that this result is representing both side of the cell so the proper one sided cathodic contribution can be achieved by splitting the impedances into two equal parts since there is a symmetry in the cell. Figure 3.11, shows the final version of the impedance spectra which is the pure cathodic contribution. The results of the impedance showed that there is an inductive effect in addition to the capacitive and resistive effects. Also as the temperature increases the cathodic resistance decreases.

The well-behaved impedance spectra for the cathodes were used to derive area specific impedances Z_c for cathode polarization which are plotted in a Nyquist plot in Figure 3.11. The relaxation frequencies for the cathodic processes are as such indicated that the porous cathode processes with its higher surface area were faster than the lower-surface area patterned anodes. Thus, it was deemed feasible to subtract out the cathode impedances as a function of frequency from the overall cell

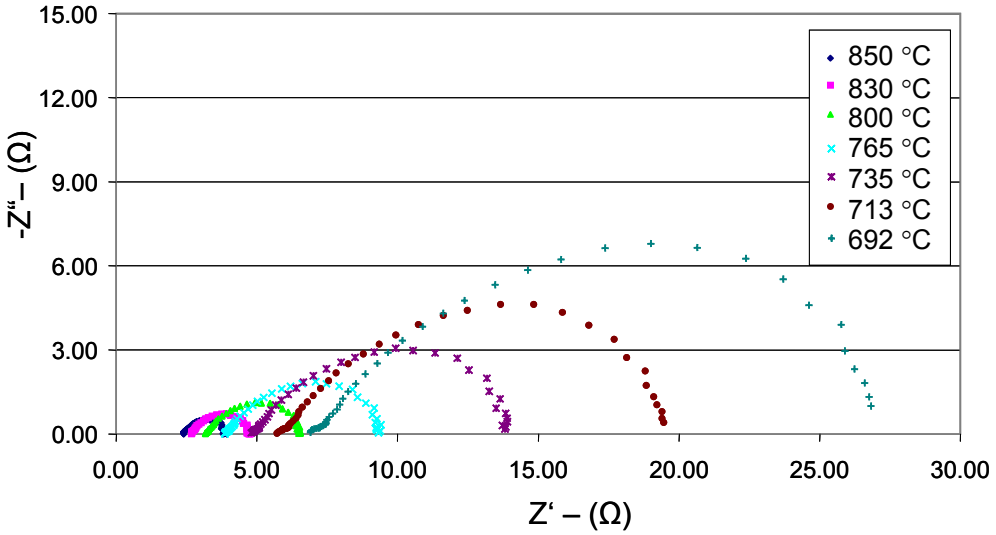

Figure 3.10 – Uncorrected impedance spectra of symmetrical cell of LSM/YSZ/LSM exposed to air at both end in different working temperatures

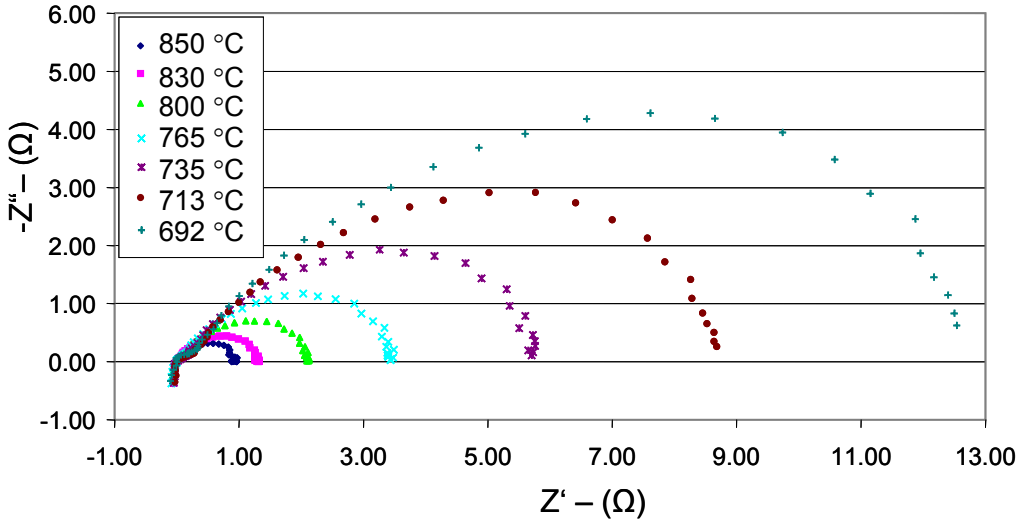

Figure 3.11 – One sided cathodic impedance spectra of a symmetrical LSM/YSZ/LSM cell exposed to air in different *T* without electrolyte contribution

impedance in order to isolate impedances associated with the non-porous anode. To this end, the area specific cathode impedance spectra were fit (using a non-linear least squares approach) to an equivalent circuit consisting of circuit elements arranged as follows [LR_1 [(C [R_2 (R_3Q)])] as in the Figure 3.12. In this fit, L is associated with

lead inductances, C is the double layer capacitance, R_1 is the electrolyte resistance, and R_2 and R_3 are resistances associated with polarization of each of the cathode, and Q a constant phase element. Table 3.1 shows the equivalent circuit fit to the measured cathode impedances. The fitted impedance circuits were used to calculate area specific impedance for a given test condition and then multiplied by electrolyte area, a_{elec} for each pattern and then subtracted from the measured impedance to derive the $R_{pol,a}$.

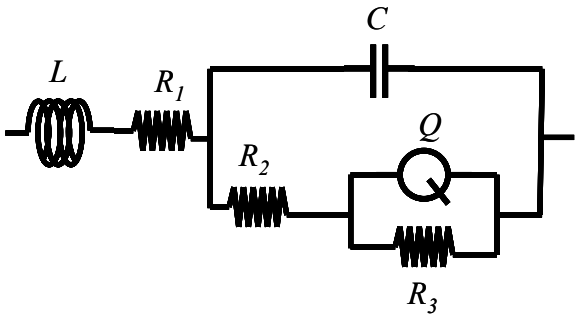

Figure 3.12 – The equivalent circuit of the cathodic impedance which includes the inductance associated to the leads, L, and electrolyte bulk resistance, R_1. The rest of the impedance is associated to cathodic resistance.

Table 3.1 – Fitting parameters for impedance data at different temperatures at p_{O2} = 0.21 atm and a_{cell} = 1.26 cm^2.

T (°C)	L (μH)	R_0 (Ω)	C (μF)	R_1 (Ω)	R_2 (Ω)	Y_0 (S*s^n)	n
692	0.882	6.81	33.0	0.478	21.46	0.0116	0.68
713	0.929	5.63	34.1	0.404	14.39	0.0119	0.69
735	0.951	4.68	40.8	0.308	9.41	0.0119	0.70
765	0.999	3.74	39.6	0.237	5.60	0.0117	0.71
800	0.909	3.08	58.7	0.164	3.39	0.0115	0.72
830	0.934	2.58	91.0	0.123	2.07	0.0108	0.74
850	1.020	2.29	30.9	0.112	1.52	0.0111	0.73

The electrolyte area which determines the area of cathode and electrolyte contributing to the electrochemical processes is defined as the area underneath each pattern including the spacings of exposed YSZ between strips and a boundary around the outside of the pattern as wide as the electrolyte thickness.

The cathodic polarization based on a_{elec} was small relative to anode contributions. It can be seen from the chapters 3 and 4 that subtraction of the cathodic impedance is not significant and the major R_{pol} is due to anode contribution. The cathodic contribution in *V-i* measurements was subtracted out by using a Tafel fit to the symmetrical LSM/YSZ/LSM *V-i* data. For this purpose Tafel plots, shown in Figure 3.13, for the LSM/YSZ porous cathodes were used to derive Butler-Vollmer fits for the measured range of *T*. These fits fell very nicely on top of the data and were used to subtract out η_{cath} from the *V-i* measurements as a function of *i* based on a_{elec}.

Fitting the cathode Tafel plots to a simplified Butler-Vollmer equation (equation 3.1 shown here) can be employed to derive effective exchange current densities i^0 and anode exchange coefficients β_f for the electrochemical oxidation processes.

$$i_{A,fit} = i_{\infty}^{0} \exp\left(-\frac{E_{act}^{0}}{\overline{R}T}\right)\left[\exp\left(\frac{\beta_f \eta_{cath} F}{\overline{R}T}\right) - \exp\left(-\frac{\beta_r \eta_{cath} F}{\overline{R}T}\right)\right] \qquad \text{(Eq 3.1)}$$

In equation 3.1, the exchange current density $i^0 = i_{\infty}^{0} \exp\left(-\frac{E_{act}^{0}}{\overline{R}T}\right)$ and at high η when the second term in the brackets is quite small, Eq 3.1 can be approximated by this equation can be rewritten in form of:

$$i_{A,fit} = i^0 \exp\left(\frac{\beta_f \eta_{cath} F}{\overline{R}T}\right) \qquad \text{(Eq. 3.2)}$$

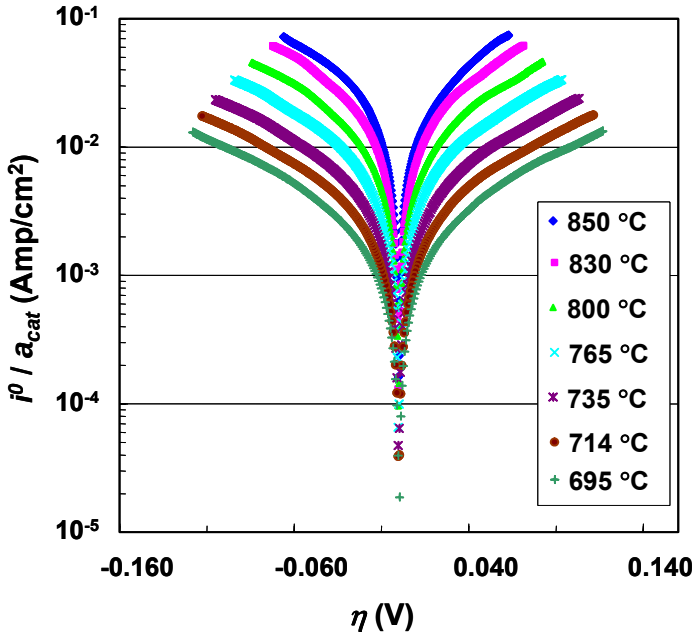

Figure 3.13 – Plot of cathode current densities i^0 as a function of η as measured from symmetric cathode experiments.

3.3. Accounting for Three Phase Boundary and Ni Area Effects

To address the contribution of the l_{TPB} and a_{cat} in the measurements multiple patterned anodes were deposited on thick YSZ electrolyte supports and opposite a high porosity LSM/YSZ cathode. Electrochemical measurements (voltammetry and impedance spectroscopy) were utilized to explore the differences in performance of the co-deposited patterns in order to assess how geometrical factors such as a_{cat} and l_{TPB} impacted impedances and overpotentials. Due to the challenges, with the pattern stabilities and the gold/Ni interfaces at the interconnect junctions, experimental conditions were limited and as discussed earlier in reference to Table. 2.2, various groups of patterns were designed to study different geometry aspects. As in previous patterned anode SOFC studies [65, 84] the rate of the reaction is expected to be a

function of the l_{TPB} for each anode yet it is not clear how the a_{cat} and the perimeter plays a role in the rate of the reaction.

The experiments in this study were set up to reveal some unanswered questions regarding the geometrical effect of the patterns. Mizusaki [4] and Bieberle [84] have presented their result as a function of l_{TPB}/a_{elec}. According to the investigated result of the projected area discussed in previous section, in current study this ratio is kept constant for all patterns and the only varying parameter is contact area of the nickel. The comparison of the a_{cat} discussed here considers all patterns with equal l_{TPB}.

There is a question of the effect of the perimeter of the pattern or the projected area of the outer boundary of the pattern on the electrochemistry of the cell. To answer to this question a specific Ni patterned anode according to the group D of the patterns geometry (detailed in Table 2.2) was selected. As it can be seen from Figure 3.14, two sets of patterns with equal l_{TPB}, and equal a_{cat} are on this cell. The only difference is that the Ni stripes are lay down with double the spacing in one of these patterns. In other word the a_{elec} of one pattern is twice as the other patterns. In this experiment it was expected to get the same impedance spectra in both patterns as the l_{TPB}'s are the same. In fact if this is the limiting process then both electrodes should give the same overall anode overpotential and impedances. If not then some other processes that are geometry dependent may be involved.

The result showed that the R_{pol} are the same the only difference is in the R_{bulk}. The impedance spectra for two patterns using wet H_2 as fuel can be seen in Figure 3.15. It clearly shows that the overall R_{pol} are the same, while the R_{bulk} for pattern with the narrower distances between stripes of nickel is bigger than pattern with wider spacing

between stripes. In other word the bigger the a_{elec} the smaller the R_{bulk} will be. This change in R_{bulk} almost scales with the a_{elec} as in this experiment the pattern with twice as the a_{elec} has the half the R_{bulk}.

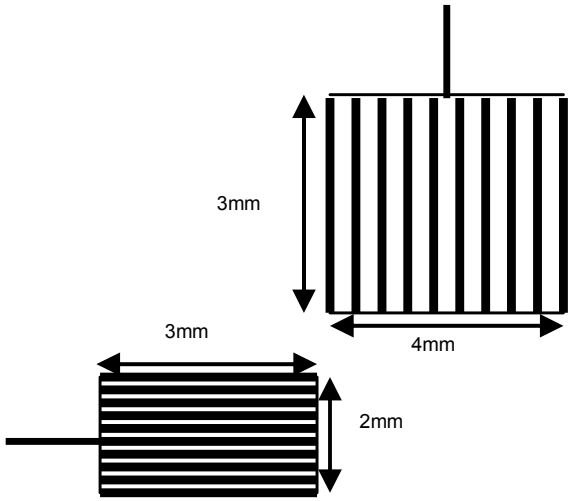

Figure 3.14 – Schematic of the pattern group D to investigate the dependency of the R_{bulk} to the a_{elec}.

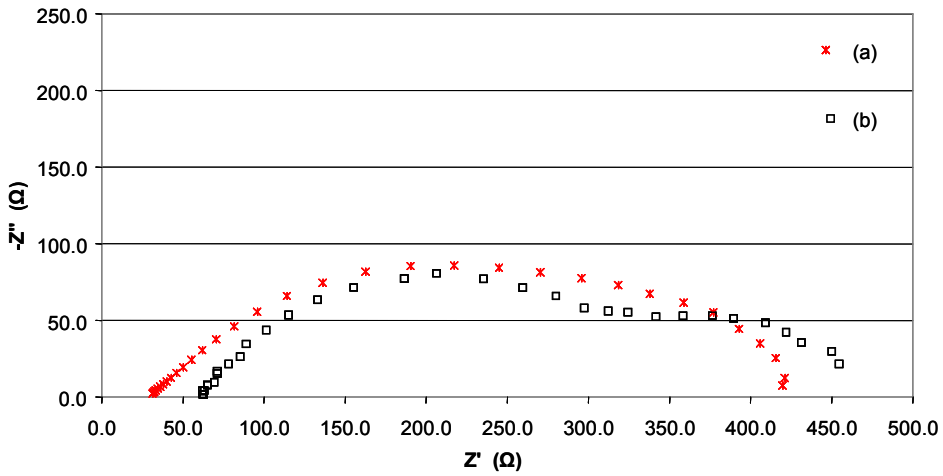

Figure 3.15 – Impedance plots for wet H_2 fuel at OCV, T = 750 °C for two cases, (a) YSZ width = 0.111 mm and (b) YSZ width = 0.333 mm at group D pattern show R_{bulk} scales with the a_{elec}

This experiment suggests that to compare two different patterns it is better to use equal projected area. Almost all the conducted experiments in the next chapters has been done with the pattern group B from the Table. 2.2.

Mizusaki [4] and Bieberle [84] had suggested that the charge transfer in nickel pattern anode is a function of the l_{TPB} while using H_2 as fuel. Although they did not investigate the effect of the a_{cat}, it would not show any effect while using H_2 as fuel. Normally the rate of the adsorption and desorption of the H_2 molecules is very fast that the surface diffusion will not play a role in rate determining step in the overall reaction. If the fuel is changed to CO instead of the H_2 this is not the case any more. It can be seen for CO that the dependency of the charge transfer is not only a function of the l_{TPB} but is a function of the a_{cat} at lower T.

3.4. Summary of Experimental Challenges

The challenges mentioned in this chapter were revealed during the experimental program. These challenges revealed limitations with the patterned anode experiments which were not heretofore expected. The lessons learnt listed discussed in the previous sections provided a basis for moving forward with reliable experiments using well-defined and stable microfabricated patterned anodes. In the next chapter, experimental results are presented for H_2 electrochemical oxidation on stable Ni patterned anodes (as discussed in this chapter) and these studies include H_2 with and without the presence of CO. In the subsequent chapter, patterned anode experiments are used to explore CO electrochemical oxidation which is a critical new contribution of this study to the SOFC literature.

4. H_2 Electrochemical Oxidation

Understanding CO oxidation in SOFC anodes, particularly under humidified conditions, must be linked to an understanding of H_2 electrochemical oxidation. Since the patterned anode experiments are designed to remove gas-phase and porous media transport influences on electrochemical oxidation rates, it is important to assess H_2 electrochemical oxidation processes on the patterned anodes to compare with both wet and dry CO electrochemical oxidation experiments.

H_2 also provides a well-studied fuel with some established quantitative models for electrochemical oxidation in the Ni/YSZ system [52, 67, 68, 105, 106]. Since many early SOFC studies focused on H_2 electrochemical oxidation in Ni/YSZ cermet anodes [4, 65, 66, 75, 84], experiments on H_2 electrochemical oxidation on the Ni patterned anodes will provide a basis for validating patterned anode modeling efforts and for comparing with past studies, including the earlier patterned Ni anode research of Bieberle [5, 52, 84]. This chapter presents a brief review of some of the previously conducted research on H_2 electrochemical oxidation in Ni/YSZ anodes and then presents the experimental results for this study in that context.

4.1. Review of Past Results

As discussed earlier in Section 1.3, electrochemical oxidation of H_2 on Ni/YSZ electrodes in SOFC's is a multi-step process involving adsorption, surface reactions, and charge transfer. Some [66, 107] have postulated a multi-step mechanism that was summarized here in the following steps:

- dissociative H_2 adsorption on the Ni surface,

- surface diffusion of H_{Ni} to the TPB,
- ionization of H_{Ni} to H^+ on the Ni electrode,
- two-step charge-transfer involving the $H^+ + O^{2-}$ and $H^+ + OH^-$ at the TPB,
- desorption of H_2O molecules from the YSZ surface.

In this multi-step process, the rate-determining steps that control the overpotentials (and impedances) have been debated in the literature, but recently Bessler et al. [51] and Primdahl et al. [107] give strong suggestions that the $H^+ + OH^-$ charge transfer reaction may be rate-controlling for $T < 800$ °C, although it is likely that the rate-controlling step(s) depend on conditions T, p_{H2O}, and η_{anode}.

Other mechanisms for H_2 electrochemical oxidation on Ni/YSZ have been proposed from patterned anode studies that involve charge-transfer reactions where O^{2-} passes to the Ni and reacts with H atoms to form OH and H_2O [4, 5, 65]. Bieberle et al. originally suggested [52, 68, 105] such a charge transfer reaction, but in later analysis proposed that charge transfer involving H^+ ions jumping to the YSZ to form OH^- ions which reacts with each other to form H_2O for desorption and a surface O^{2-} ion for further reaction with H^+ [53, 69, 105]. Goodwin has added to the understanding of this mechanism and proposed that the final rate-controlling oxidation step is H^+ reacting with OH^- at the TPB before forming H_2O for desorption. Less attention has been given to quantifying the surface chemistry on the electrolyte, which has been shown to be a good protonic conductor in the presence of H_2O [108] and to undergo reduction in the presence of H_2 [109].

While there has not been clear agreement on the mechanism or the rate-determining steps for H_2 electrochemical oxidation on Ni/YSZ anodes, a recent

detailed modeling [106] study comparing predictions of different H_2 oxidation mechanisms with measurements on Ni patterns has shed new light by comparing various proposed mechanisms. That study gives strong credence to the reaction Goodwin's mechanism by evaluating data from patterned anodes studies. The study also shows the importance of the underlying thermodynamics since many H_2 surface and oxidation reactions are assume to be reversible and equilibrate even at very short time scales. Further patterned anode studies may still help provide new data for quantifying some of the key reactions in H_2 electrochemical oxidation on Ni. Williford and Chick [110] hypothesized that spillover of O^{2-} ions onto the catalyst surface leads to a variable width of effective TPB for several tens of nm. While their proposed size of the TPB region seems to be consistent with others [69], spill over of O^{2-} onto Ni does not seem appear to be the rate-controlling process in H_2 oxidation and thus should not determining the width of the TPB.

4.2. Experimental Conditions

To compare with past patterned anode studies, an initial series of experiments with the patterned anode MEA's was undertaken to study H_2 electrochemical oxidation with thin (100 nm) Ni patterned anodes were applied. These very thin Ni patterns experienced disintegration into small interconnected agglomerates as discussed earlier in chapter 3 and illustrated in Figure 3.3. The disintegration did not disrupt the electronic conductivity of the pattern but is also did not allow for l_{TPB} be readily quantified, and thus the value of these measurements for understanding patterned geometry effects was limited. Nonetheless, the effect of the temperature and p_{H2O} on the Ni-patterned anode electrochemical performance was studied [86].

For these initial experiments, the patterned anode MEA's were operated with a flow of diluted fuel (H_2 and/or CO) in Ar on the anode and a flow of air on the cathode. After measurements on dry fuel mixtures were made, the Ar with or without the fuel was bubbled through a water bath at 25 ± 2 ºC ($p_{H2O,sat}$ = 0.31 ± 0.04 bar) before entering the anode side for measurements on wet fuel feeds. For all fuel compositions in this study, electrochemical measurements were made at T from 750 ± 10 ºC up to 850 ± 10 ºC. Multiple cells were tested for these experiments to test consistency of the results.

The original intent of this study was to observe how η_a vs. i and anode impedances for H_2 electrochemical oxidation correlated with l_{TPB} or l_{TPB}/a_{elec} of the patterned Ni anodes. Also, the experiments were then to investigate the effect of the presence of CO and humidity on the H_2 electrochemical oxidation processes. Previous patterned anode studies with thicker patterns attempted to correlate polarization resistances with l_{TPB}/a_{elec} [4] but significant scatter in the results raises questions as to the quantitative reliability of correlations from those studies. In these experiments group C patterns, according to Table 2.2, were used. A schematic of this group can be seen in Figure 4.1. The calculated value for the a_{elec} for this group (C) of patterns sputtered on a 0.5 mm thick YSZ single crystal disc for each set of the patterns are listed in Table 2.2.

In the current study, which began with thinner Ni films than earlier studies [4, 5, 66], breakup of the originally dense Ni films into interconnected regions with exposure of TPB internal to the original pattern area did not readily permit correlation of η_a and $R_{pol,a}$ with l_{TPB}/a_{elec} because the greatly enhanced l_{TPB} was not easily

characterized by SEM imaging. Correlation of results with original coverage area of the Ni patterns, a_{cat}, elucidates how H_2O content and T impact electrochemical processes that occur in Ni/YSZ anodes.

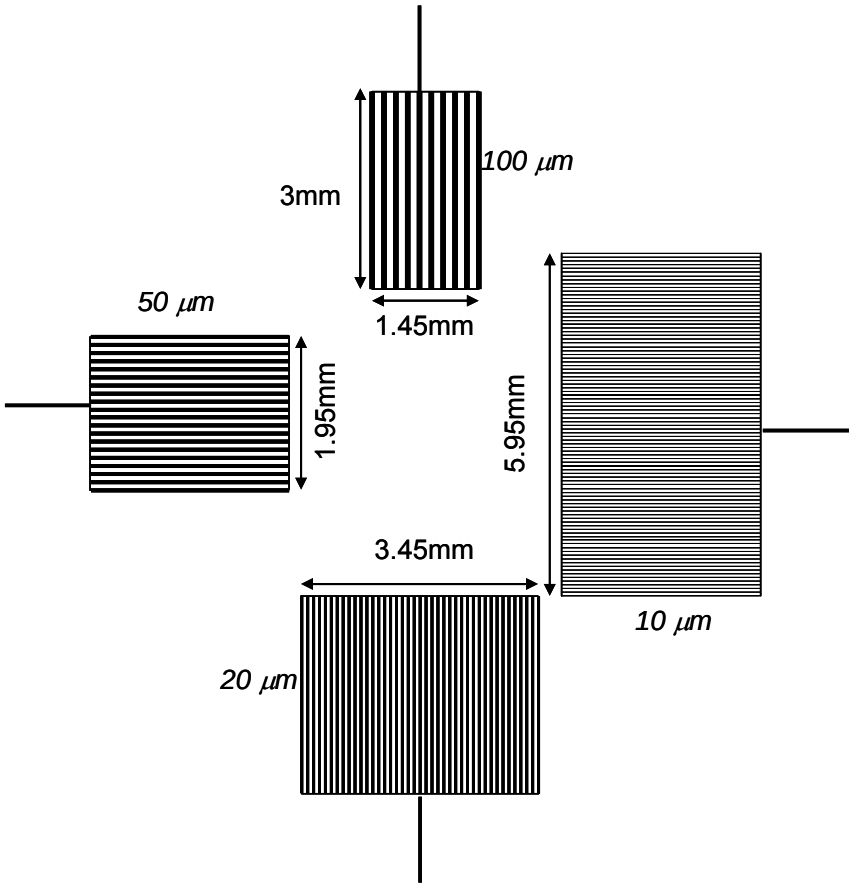

Figure 4.1 – A schematic view of the group C layout, with 4 patterns; 100 lines of 10 μm, 50 lines of 20 μm, 20 lines of 50 μm and 10 lines of 100 μm Ni patterns.

4.3. Voltammetry Studies

Figure 4.2a shows uncorrected V_{cell} and power densities ($\dot{w}$) vs. i (based on a_{cat}) for the four different anodes from group C for $p_{H2,a}$ = 0.33 bar (diluted in Ar) as fuel. The lower V_{cell} and $\dot{w}$ for the widest 100 μm pattern can in large part be attributed to the smaller a_{elec} and thus higher iR_{bulk} and η_{cath} losses for the 100 μm patterns. From

the pattern images in Figure 3.3, it is not expected that the current density scales with the original l_{TPB} rather scales with the a_{cat}.

To properly isolate the patterned anode overpotentials η_a, iR_{bulk} and cathode overpotentials η_c must be subtracted from the losses in the *V-i* curves. iR_{bulk} losses are removed by basing *i* on the expected electrolyte area (a_{elec} in Table 2.2 for Group C) contributing to a given patterned anode as discussed above. From the symmetric cell cathode experiment performed for the range of cathode current densities and *T* experienced in the H_2 and CO electrochemical oxidation tests in this study, η_c for the porous LSM/YSZ was obtained as it was discussed in section 3.2. The corrected *V-i* curves in Figure 4.2b (where i_a is based on the original Ni pattern area) are quite similar with all four patterns for H_2 electrochemical oxidation.

Tafel plots for H_2 electrochemical oxidation on a representative pattern (20 μm) are provided in Figure 4.3a. Both anodic ($\eta_a > 0$) and cathodic ($\eta_a < 0$) overpotentials for the anode are plotted for p_{H2} = 0.30-0.33 bar from 750 to 850 °C for both dry and wet (p_{H2O} = 0.03 bar) conditions. For the anodic overpotentials, the dry and wet conditions showed similar performance with respect to η_a, and as expected for the cathodic overpotentials, the addition of water greatly enhanced the reverse reaction rates (|*i*|) for water electrolysis. However, for the fuel cell relevant anodic overpotentials, the effect of adding the small amount of H_2O was not significant on *i* vs. η_a at 850 °C. At 750 °C, some enhancement did appear in *i* vs. η_a as reported in the literature [5], but such enhancement is offset by a drop in the V_{cell} due to thermodynamic reduction of the V_{OCV}.

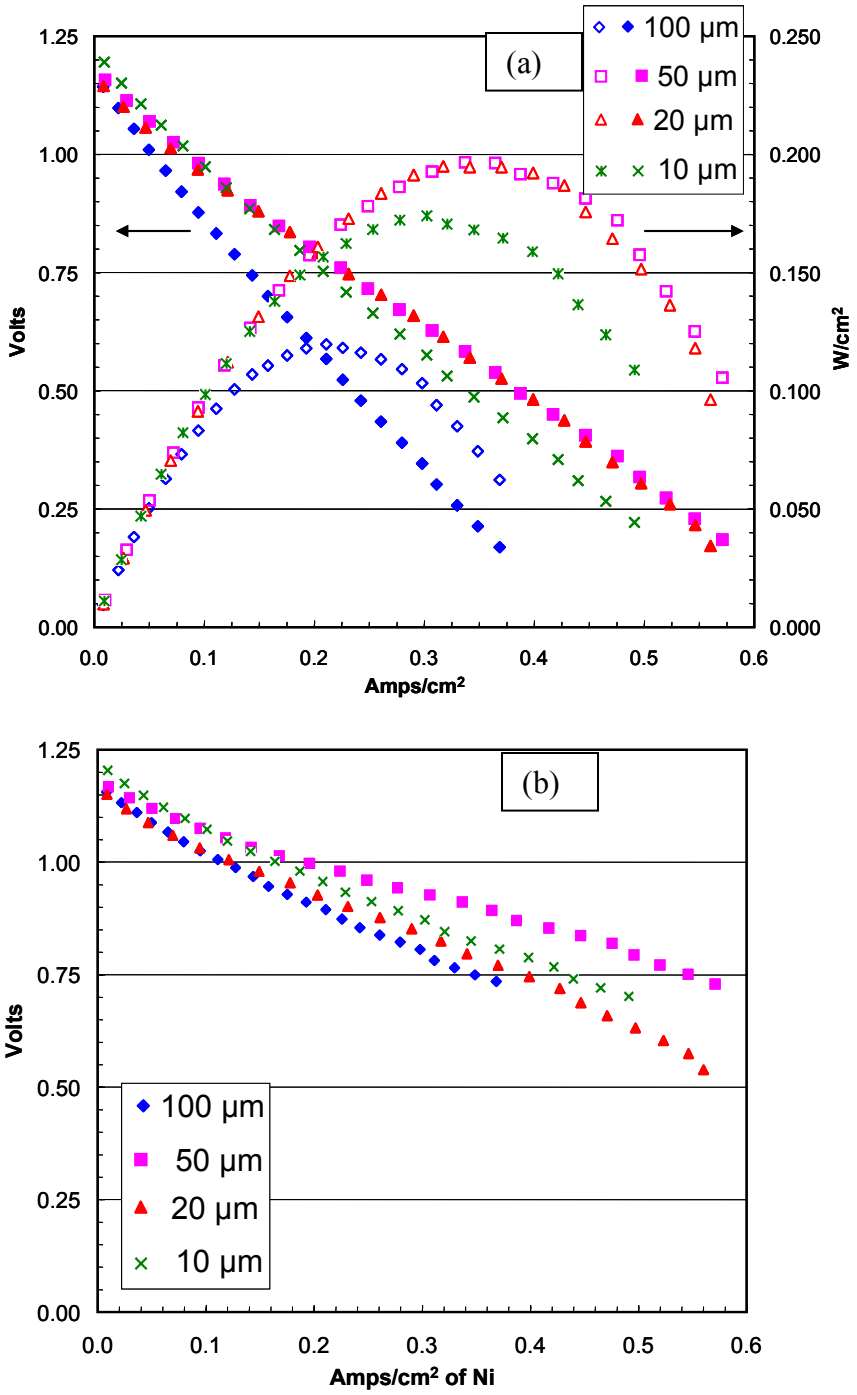

Figure 4.2 – a) Uncorrected V_{cell} and $\dot{w}$ vs. A/cm^2 of Ni for different pattern widths at p_{H2} = 0.33 bar at 850 °C; b) Same corrected $V_{cell} - i^*R_{bulk} - \eta_{cath}$ vs. Amp/cm^2 of Ni for different pattern widths.

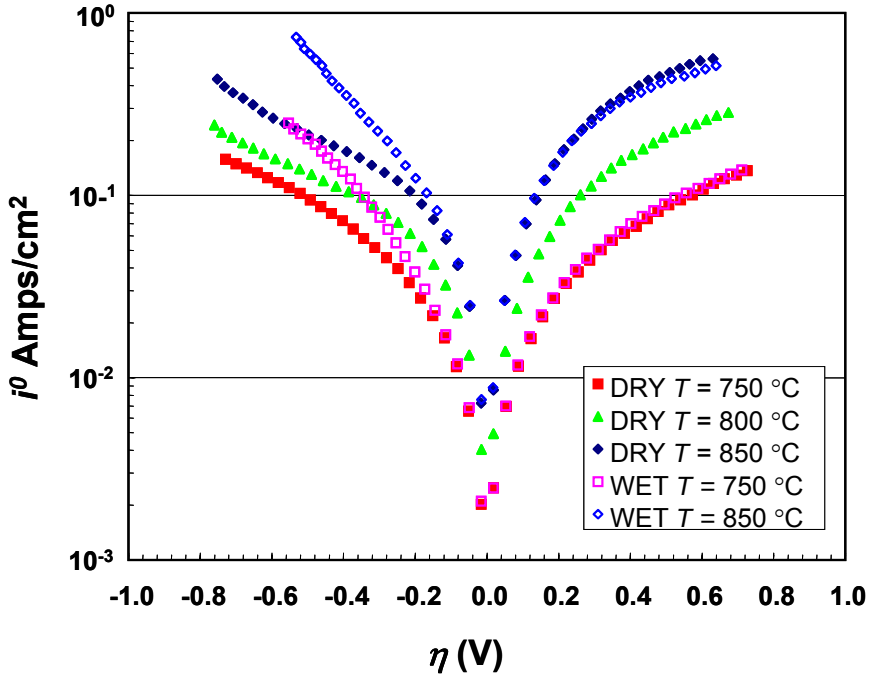

Figure 4.3 – η_a vs. i for T from 750 to 850°C at p_{H2} = 0.3-0.33 bar in both dry and wet (p_{H2O} = 0.03 bar) feeds for the 20 μm pattern. Filled symbols dry and open symbols wet.

Since for most reformed hydrocarbon feeds, H_2 and CO will enter as a mixture into the SOFC anode chamber, it is of interest to know how the two fuels undergo oxidation when mixed together. Thus, the results for pure H_2 electrochemical oxidation on the initially thin Ni patterns (after pattern agglomeration) were compared with H_2/CO mixtures to provide some understanding about how CO influences H_2 electrochemical oxidation. The corrected V-i curves in Figures 4.4 show how an equimolar mixture of CO and H_2 (both with p_k = 0.17 bar diluted in Ar) behaves very similarly to pure H_2 when comparing with Figure 4.2b. This similar behavior is not surprising considering that these experiments were conducted with significant excess fuel such that if H_2 electrochemical oxidation were favored all of the current would not significantly deplete the H_2 reactant pool. Figure 4.5 provides

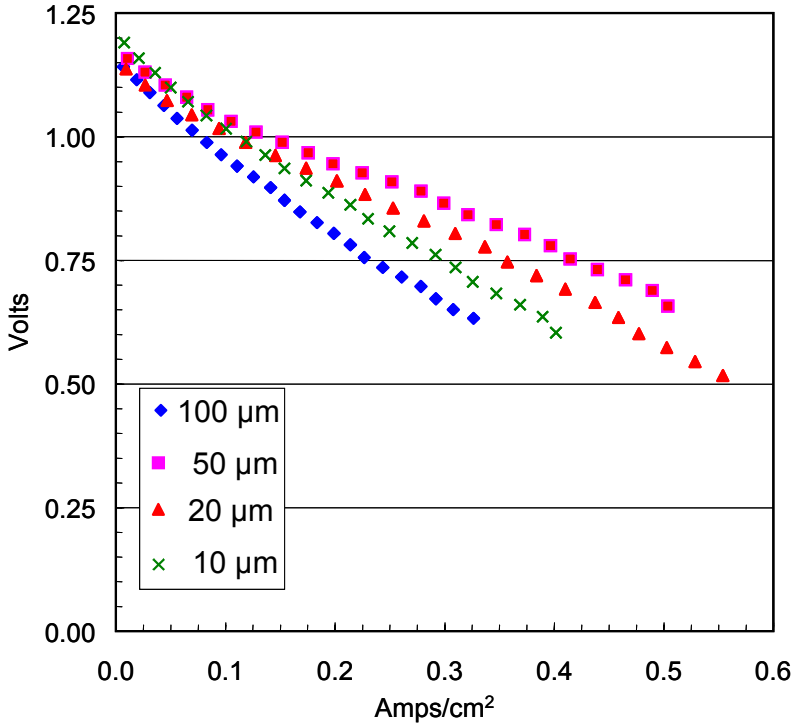

Figure 4.4 – Corrected V_{cell} vs. i based on a_{cat} for patterned anodes with 10, 20, 50 and 100 µm-wide lines. All measurements at 850°C with p_{H2} = 0.167 bar and p_{CO} = 0.167 bar.

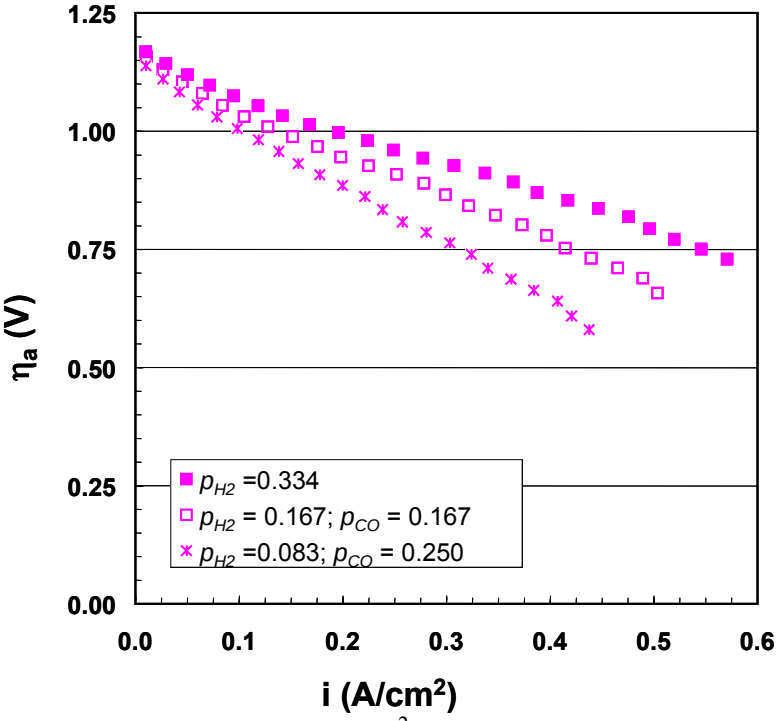

Figure 4.5 – Corrected voltage vs. Amp/cm^2 of Ni patterned anode for 50 µm pattern at T at 850°C for three different anode flow compositions.

the direct comparison of H_2/CO mixture corrected *V-i* curves performance at two different H_2/CO ratios with pure H_2 *V-i* curves. Increasing p_{CO} does reduce the performance particularly at higher *i* which is likely explained by the increased CO site coverage reducing surface diffusion to the TPB at the highest current densities.

In the current experiments, the presence of excess fuel allowed for H_2 oxidation to occur such that CO appears to play a minimal role in the total electrochemical oxidation rates except at relatively high *i*. This has also been observed in porous Ni/YSZ anode experiments [70, 91]. While there is a monotonous decrease in the voltage of the pure H_2 values with increasing CO/H_2 ratios, the decrease is no more than 25% for the 3:1 CO/H_2 mixtures. Excess H_2, with its faster electrochemical oxidation rates, does not permit significant CO buildup on the surface except at higher current densities. As such H_2 reactions dictate the electrochemical oxidation process even when the CO/H_2 ratio is 3:1. An additional factor may also be the water-gas shift reaction which may convert product H_2O and reactant CO to H_2 and CO_2 on the Ni surface.

V-i curves for CO/H_2 mixtures were compared with those from pure H_2 at the same partial pressures as the mixtures where Ar was used in place of the CO fuel component. Comparison of the *V-i* curves for pure H_2 and H_2/CO mixture as well as replaced CO with equal amount of Ar for a 20 μm pattern are shown in Figure 4.6. Similar results were observed for the other patterns. In general, Ar substitution for CO has limited impact on the *V-i* curves with the increasing fall-off in V_{cell} with p_{CO} began to be noticeable at the highest *i*. Thus, CO does not significantly inhibit H_2 electrochemical oxidation under conditions of excess fuel on Ni/YSZ anodes.

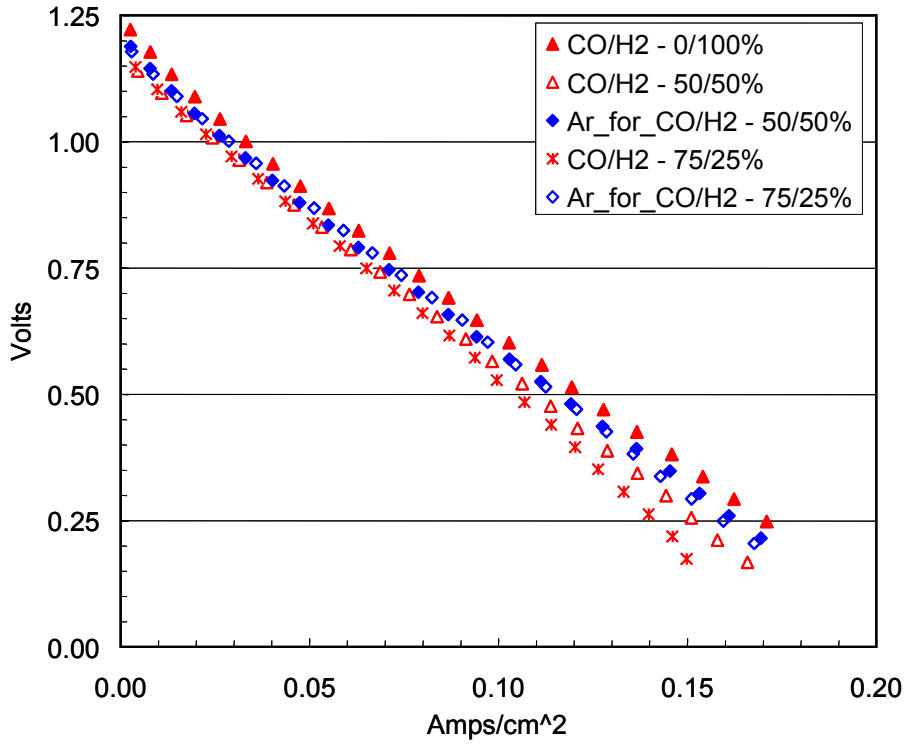

Figure 4.6 – Corrected voltage vs. current density for different CO/H_2 mixtures in Ar diluent at 850 °C for a 20 µm pattern.

The thicker (1 µm) stable Ni patterned anodes showed electrochemical performance that scaled consistently with l_{TPB} and not with a_{cat}. This is to be expected because the thick patterns maintained l_{TPB} at near the original value from the geometric values. As such it was of interest to assess i/l_{TPB} in terms of A/m of TPB with H_2 as the fuel feed. Results from one stable pattern (100 µm line width – Group D) are shown in Figure 4.7 for a range of temperatures. The results provide a basis for approximating fitting parameters not on a per a_{cat} basis but rather on a per l_{TPB} basis. Results in Figure 4.7 show i/l_{TPB} vs. η_a and indicate that based on geometric l_{TPB} values, i/l_{TPB} can readily reach values as high 0.05 A/m of TPB at typically SOFC operating conditions ($\eta_{an} \leq 0.25$ V and $T = 850°C$) and this value provides a basis for assessing the effectiveness of other fuels in comparison to H_2 (as done for CO in chapter 6).

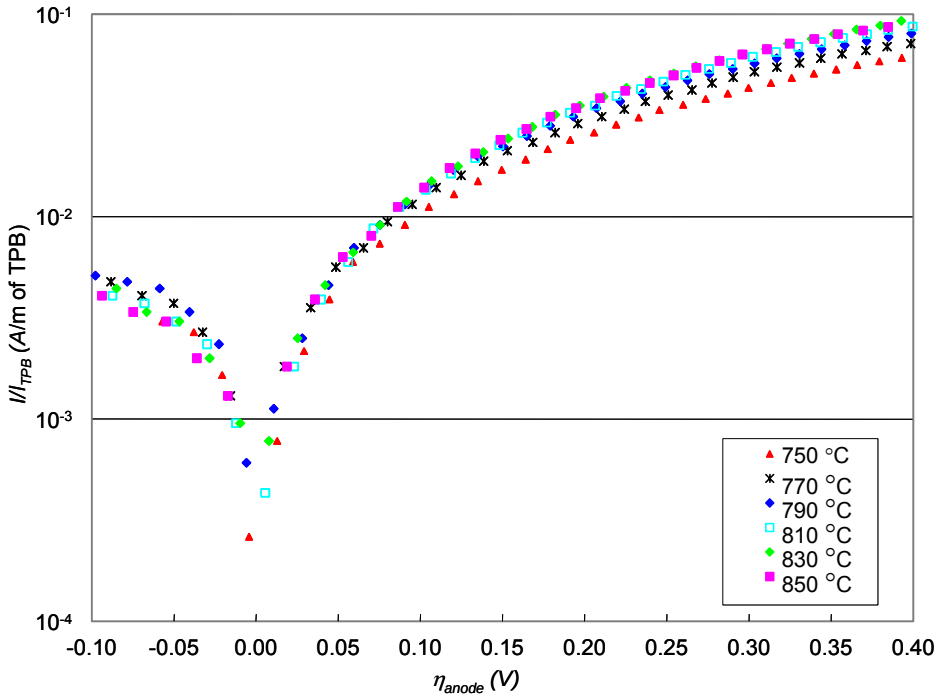

Figure 4.7 – Tafel plots showing i/l_{TPB} vs. $\eta_{act,an}$ for a range of T with constant p_{H2} = 0.32 bar and p_{H2O} = 0.03 bar mixtures in Ar diluent for a 20 µm pattern

4.4. Impedance Measurements

To have a better understanding of the chemical/electrochemical reaction of the H_2 on the Ni surface, along with the polarization studies, impedance spectra were taken across the entire cell for all of the anode feeds and individual patterns at η_a = 0.0 V. To extract the impedance contribution for the anode, the specific impedances of the porous LSM/YSZ cathode were measured in the symmetric cell experiments over the range of relevant T as discussed in previous chapter. The relaxation frequencies for the cathodic processes for three of the spectra plots in Figure 3.10 corresponding to 850, 800 and 735 °C are respectively 33.7, 13.9 and 3.2 Hz, and knowing these frequencies made it feasible to subtract the cathodic impedance of the overall cell impedance as a function of frequency.

Figure 4.8 shows corrected impedance spectra for dry H_2 diluted in Ar at three different T. The figure shows the area specific impedance spectra (based on original Ni film area) for the 50 µm patterned anodes and remaining bulk impedances (after subtracting the cathode impedances). These impedance spectra do not show any diffusion resistance, and thus, after subtracting the cathodic resistance, the remaining polarization loop is due to the charge transfer and surface reactions.

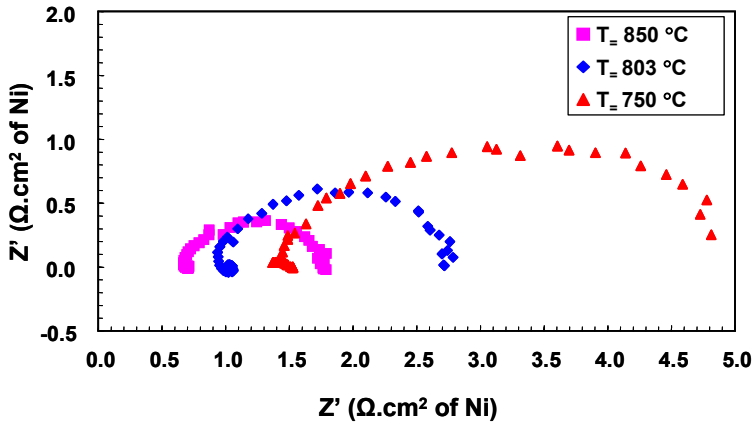

Figure 4.8 – Area specific impedances (including R_{bulk}) for the patterned Ni anode with 50 µm-wide lines at V_{OCV} and with p_{H2} = 0.33 bar and T from 750 to 850°C.

Figure 4.9 shows the area specific impedance (scaled with a_{cat}) for different pattern width at T of 850 °C. Due to the pattern disintegration the impedance does not scale with the l_{TPB}, but instead with a_{cat}. Although 100, 50 and 20 µm are fairly following the width of the pattern, the 10 µm is not showing the same trend. That can be explained by the fact that size of the disintegration is in the order of the width of the pattern likely caused some partial discontinuity in pattern and thus large impedances.

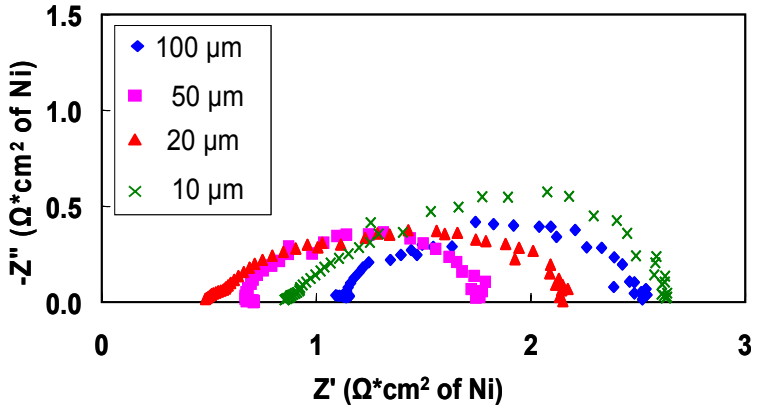

Figure 4.9 – Area specific impedances (including R_{bulk}) for patterned anodes with 10, 20, 50 and 100 µm-wide lines. All measurements at V_{OCV} and with p_{H2} = 0.33 bar and T = 850°C.

4.5. Discussion and Analysis

Data in Figure 4.2b show that at 850 ºC, H_2 electrochemical oxidation maintains a near constant $R_{pol,a}$ with increasing η_a or i. Corrected V-i curves for dry H_2 with the 50 µm Ni pattern, shown in Figure 4.3-b, demonstrate this same trend at lower T down to 750 ºC with the average $R_{pol,an}$ increasing with lower T. The temperature-dependence of $R_{pol,a}$ reveals a rate controlling processes that has a significant E_{act} more characteristic of a reaction process rather than a surface diffusion process. Since the four patterned anodes in those experiments possessed similar a_{cat} as well as similar l_{TPB}/a_{cat} (due to the pattern agglomeration), the results are ambiguous as to whether processes related to a_{cat}, such as adsorption, or related to l_{TPB} , such as charge-transfer reactions, control the H_2 electrochemical oxidation rates. Some studies have suggested that adsorption equilibration processes control H_2 electrochemical oxidation in porous cermet Ni/YSZ anodes for T > 800 ºC [78].

From the simplified Butler-Vollmer equation (Eqs. 2.6-2.7), i_∞^0, E_{act}^0, and β_f can be fitted to find expressions for i^0 as a function of T for a given anode fuel feed

compositions. These fits can be simplified by only fitting high η_a > 200 mV and ignoring the β_r term which is negligibly small at those conditions. Results from such fits for all H_2/CO fuel feeds from the initial thin Ni patterns are summarized in Table 4.1. These results from the fits showed consistent trends for H_2 (as well as CO) electrochemical oxidation. The results for the fits again show a 20% enhancement in i^0 with the addition of H_2O at 750 °C as discussed above.

Table 4.1 – Summary of Tafel plot fitting parameters for high η_a vs. i for average results of all patterns for a range of different H_2/CO fuel mixtures and T.

p_{fuel} (bar)	T (°C)	i^0*100 (A/cm^2 of Ni) (dry / wet)	$\beta_{f,a}$ (dry / wet)	E_{act}^0 for i^0 (dry)
p_{H2} = 0.33	750	4.0 / 4.9	0.24 / 0.27	1.15 eV
	803	7.8	0.27	
	850	12.7 / 14.3	0.29 / 0.27	
p_{H2} = 0.167 p_{CO} = 0.167	750	7.3	0.19	0.45 eV
	802	8.0	0.23	
	847	11.6 / 12.3	0.25 / 0.23	
p_{H2} = 0.083 p_{CO} = 0.25	744	6.4 / 4.4	0.20 / 0.23	0.45 eV
	802	7.1	0.22	
	842	10.4 / 10.9	0.21 / 0.18	

As documented in Table 4.1, i^0 for H_2 oxidation on all of the Ni anodes tested increased with T and was fitted with an E_{act}^0 of 1.15 eV for dry H_2 and a slightly lower value of 0.95 eV for wet H_2. These E_{act}^0 values are slightly higher than those found for lower T measurements in a previous half-cell patterned anode study on sputtered Ni electrodes [5] which shows although these result have been collected from disintegrated pattern, still are reliable for E_{act}^0 calculations. To confirm this, data

for H_2 electrochemical oxidation was taken for the stable thicker Ni patterns (1 μm) with group B geometry as detailed in Table 2.2. In those experiments, T was increased from 750 to 850 °C in 20 °C increments and fuel was diluted H_2 in Ar (p_{H2} = 0.32) with added H_2O (p_{H2O} = 0.03) in the fuel stream. Figure 4.10 shows the i^0/l_{TPB} fits from which E^0_{act} was derived (from data in Figure 4.7) Table 4.2 shows the result of the Tafel fit for high η_a for 100 μm pattern.

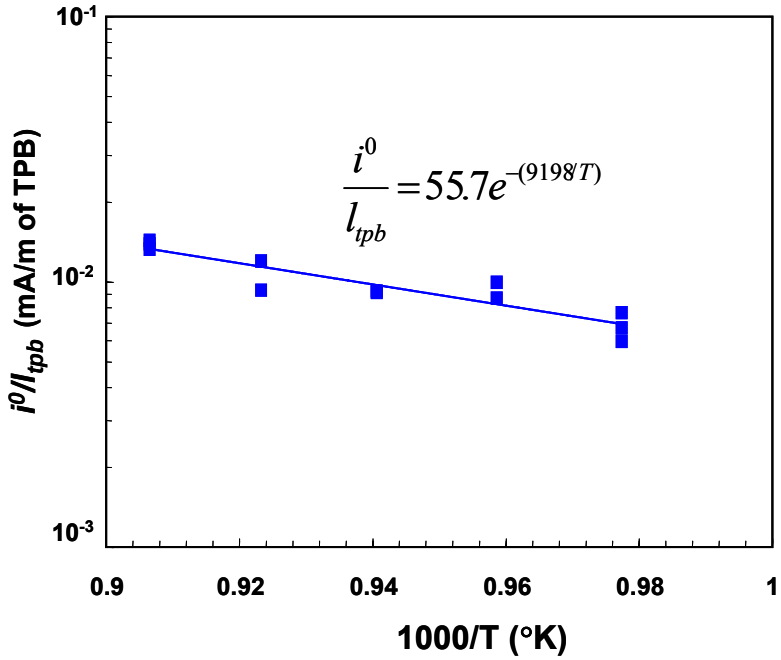

Figure 4.10 – i^0 for the range of T = 750 to 830 °C and p_{H2} = 0.32, p_{H2O} = ~0.03.

Table 4.2 – Summary of Tafel parameters for high η_a vs. i for average results of 100 μm pattern for T from 750 to 850 °C with p_{H2} = 0.32 and p_{H2O} = ~0.03.

T(°C)	i^0*100 (mA/m TPB)	β_f	E^0_{act} for i^0
750	1.425	0.485	1.106
770	1.961	0.488	
790	1.931	0.506	
810	2.239	0.505	
830	2.911	0.491	

Results from Table 4.2 show that E_{act}^{0} can still be extracted from the disintegrated patterns because, although l_{TPB} is not known, it likely scales with a_{cat}. Higher i^{0} in thinner pattern shown in Table 4.3 suggests higher l_{TPB}.

H_2O drives a thermodynamic drop in V_{OCV} for H_2 oxidation but without any reduction in R_{pol} and apparently with a slight increase in the relaxation frequencies of the dominant polarization process. The observed impedance spectra for determining relaxation frequencies are dominated by two processes and fitted to an $[R_1(R_2L_1)(R_3Q)]$ equivalent circuit suggested by Adler [104]. The high frequency inductive loop modeled as (R_2L_1) in parallel and with relaxation frequencies ($\omega_L^* = R_2/2\pi L_1$) $\geq$ 400 Hz for all conditions tested in the current study. The fitted values for R_2, L_1, and the other circuit parameters are shown in Table 4.3. Interestingly, ω_L^* increases with temperature but does not appear to be a strong function of the anode feed composition, and as such it does not provide any insight into the oxidation mechanisms of the fuel species.

The main arc of the anode impedance spectra were fitted most readily with a constant phase element (CPE) in parallel with a resistor in a (R_3Q_1) frequency process. This CPE is associated with the charge transfer processes occurring in the TPB region of the anode. A CPE in parallel with a resistive element gives the following impedance:

$$Z_{(RQ)} = \frac{R_3}{R_3 Y_1 (j\omega)^{n_1} + 1} \qquad \text{(Eq. 4.1)}$$

where n_1 falls between 0 (characteristic of a pure resistive element) and 1. The fitted values for R_3, Y_1, and n_1 for the 50 μm pattern spectra fits are listed in Table 4.4 for

all of the fuels. The relaxation frequencies ω_Q* for the (R_3Q_1) element (where ω_Q* = $1/2\pi(R_QY_o)^{1/n}$) is also listed in Table 4.3 and the values show that for all fuels, temperature increases the relaxation frequency.

Several trends can be observed with ω_Q* as listed in Table 4.3. ω_Q* associated with H_2 oxidation are faster than those for CO/H_2 mixture at the same temperature. Although the 3:1 CO/H_2 mixtures shows a reduced ω_Q* than H_2, it is closer to the value of H_2 than pure CO. As stated earlier, this indicates the preferential oxidation of H_2 in these mixtures and not significant water-gas shift reaction rates.

Table 4.3 – Summary of impedance spectra fitting parameters for a $R_1(R_2L_1)(R_3Q_1)$ circuit with the 50 μm pattern for a range of different H_2/CO fuel mixtures and T at η_a = 0.0 V.

p_k (kPa)	T (°C)	R_1 (Ω∗cm^2)	R_2 (Ω∗cm^2)	L_1 (μH*cm^2)	R_3 (Ω*cm^2)	Y_1*100 (S*s^{n1}*cm^2)	n_1	ω* (Hz)
p_{H2}= 0.33	750	0.96	0.56	223.0	4.28	5.38	0.59	1.9
	803	0.73	0.38	70.2	2.20	3.00	0.75	6.7
	850	0.62	0.13	6.9	1.20	2.45	0.75	17.4
p_{H2}= 0.33 p_{H2O} = 0.03	738	1.31	0.33	90.4	2.76	9.15	0.65	1.3
	782	0.73	0.47	95.0	2.98	2.73	0.62	9.2
	850	0.55	0.22	15.8	1.28	2.14	0.66	37.4
p_{H2}= 0.083 p_{CO}= 0.250	750	0.40	0.65	178.0	2.82	5.19	0.66	2.9
	802	0.71	0.37	66.7	2.52	2.83	0.74	5.6
	842	0.68	0.16	8.2	2.42	1.76	0.77	9.3
p_{H2}= 0.083 p_{CO}= 0.250 p_{H2O} = 0.03	738	1.31	0.35	82.7	3.45	10.38	0.53	1.1
	850	0.63	0.17	12.0	1.99	1.21	0.74	24.2

A final trend is observed in the impedance fits is the consistent increase in ω_Q* with the addition of H_2O. This effect can be explained by the fact that increasing p_{H2O} increases i^0 as suggested by equation 4.2. Zhu et al. assume surface equilibrium with a rate-controlling charge transfer reaction to derive an expression for i^0 from an elementary reaction mechanism involving reactions 1.7 and R.1.9 – 11. The expression shown here indicates a dependency of i^0 on p_{H2O} and p_{H2}:

$$i^0 = i^*_{H2} \frac{\left(p_{H2} / p^*_{H2}\right)^{1/4} \left(p_{H2O}\right)^{3/4}}{1 + \left(p_{H2} / p^*_{H2}\right)^{1/2}} \qquad \text{(Eq. 4.2)}$$

In equation 4.2, parameter p^*_{H2} depends on H_2 adsorption/desorption rates, and i^*_{H2} is derived from parameters associated with the charge-transfer reactions.

The acceleration of processes due increased p_{H2O} does not translate into lower $R_{pol,a}$ as can be seen by the similarity of the impedance magnitudes for dry and wet cases in Figures 4.10 and 4.11. However, consistently the addition of ~3% H_2O to the fuel feed increases ω_Q* at η_a = 0.0 V and in particular at $T \geq$ 800 ºC. It is not clear whether this acceleration is derived from a dissociative activation of H_2O on the Ni or YSZ surface in the TPB region. A more definitive understanding of the impedance spectra and the observed trends requires detailed model development which will allow for multi-step kinetic processes to be considered and such an effort in collaboration with others is being undertaken [111]. *In situ* surface Raman spectroscopy may also provide a valuable tool for identifying long-lived adsorbates on Ni and YSZ surfaces during electrochemical oxidation as a function of p_{H2O}.

5. CO Electrochemical Oxidation

Understanding the CO oxidation in SOFC's is of a great importance. SOFC's are capable of using light and even heavy hydrocarbons. CO is one of the products in the process of gasification in the form of coal gas; also in the process of steam reforming there is CO available in the syngas. There are uncertainties about the oxidation processes for CO in SOFC anodes particularly with high CO concentration such as coal gas. These uncertainties are in the role of water gas shift in oxidation of CO versus CO electrochemical oxidation at the catalyst surface. In either case there are several physical, chemical and electrochemical steps that could happen when CO molecule meets the catalyst surface. Electrochemical oxidation of dry CO on Ni/YSZ SOFC anodes involves several steps which likely include:

- non-dissociative CO adsorption on the Ni surface
- surface diffusion of CO toward the TPB
- O^{2-} transport to the TPB on the electrolyte surface
- charge-transfer reactions involving transfer of two electrons from YSZ to Ni by reacting O^{2-} ions with CO to form CO_2

Electrochemical oxidation rates of CO on Ni/YSZ have been reported to range from 3X to an order of magnitude lower than rates of H_2 [74]. Thus, for the same i higher η_{anode} are required for CO oxidation in comparison to H_2 oxidation on Ni-based electrodes [70]. Some have postulated that the adsorbed CO oxidation by O^{2-} from the electrolyte is the rate-limiting step except under low CO concentrations

when gas diffusion becomes slow [112, 113]. Similar proposals have been put forth for CO electrochemical oxidation on Pt/YSZ electrodes [71].

The voltammetry and impedance measurement in this chapter try to address the oxidation pathway of the CO on Ni anode in SOFC's. The experiments and patterned anode model presented in chapter 6 are designed to elucidate how the various steps listed above may play a role in the CO electrochemical oxidation process in Ni/YSZ SOFC anodes.

5.1. Review of Past Results

Although fewer in number than H_2 electrochemical oxidation studies, some studies have explored CO oxidation on Ni/YSZ porous anodes [70, 74]. The limited published results on CO electrochemistry do not provide a conclusive story as to the controlling mechanisms for CO electrochemical oxidation. In this section, a brief overview of the previous research on CO oxidation will be presented.

Holtappels et al. [74] studied the electrochemistry of CO/CO_2 oxidation on Ni/YSZ cermet as a function of p_{CO} and p_{CO2} at 1000 °C. The CO/CO_2 ratio was kept < 20 to avoid carbon deposition due to Bouduard reaction (reaction 1.5). Further, to prevent the Ni/YSZ anode from forming NiO at high oxygen activities, the CO/CO_2 ratio was kept > 0.2. Holtappels et al. suggested that CO electrochemical oxidation reaction is more than an order of magnitude slower than H_2 oxidation. Holtappels et al. speculated that the differences in electrochemical oxidation rates of CO and H_2 in porous anodes are caused primarily by difference in gas-phase mass transfer resistance of the fuels at 750 °C, and by difference in both the mass transfer and charge transfer resistances at 1000 °C. These results supported qualitative

observations but did not provide adequate data for quantitative rates for reaction steps in the electrochemical oxidation of CO.

In related research Mizusaki et al.[71] studied CO oxidation in Pt/YSZ porous electrodes with 8% mole Y_2O_3 doped ZrO_2 (YSZ) for T between 600 and 1000 °C and CO/CO_2 ratios between 1 to 10^{-4}. A plot of p_{CO} vs. i in logarithmic scale suggested that the forward charge transfer coefficient $\beta_f = 0.5$ which they interpreted to indicate reaction rates controlled by a simple charge transfer step at the TPB as also proposed in this study for Ni/YSZ anodes.

$$CO_{Pt} + O^{2-}_{YSZ} \leftrightarrow CO_{2,Pt} + []_{YSZ} + 2e^-_{Pt(b)} \qquad \text{(R. 5.1a)}$$

In another study on porous Ni/YSZ anodes, Matsuzaki and Yasuda [75] explored a wide range of experiments with various combinations of H_2, H_2O, CO and CO_2 at different T. According to this study, electrochemical oxidation rates of H_2 in the interface of Ni/YSZ porous anode are only about 2X those of CO, which is significantly less than the reported order of magnitude ratio by Holtappels et al. [74]. Equivalent circuit analysis was used to detail specific resistances, but there is much uncertainty in interpreting the results of these fits due to the significant mass transport limitations in those experiments. As such the observed variation in the differences in electrochemical oxidation rates between CO and H_2 remain unresolved.

Weber et al. [70] have compared electrochemical oxidation in porous Ni/YSZ anodes for H_2, CO, and CH_4 as well as mixtures of these fuels. For pure CO, they did not observe long-term stable operating condition. In short period of time CO electrochemical oxidation experiments, carbon deposition and micro-structural changes were observed within the anode which would lead to delamination of the

anode from the electrolyte. To overcome these issues the authors suggest to use appropriate steam/carbon ration in fuel use the cell under adequate current density which delivers sufficient amount of oxygen to the anode surface. This result suggests that anode microstructure as well as p_{H2O} may significantly impact an SOFC's ability to operate on high p_{CO} fuel streams.

Of all the previous research on CO electrochemical oxidation in porous Ni/YSZ SOFC anodes, Lauvstad et al. [72, 73] have conducted the most thorough study. Analysis of their experiments on both Ni/YSZ and Pt/YSZ anodes led to the suggestion of different possible mechanisms for CO electrochemical reaction on Pt and Ni surface [72] which can be summarized as follows. In these equations, Ni can be replaced by Pt.

Model 1 and 2) Charge transfer with O^{2-} ions going to anode and atomic O available for oxidation of gaseous CO (Model 1) or adsorbed CO (Model 2) with adsorbed atomic O on the metal surface:

$$O^{2-}_{YSZ} \leftrightarrow O_{Ni} + []_{YSZ} + 2e^{-}_{Ni(b)} \quad \text{(R. 5.2)}$$

$$CO + O_{Ni} \leftrightarrow CO_2 + []_{Ni} \quad \text{(R. 5.3)}$$

$$CO + []_{Ni} \leftrightarrow CO_{Ni} \quad \text{(R. 5.4)}$$

$$CO_{Ni} + O_{Ni} \leftrightarrow CO_2 + 2[]_{Ni} \quad \text{(R. 5.5)}$$

Model 3) Oxidation of adsorbed CO by O^{2-} ions at a phase boundary interface is described by Reactions 5.4 and 5.1b:

$$CO + []_{Ni} \leftrightarrow CO_{Ni} \quad \text{(R. 5.4)}$$

$$CO_{Ni} + O^{2-}_{YSZ} \leftrightarrow CO_{2,Ni} + []_{YSZ} + 2e^{-}_{Ni(b)} \quad \text{(R. 5.1b)}$$

Inclusion of surface diffusion of CO with model 3) also provides an additional process to consider, but the effects of surface diffusion can be readily incorporated into any of the above models.

In the second part of their report [73], Lauvstad et al. analyzed experiments on point electrodes of Ni and Pt on YSZ surfaces under different CO/CO_2 mixtures and a range of T. The microelectrodes removed gas-phase mass transport from the impedances and allowed for clearer analysis of electrochemical oxidation rates much in the same way that the patterned anode experiments in the current study have done. Their analysis of the impedances from these microelectrode experiments suggested that mechanism 2 best explains the results from their experiments, but the arguments used were not convincing and this interpretation has been questioned here. The lack of any Warburg impedance was interpreted to mean an insufficient supply/removal rates by adsorption/desorption processes at the TPB. They also noticed that for Ni anodes, decreasing CO_2/CO ratios at constant p_{CO} increases the $R_{pol,a}$.

In a final study, Costa-Nunes et al. [62] compared two different anodes (Ni/YSZ and Cu-CeO_2-YSZ) working with H_2, CO and syngas fuel feeds. They conclude that the higher activity for H_2 is due to the spillover of H atoms from the Ni to the YSZ surface. On the other hand, such spillover is assumed to not occur with the more strongly absorbed CO. Thus, the charge transfer processes for H_2 electrochemical oxidation are significantly different than that of CO. This difference is critical for design of Ni-based anode microstructures for SOFC applications that will operate well on gases derived from coal gasification or reformers. It is for this reason that CO electrochemical oxidation was studied with patterned Ni anodes here.

5.2. Experimental Conditions

To ensure relatively stable pattern geometry, all experiments reported in this chapter used 1 μm thick Ni patterns for evaluating CO electrochemical oxidation. As discussed earlier, 1 μm thick Ni patterns maintained their structure during electrochemical oxidation up to at least 800 °C [77] . In the current study, T remained ≤ 800 °C. Most of the experiments performed with CO electrochemical oxidation utilized the group B set of patterned electrodes as described in Table 2.2 and further in chapter 3. The set of Group B patterns are shown in Figure 5.1 and are designed to have equal l_{TPB} and equal a_{elec} while the a_{cat} varies in patterned electrodes.

Overall, 15 membrane electrode assemblies with the patterned electrodes sketched in Figure 5.1 were used to explore of CO electrochemical oxidation.

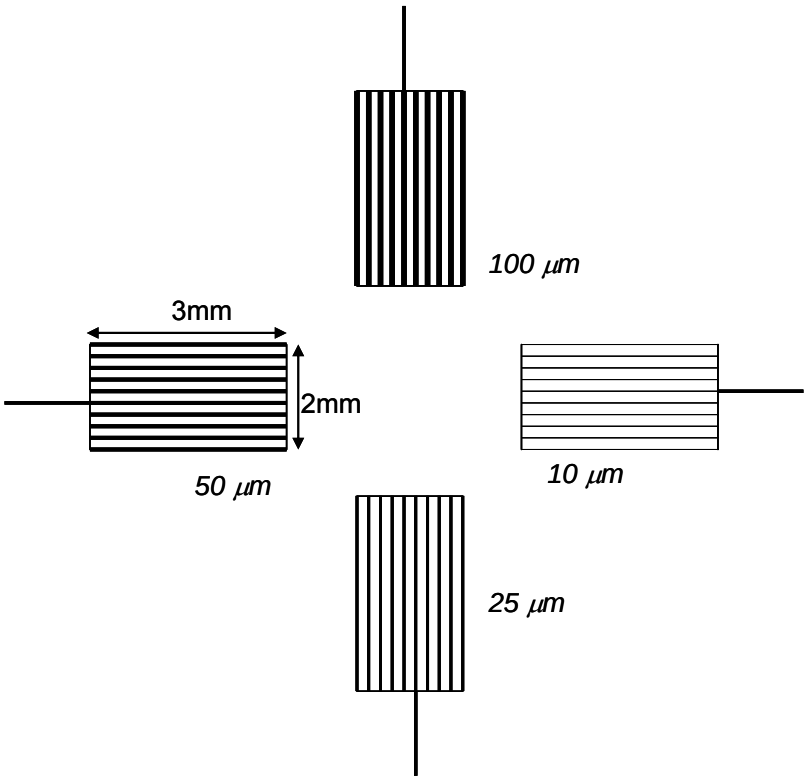

Figure 5.1 – The pattern geometry with equal l_{TPB} and a_{elec} and varying a_{cat} according to Group B detailed in Table 2.2.

To evaluate the repeatability of the CO electrochemical oxidation measurements, an error investigation was performed on data taken from different MEA's using the stable 1 μm thick Ni patterned anodes. Table 5.1 shows the result of the repeatability analysis for both dry and wet CO fuel feeds for a 100 μm pattern from the group B pattern tested at T = 725 °C. Since all the represented data are taken from the same group of pattern and the same width of the pattern, to compare these data, they are neither scaled nor averaged based on surface area. On the other word these data are totally raw data and are not representing area specific values. From these data, it is clear that current produced at different η_{tot} are within a reasonable range with standard deviation, σ_{dev} <= 0.1. The low σ_{dev} shows that for the stable patterned anodes, current vs. η_{tot} remains relatively stable with time and between different MEA's. This is in part because current is controlled by the thick bulk electrolyte resistance which as shown in Table 5.1 remained consistent from MEA to MEA. However, R_{pol} at η_{tot} = 200 and 300 mV also was shown to be relatively consistent between MEA's. On other hand, there is a wide variation in the R_{pol} at V_{OCV} between MEA's. The wide variation in R_{pol} at V_{OCV} can be explained by small leakage currents for the MEA's with reduced V_{OCV}. Small leakage currents greatly reduce $\eta_{act,an}$ for small currents around the measured OCV and this has a significant impact on R_{pol} at V_{OCV}. The trends in Table 5.1 are consistent with this interpretation, and the reduced measured V_{OCV} for the 3rd and 4th MEA's listed in Table 5.1 explain their lower R_{pol} at this measured V_{OCV}.

The relative consistency in the electrolyte-dominated R_{bulk} for the different MEA's is illustrated in the Table 5.1. The observed variation in R_{bulk} may be due to

variations in the leads as well as variation in electrolyte thickness or effective a_{elec}. Also, possible leakage currents which may have caused the unexpectedly low V_{OCV} may have also impacted R_{bulk} to some extent. Only MEA's with R_{bulk} and V_{OCV} within an acceptable range were considered as worthy of testing and those MEA's are the ones listed in Table 5.2 and presented in this study. Table 5.2 shows the experiments (numbered by the MEA) that were used to assess the effect of p_{CO2} and p_{H2O} for a range of temperatures between 700 and 800 °C. In this chapter, a set of experiments will be referred to by the MEA number.

Electrochemical impedance spectroscopy (EIS) and voltammetry measurements have been performed as the primary tools to investigate the electrochemical behavior of the CO oxidation. While doing these measurements it was noted to avoid Ni anode oxidation by keeping the anodic overpotential < 400 mV both in impedance spectroscopy and in sweep voltammetry as it was discussed in chapter 3.

Table 5.1 – Error range calculated from the raw data taken for one point (100 µm and T = 725 °C) measured from different MEA's of the same pattern group B

	V_{OCV}	i (mA)		R_{bulk} (Ω)			R_{pol} (Ω)		
		at η_{tot} = 200 mV	at η_{tot} = 300 mV	at V_{OCV}	at η_{tot} = 200 mV	at η_{tot} = 300 mV	V_{OCV}	at η_{tot} = 200 mV	at η_{tot} = 300 mV
T =725 °C; 100 µm from pattern group B									
p_{H2O} = 0.0 bar	0.92	0.551	1.051	54.24	54.41	54.17	1184.7	165.8	139.7
	0.93	0.518	1.018	54.56	N.D.	N.D.	1458.4	N.D.	N.D.
	0.84	0.734	N.D.*	45.85	45.16	46.11	354.1	184.6	146.0
	0.84	0.692	N.D.	46.13	45.54	52.53	363.9	176.9	227.7
Mean	**0.887**	**0.624**	**1.034**	**50.20**	**48.37**	**50.94**	**840.3**	**175.8**	**171.1**
Std. Dev.	**0.048**	**0.105**	**0.023**	**4.86**	**5.23**	**4.26**	**566.9**	**9.4**	**49.1**
Std. err.	**0.024**	**0.053**	**0.017**	**2.43**	**3.02**	**2.46**	**283.4**	**5.4**	**28.3**
T =725 °C; 100 µm from pattern group B									
p_{H2O} = 0.03 bar	0.93	0.614	1.164	52.85	52.27	52.40	922.5	155.9	110.5
	0.93	0.634	N.D.	51.92	N.D.	N.D.	1265.0	N.D.	N.D.
	0.82	0.490	N.D.	60.99	59.77	N.D.	162.8	90.8	N.D.
	0.81	0.654	N.D.	59.58	N.D.	N.D.	290.2	N.D.	N.D.
Mean	**0.87**	**0.598**	**N/A**	**56.33**	**56.02**	**N/A**	**660.1**	**123.4**	**N/A**
Std. Dev.	**0.069**	**0.074**	**N/A**	**4.62**	**5.31**	**N/A**	**552.4**	**46.1**	**N/A**
Std. err.	**0.035**	**0.037**	**N/A**	**2.31**	**3.75**	**N/A**	**261.2**	**32.6**	**N/A**

*N.D.: No data was collected for this point

.

5.3. Voltammetry Studies

Of the tests listed in Table 5.2, MEA 12 provided the highest quality data in terms of repeatability and consistency amongst trends. Figure 5.2 shows uncorrected V_{cell} and power density ($\dot{w} = V_{cell}*i$) vs. i based on a_{cat} of the MEA 12 cell for 100 μm pattern at different T for dry (5.2a) and wet with p_{H2O} = 0.025-0.028 bar (5.2b) conditions. Tafel plots for the dry CO/CO_2 mixtures for the same range of T with the 100 μm Group B pattern can be seen in Figure 5.3. Larger activation overpotentials are seen for the dry case in comparison to the wet case. This effect of H_2O addition also resulted in increased i for a given cell overpotential and thus an increase $\dot{w}$ for the wet case in comparison to the dry case.

The presence of H_2O in the CO feed may result in H_2O dissociation on the Ni surface and the formation of OH_{Ni} and H_{Ni}. This may enhance charge transfer reaction rates when H_{Ni} reacts with O^{2-}_{YSZ} at the TPB. These adsorbates may also cause heterogeneous water-gas-shift reaction to drive CO_{Ni} from the surface as CO_2.

Table 5.2 – The conducted experiments on Pattern Group B for *CO* electrochemistry on the *Ni* surface at SOFC.

	MEA 0	**MEA 2**	**MEA 4**	**MEA 5**	**MEA 12**	**MEA 13**
***T* °C**	750	700 – 725 – 750	700 – 725 – 750	700 – 725 – 750	700 – 725 – 750 -775	775
p_{CO} range	0.33	0.27 – 0.17 – 0.07	0.30	0.267 & 0.260	0.323 & 0.315	0.3333
p_{CO2} range	0	0.07 – 0.17 – 0.27	0.03	0.066 & 0.065	0.032	0.0017-0.0033-0.005-0.0083-0.0167-0.0333-0.0833
p_{H2O} range	0.01	0	0	0 & ~0.025	0 & ~0.025	0
p_{Ar} (diluent)	0.66	0.66	0.67	0.667 & 0.652	0.645 & 0.63	0.6650-0.6333-0.6617-0.6583-0.6500-0.6333-0.5833
η_{tot} (mV)	0	0 – 100	0 – 300	0 – 200	0 – 300	0
Anode flow (sccm)	300	300	450	450	620	600
Cathode air flow (sccm)	400	400	400	400	600	600
Working patterns (µm)	10-25-50	10-25-50-100	10-50-100	10-25-50-100	100	100

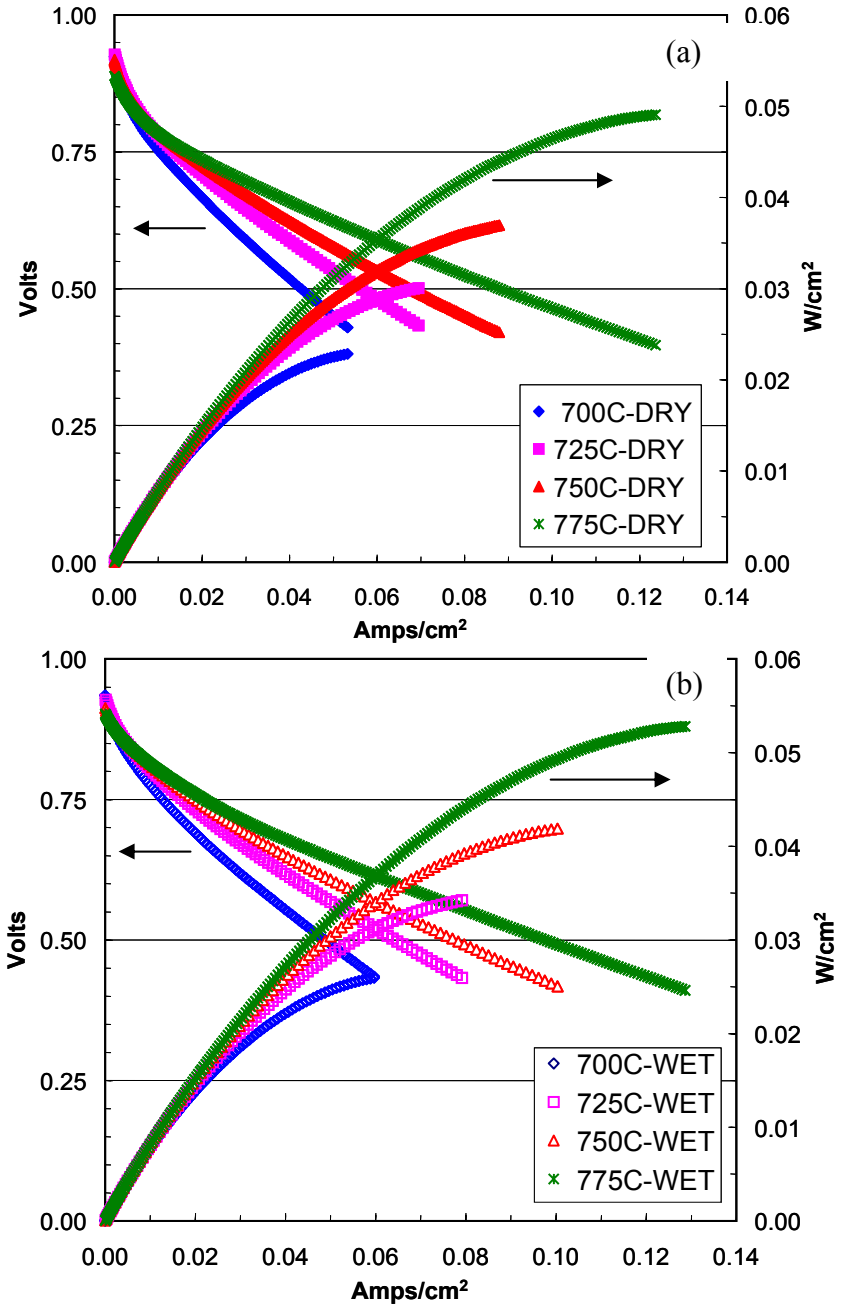

Figure 5.2 – Uncorrected V_{cell} and $\dot{w}$ vs. i base on a_{cat} Ni for 100 µm width Ni patterned anodes. **a)** $p_{CO} = 0.323$ and $p_{CO2} = 0.032$; **b)** $p_{CO} = 0.315$, $p_{CO2} = 0.032$, and $p_{H2O} = \sim 0.025$.

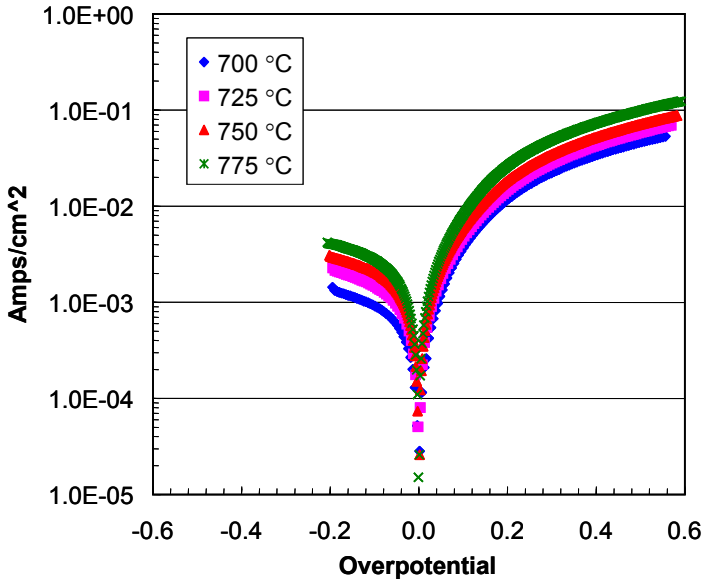

Figure 5.3 – Tafel plot for pattern 100 μm at T ranging from 700 to 775°C. Fuel: p_{CO} = 0.323; p_{CO2} = 0.032

The CO electrochemical oxidation V-i data were fitted to the simplified Butler-Vollmer equation (Eqs. 2.6 and 2.7). A MATLAB code was written and used a least-squares algorithm to fit $\eta_{act,a}$ and $\eta_{conc,a}$ to their forms provided in equations 2.6 and 2.8. Since $\eta_{conc,a}$ for the patterned anodes was typically quite small the discussion will focus on the fit for $\eta_{act,a}$ whose fit with respect to i was determined from the implicit equation 2.6.

$$i = i^0\left[\exp\left(\frac{\beta_f nF\eta_{act}}{\bar{R}T}\right) - \exp\left(-\frac{\beta_r nF\eta_{act}}{\bar{R}T}\right)\right] \qquad \text{(Eq. 2.6)}$$

Since i^0 will vary with T (via an E_{act}) and p_k of reactants and products, i^0 is fitted when possible to an expression of the form

$$i^0 = i^0_\infty \exp\left(-\frac{E^0_{act}}{\bar{R}T}\right)\prod_k\left(\frac{p_k}{\bar{R}T}\right)^{n_k} \qquad \text{(Eq. 2.7)}$$

where n_k are empirically derived power dependencies.

Fits to find the governing parameters for calculating $\eta_{act,a}$ provided β_f and β_r as well as i_∞^0 and E_{act}^0. In many cases, the β_r fits did not show high sensitivity to the data and as such, simpler fits ignoring the second term in the brackets in Eq. 2.6 and just fitting the high η_a > 200 mV to equation 3.2 provided more consistent data. As such, the fits for the Tafel plots for all experiments done on MEA 12 are summarized in Table 5.3. Also, Figure 5.4 shows how E_{act}^0 is extracted from the data for i^0 for both dry and wet cases. These results from the fits showed a consistent 10% increase in i^0 with the 3% addition of H_2O.

Table 5.3 – Summary of Tafel plot fitting parameters for high η_a vs i^o for average results of 100 μm pattern, for the range of T from700 to 775 °C; p_{CO}/p_{CO2}: 10

p_k (bar)	T (°C)	i^0*100 (mA/m^2)	β_{anode}	E_{act} for i^o (eV)
p_{CO} = 0.322 p_{CO2} = 0.032 p_{H2O} = 0.0	700	0.193	0.60	1.49
	725	0.258	0.60	
	750	0.332	0.60	
	775	0.585	0.61	
p_{CO} = 0.322 p_{CO2} = 0.032 p_{H2O} = 0.023	700	0.225	0.60	1.64
	725	0.329	0.60	
	750	0.485	0.59	
	775	0.612	0.60	

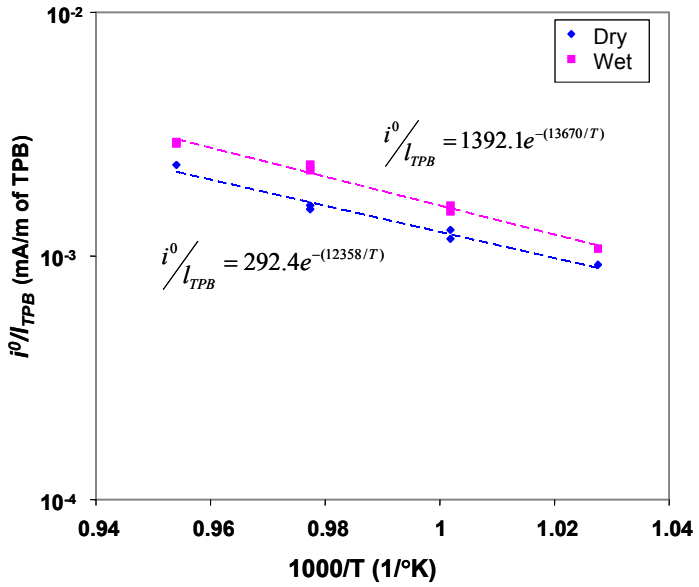

Figure 5.4 – i^0/l_{TPB} vs. $1000/T$ (°K) to find E^0_{act} d for MEA 12 over T = 700 to 775 °C. for feeds dry: p_{CO} = 0.323 and p_{CO2} = 0.032 and wet: p_{CO} = 0.315, p_{CO2} = 0.032, and p_{H2O} = ~0.025;

MEA 12 generated the highest quality data but similar trends within expected margin of error were observed from other tested MEA's with other 1 μm thick patterned anodes. The range of maximum i/l_{TPB} for other electrodes did not always match that of MEA 12, other MEA's were tested and fitted. In an earlier attempt data taken with MEA 5 was fitted, and because of the scattered data, the E^0_{act} for the wet case was almost 25% higher than observed values from MEA 12. Figure 5.5 and Table 5.4 show the fitted data to the data taken from MEA 5. At this point a side by side comparison between data taken from MEA 12 with CO/CO_2 mixture fuel and MEA 1 with H_2/H_2O fuel mixture could help to compare the critical electrochemical reactions of each fuel. Data for MEA 1 was shown and discussed in chapter 4, although not as MEA 1 in that chapter. Figure 5.6 shows the i^0/l_{TPB} plot vs. T for both cases and Table 5.5 has listed the fit parameters including β_f and E^0_{act}.

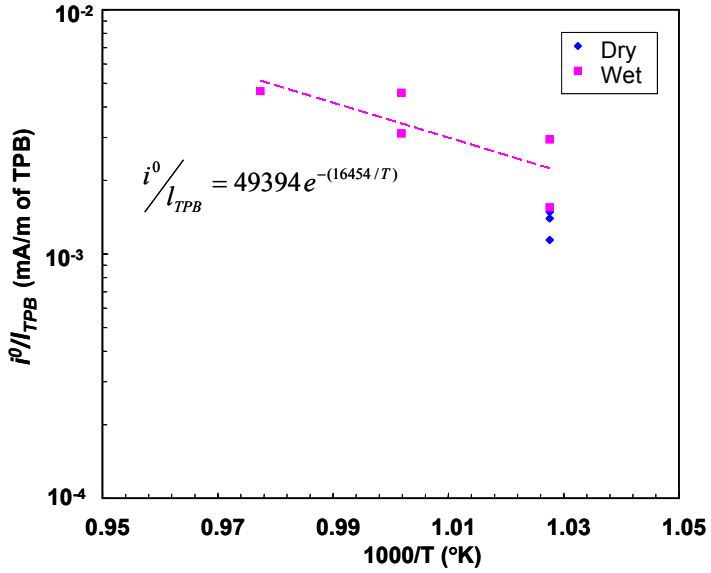

Figure 5.5 – i^0/l_{TPB} vs. 1000/T (°K) to find E^0_{act} d for MEA 5 over T = 700 to 750 °C for feeds dry: p_{CO} = 0.267 and p_{CO2} = 0.066 and wet: p_{CO} = 0.260, p_{CO2} = 0.065, and p_{H2O} = 0.025

Table 5.4 – Summary of Tafel plot fitting parameters for high η_a vs i^0 for average results from MEA 5, for the range of T = 700 to 750 °C.

p_{fuel} (kPa)	T (°C)	i^o*100 (mA/m^2)	β_{anode}	E_a for i^o(eV)
p_{CO} = 0.267 p_{CO2} = 0.066 p_{H2O} = 0.0	700	0.355	0.599	-
p_{CO} = 0.260 p_{CO2} = 0.065 p_{H2O} = 0.026	700	2.044	0.599	1.98
	725	1.185	0.556	
	750	0.941	0.588	

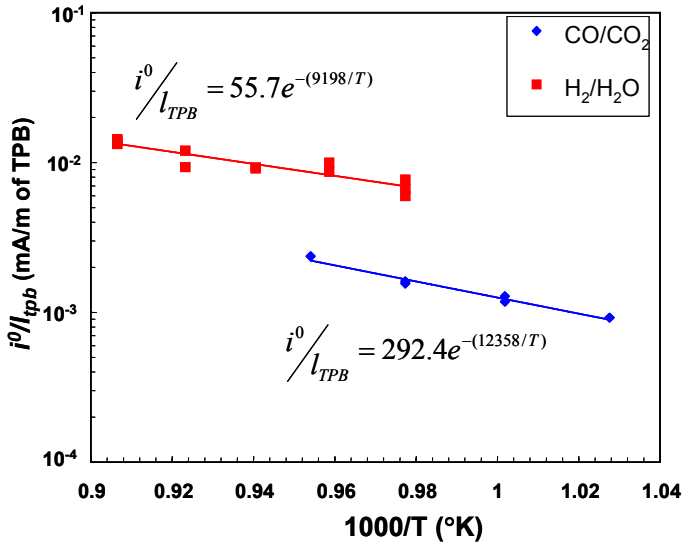

Figure 5.6 – Comparison of i^0/l_{TPB} vs. $1000/T$ (°K) for a CO/CO_2 feed with p_{CO} = 0.323 and p_{CO2} = 0.032 and for H_2/H_2O feed with p_{H2} = 0.308 and p_{H2O} = 0.025

Table 5.5 – Summary of Tafel fit parameters for high η_a vs. i for average results of all 100 µm pattern for two fuel feeds p_{H2} = 0.308 with p_{H2O} = 0.025 and p_{CO} = 0.323 with p_{CO2} = 0.032.

T (°C)	i^0*100 (mA/m TPB)		β_f		E^0_{act} for i^0 (eV)	
	H_2/H_2O	CO/CO_2	H_2/H_2O	CO/CO_2	H_2/H_2O	CO/CO_2
700	-	0.193	-	0.600	1.11	1.49
725	-	0.258	-	0.601		
750	1.425	0.332	0.485	0.600		
770	1.961	-	0.488	-		
775	-	0.585	-	0.611		
790	1.931	-	0.506	-		
810	2.239	-	0.505	-		
830	2.911	-	0.491	-		

Higher i vs. η_a for H_2/H_2O mixture was expected. Also, β_f for H_2/H_2O mixture is around 0.5, while for CO/CO_2 mixtures β_f is closer to 0.6.

5.4. Impedance Measurements

EIS during CO oxidation on the Ni surface in SOFC anodes was performed at various conditions applied on the MEA's as listed in Table 5.2 will result in different responses in impedance spectra and the comparison along with further modeling and curve fitting will help to elucidate possible processes and their dependency to each variable. Figure 5.7 shows an uncorrected impedance plot for the 100 µm pattern at four different T under OCV conditions. The overall $R_{pol,a}$ for CO electrochemical reaction are about 3X bigger values than the same condition for H_2. For this reason the cathodic resistance is even a smaller fraction of the overall $R_{pol,a}$ for CO electrochemical reaction. Figure 5.8 shows impedance spectra for the 100 µm pattern at T = 775 °C and OCV. Comparing the corrected and uncorrected data shows the impact for the cathodic resistance.

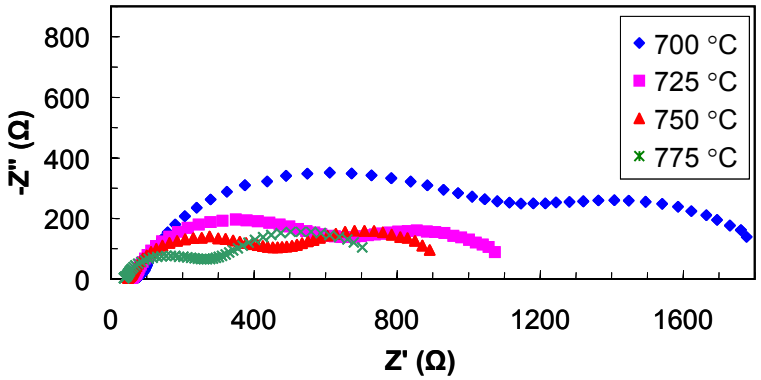

Figure 5.7 – Uncorrected cell impedance spectra for 100 µm pattern at different T at V_{OCV}.

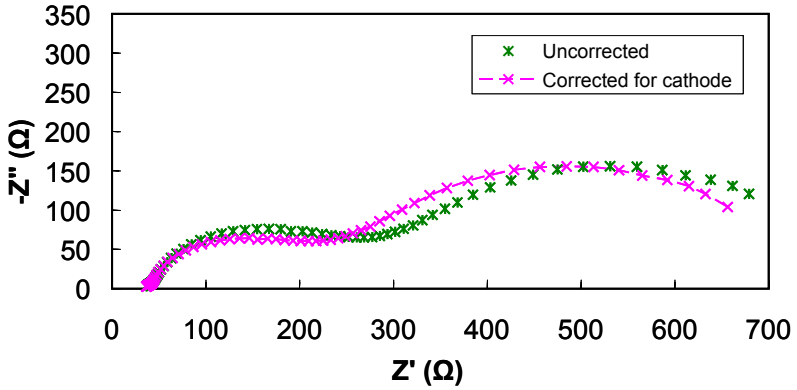

Figure 5.8 – Cell impedance spectra for 100 µm pattern at 775 °C at V_{OCV}; Uncorrected and corrected for cathodic impedance

Both uncorrected and cathodic contribution deduced impedance spectra show two near distinct loops which are not complete semicircle. Considering that the major contribution to the cell impedance is anodic resistance, and two non semicircular curves, an equivalent circuit with two (RQ) elements could best fit the impedance spectra. Counting a pure resistive impedance for R_{bulk}, and an inductive element for the collector lead, the suggested equivalent circuit can have all these elements in series in the form of $[LR_{bulk}(R_1Q_1)(R_2Q_2)]$. Figure 5.9 shows this equivalent circuit.

It was already mentioned in chapter 3 that cathodic contribution to the impedance can be model with an equivalent circuit in the form of $[LR(C[R(RQ)])]$. A code was developed to fit the anodic impedance to the suggested equivalent circuit after deducing the contribution of the cathodic impedance. The fits for the MEA 12 data

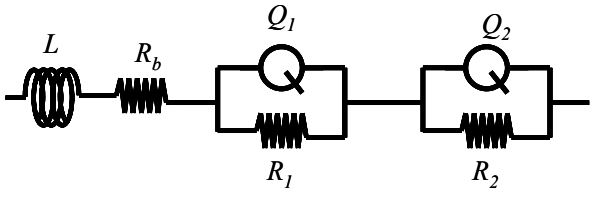

Figure 5.9 – The equivalent circuit which models the anodic impedance for CO electrochemistry

showed that the suggested equivalent circuit can fit both dry and wet CO streams and also were able to capture the effect of applying overpotential to the cell within a very reasonable error margin (χ^2 in the order of 10^{-5}). Figure 5.10a shows experimental results and fits for the 100 µm pattern impedance at T = 725 °C and V_{OCV}. Figure 5.10b shows the same setup with η_{tot} rising from 0 mV (OCV conditions) to 100 mV.

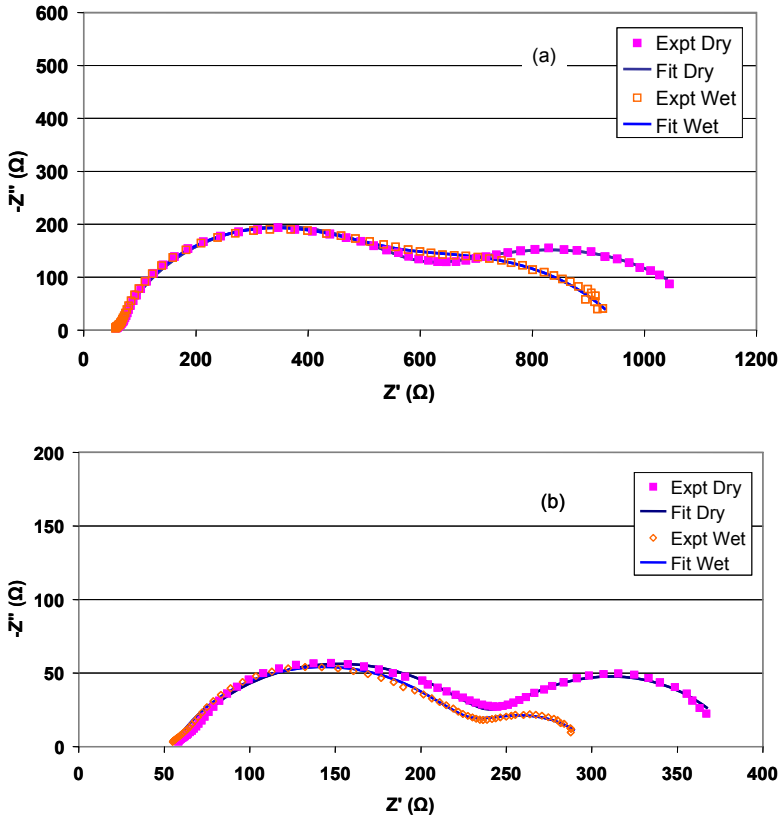

Figure 5.10 – Anodic impedance spectra for the 100 µm pattern at 725 °C; dry fuel feed: p_{CO} = 0.323, p_{CO2} = 0.032; wet fuel feed: p_{CO} = 0.315, p_{CO2} = 0.032, p_{H2O} = ~0.025; a) V_{OCV}; b) 100 mV overpotential.

Figure 5.11 shows the Bode plot for the 100 µm pattern at T = 725 °C for dry CO/CO_2 at η_{tot} = 100 mV. The plots show two arcs with two distinct relaxation frequencies: ω^*_{Hi} around 300 Hz and ω^*_{Low} around 0.6 Hz. ω^*_{Hi} is associated with

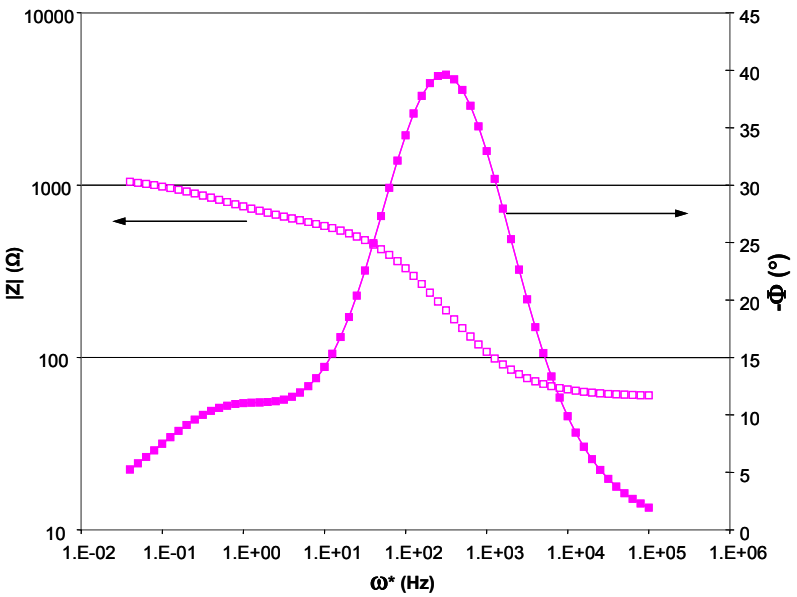

Figure 5.11 – Total impedance and impedance phase vs. frequency for a 100 μm Group B pattern at 725 °C with η_{tot} = 100 mV; with p_{CO} = 0.323, p_{CO2} = 0.032

Some facts can be noticed from the impedance fit data. *e* plays a big role in reduction of the impedances, yet introducing 2.5% H_2O into the CO/CO_2 fuel stream caused a major reduction in nearly all impedances including R_{bulk}. A drop of 3% to 8% of the R_{bulk} can be seen between dry and wet cases at the same *T*. The other observation could be the rapid increase in ω^*_{Hi} with increasing the η_{tot} which clearly shows that the first loop seen in the impedance spectra refers to the charge transfer process. The ω^*_{Low}, on the other hand, is less effected by temperature change but at each given temperature humidity almost doubles the low relaxation frequency. The with humidity dependency of the $\omega^*_{\mathrm{Low,}}$ A second loop in the impedance spectra is likely related to surface diffusion of the adsorbed species. The last fact that can be noticed is the zero value for fitted inductance, *L*, in all cases. The reason of that is that

Table 5.6 – The fit parameters of fitting the impedance data of MEA 12 onto the equivalent circuit in Figure 5.9.

T (°C)	η_{ot} (mV)	P_{H2O}	R_{bulk} (Ω)	L_1 (μH*c m^2)	R_1 (Ω)	Y_1*100 (S*s^{n1}* cm^2)	n_1	ω_1* (Hz)	R_2 (Ω)	Y_2*100 (S*s^{n1}* cm^2)	n_2	ω_2* (Hz)
700	0	0	75.53	0	830.43	0.0017	0.649	35.98	950.42	0.0806	0.760	0.295
		0.023	69.13	0	611.20	0.0015	0.811	50.83	878.27	0.0004	0.536	1.382
	100	0	75.05	0	285.66	0.0030	0.698	143.26	162.40	0.0044	0.779	0.241
		0.023	70.91	0	236.62	0.0027	0.717	185.08	91.50	0.0086	0.588	0.242
	200	0	73.25	0	150.60	0.0066	0.618	279.52	23.57	0.0168	0.816	0.496
		0.023	68.48	0	124.98	0.0061	0.629	374.80	31.19	0.0316	0.901	0.162
	300	0	73.44	0	109.65	0.0088	0.598	366.86	18.61	0.0886	0.966	0.094
		0.023	67.35	0	89.86	0.0001	0.575	498.95	16.80	0.0600	1.000	0.158
725	0	0	59.27	0	508.18	0.0018	0.770	68.41	581.04	0.0011	0.584	0.322
		0.023	57.03	0	423.03	0.0017	0.799	78.38	486.86	0.0005	0.574	1.717
	100	0	57.89	0	183.31	0.0036	0.691	223.85	145.92	0.0046	0.718	0.278
		0.023	54.97	0	171.31	0.0033	0.706	245.89	74.46	0.0074	0.613	0.424
	200	0	68.48	0	124.98	0.0061	0.629	374.80	31.19	0.0316	0.901	0.162
		0.023	53.66	0	91.63	0.0073	0.620	512.88	34.22	0.0206	0.824	0.244
	300	0	67.34	0	89.86	0.0001	0.575	498.95	16.80	0.0600	1.000	0.158
		0.023	51.74	0	67.34	0.0002	0.547	636.33	19.18	0.0276	0.936	0.314
750	0	0	47.61	0	389.39	0.0027	0.733	79.88	524.65	0.0016	0.648	0.219
		0.023	45.56	0	281.96	0.0019	0.796	111.72	345.88	0.0007	0.550	2.037
	100	0	45.66	0	137.07	0.0070	0.630	255.77	102.17	0.0051	0.800	0.362
		0.023	44.41	0	120.40	0.0045	0.683	332.16	52.59	0.0112	0.647	0.360
	200	0	44.70	0	91.29	0.0002	0.536	316.03	14.56	0.0186	0.951	0.627
		0.023	42.54	0	68.68	0.0001	0.583	617.05	21.20	0.0273	0.898	0.293
	300	0	45.30	0	54.62	0.0001	0.612	589.31	196.32	0.0532	0.191	0
		0.023	41.81	0	50.22	0.0002	0.532	824.24	10.69	0.0463	1.000	0.321
775	0	0	36.04	0	235.74	0.0045	0.691	113.98	489.95	0.0019	0.707	0.180
		0.023	36.43	0	228.64	0.0031	0.739	128.03	287.95	0.0009	0.654	1.177
	100	0	32.76	0	94.01	0.0003	0.485	209.15	39.08	0.0056	1.000	0.729
		0.023	34.74	0	88.28	0.0076	0.643	382.17	49.58	0.0116	0.686	0.358
	200	0	35.17	0	66.30	0.0003	0.530	283.04	5.60	0.0466	1.000	0.609
		0.023	33.01	0	53.65	0.0003	0.512	540.72	8.88	0.0417	1.000	0.430
	300	0	35.43	0	46.74	0.0002	0.554	661.83	79.82	2.4648	0.420	00
		0.023	33.01	0	36.26	0.0003	0.528	946.47	304.56	0.2470	0.168	00

inductance effects in series and it has already been shown in the cathodic equivalent circuit of [$LR_1(C[R_2(R_3Q)])$].

5.5. Discussion and Analysis

The results of the current study provide a strong indication that adsorption/ desorption equilibration may play a decisive role in the oxidation of CO. It is important to explore this hypothesis further by building numerical models (as in chapter 6) to predict impedance spectra and polarization curves using multi-step chemistry for CO electrochemical oxidation on Ni/YSZ anodes. While quantitative mechanisms for such multi-step processes are not fully resolved, the kinetic richness of electrochemical measurements, and in particular AC impedance spectra, provides a basis for estimating rates of adsorption/desorption and charge transfer processes that may control the electrochemical oxidation of the fuels.

5.5.1. Effect of Applied Overpotential

In this section the effect of the overpotential on CO electrochemical oxidation is discussed. Unlike the H_2 electrochemical oxidation results presented by others [67], the polarization resistance for CO electrochemical reaction does not linearly vary with the overpotential in logarithmic scale. The polarization resistances of the 100 μm pattern under wet and dry diluted CO/CO_2 mixture at 4 different T in Figure 5.12 shows a sharp drop after applying overpotential of 100 mV vs. V_{OCV} condition. This steep drop gets shallower with applying more overpotential. This suggests that

processes other than charge transfer play major role in CO electrochemical oxidation. This holds for both impedances in Nyquist plot; here are named as charge transfer resistance, R_{CT}, and diffusion resistance, R_{diff}. Figure 5.13 shows R_P, R_{CT} and R_{diff} plotted vs. overpotential at 700 °C and dry fed CO/CO_2 fed fuel from the fitted data.

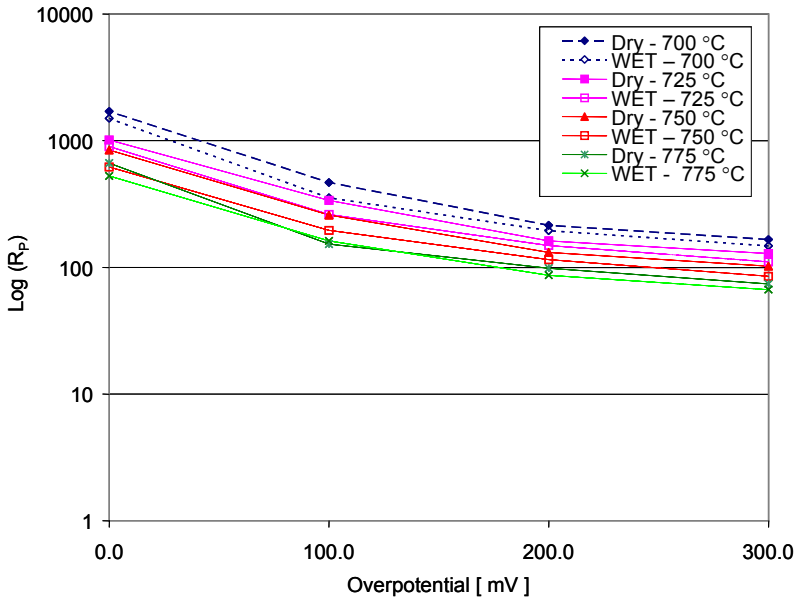

Figure 5.12 – Polarization resistance vs. applied cell overpotential for the range of T from 700 to 775 °C; dry fuel feed: $p_{CO} = 0.323$, $p_{CO2} = 0.032$; wet fuel feed: $p_{CO} = 0.315$, $p_{CO2} = 0.032$, $p_{H2O} = \sim 0.025$

5.5.2. Effect of Temperature and Humidity

Figure 5.14a shows the effect of the temperature on the mean current passing through the cell at the range of η_a from 100 mV to 300 mV on a 10 µm pattern under 33.3% fuel CO/CO_2 diluted in Ar. The fuel is applied in dry and wet ($p_{H2O} = \sim 0.025$) cases. The graph is in logarithmic scale and the slope of the lines give the E_{act} for the mean current which are listed in Table 5.7. Figure 5.14b shows dependency of the

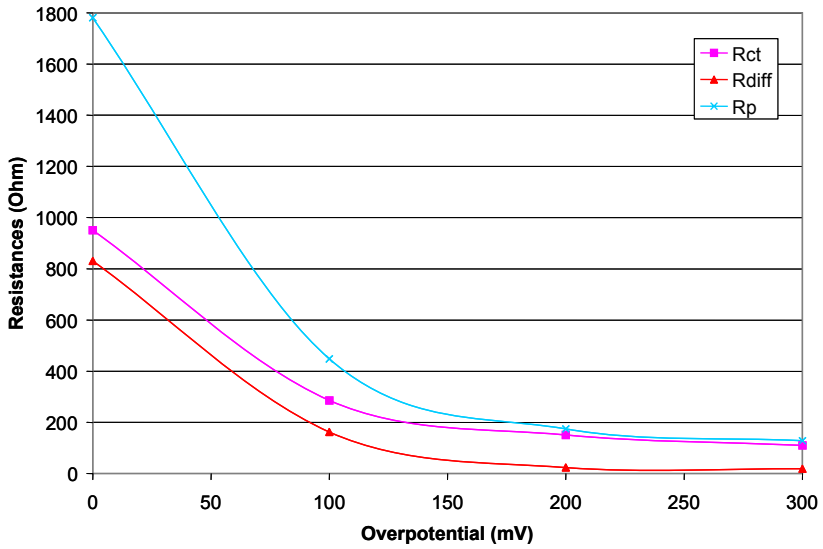

Figure 5.13 – Polarization, charge transfer and diffusion resistances vs. η_{tot} for T = 700 °C; dry fuel feed: p_{CO} = 0.323, p_{CO2} = 0.032

polarization resistance to the temperature change under wet can dry fuel fed condition for the same pattern under the same working condition. The activation energies calculated from these graphs are listed in the Table 5.7.

5.5.3. Effect of Electrode Geometry

To address the effect of geometry, specifically l_{TPB}, in this section mostly results from MEAs 2 and 5 will be discussed. At MEA 2 was also pattern group B was sputtered. Cell operating condition is listed in Table 5.2. The experiments were conducted at V_{OCV} and 100 mV overpotential. Thin sputtered patterns discussed in chapter 4 did not provide any insight about the scaling of the impedances with the l_{TPB} due to agglomeration of the patterns, yet it was examined by several other researchers [4, 66, 84] for H_2 fuel and was proven. In other word for different patterns with the equal l_{TPB} the R_{CT} should remain constant. The group B patterns were designed such

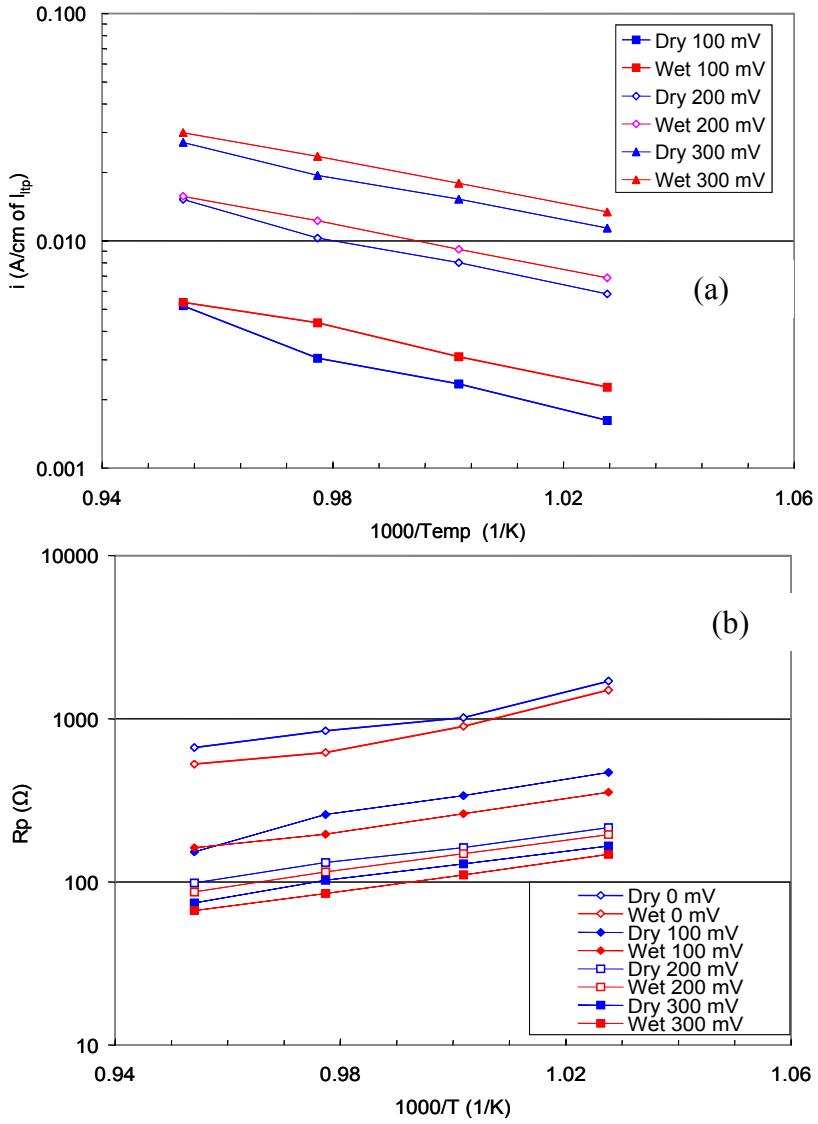

Figure 5.14 – Electrochemical performance 100 µm pattern for the range of T = 700 to 775 °C for dry fuel feed: p_{CO} = 0.323, p_{CO2} = 0.032; and wet fuel feed: p_{CO} = 0.315; p_{CO2} = 0.032; p_{H2O} = ~0.025. a) i at the applied η_{tot}; b) $R_{pol,a}$ for applied η_{tot}.

that all patterns have near constant l_{TPB} and a_{elec}, while a_{cat} was different for each pattern. Figure 5.15 shows that unlike H_2, charge transfer resistance in CO electrochemical oxidation does not scale precisely with l_{TPB}. This suggests that some other processes also play role in CO electrochemical reaction on the Ni surface.

Table 5.7 – Summary of activation energy curves plotting mean i and $R_{pol,a}$ vs T for 100 µm patterns for dry fuel feed: $p_{CO} = 0.323$, $p_{CO2} = 0.032$ and wet fuel feed: $p_{CO} = 0.315$, $p_{CO2} = 0.032$, $p_{H2O} = \sim 0.025$

p_k (kPa)	η_{tot} (mV)	E_{act} for R_P (eV)	E_{act} for i *100 (eV)
$p_{CO} = 32.2$ $p_{CO2} = 3.2$	0	1.06	N/A
	100	1.27	-0.40
	200	0.90	-1.06
	300	0.93	-1.80
$p_{CO} = 32.2$ $p_{CO2} = 3.2$ $p_{H2O} = 0.025$	0	1.24	N/A
	100	0.93	-0.37
	200	0.94	-1.04
	300	0.93	-1.93

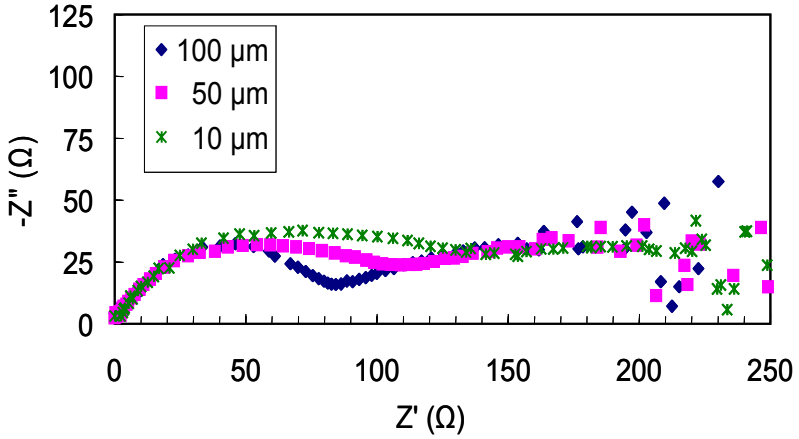

Figure 5.15 – Corrected impedance for R_{bulk} at $T = 700$ °C for three different patterns 10 µm, 50 µm and 100 µm wide lines for $\eta_{tot} = 100$ mV overpotential with $p_{CO} = 0.267$, $p_{CO2} = 0.067$.

Since the electrochemical performance does not scale exactly with $l_{TPB,}$ this suggests that processes related to adsorption, surface diffusion, and desorption may be limiting surface transport of reactants (likely CO_{Ni} which is expected to be slow at diffusion) to the TPB. To investigate dependencies on a_{cat}, another set of experiments was completed on Group B patterns. This experiment is done on MEA 0

at conditions detailed in Table 5.2. Figure 5.16 shows the impedance curves for the patterns in group B with varying a_{cat} while l_{TPB} is constant. These impedance data have R_{bulk} removed but not R_{cat} which is small and fixed for each pattern since a_{elec} is the same for the four patterns.

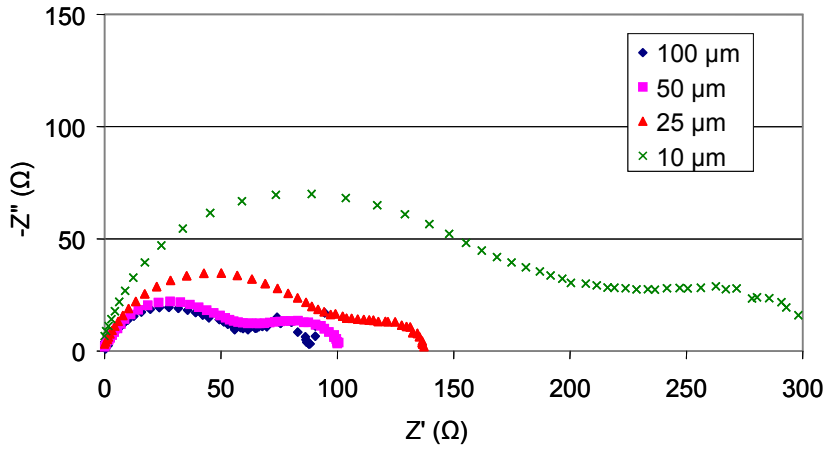

Figure 5.16 – Impedance spectra of four different pattern widths diluted dry CO (p_{CO} = 0.33) at V_{OCV} for different width of patterns in group B at T = 750 °C.

The impedance is scaling neither with the l_{TPB} nor the a_{cat}. The quite similar shape of the two arcs in the impedance spectra shows some scaling. The same scaling behavior was also observed in MEA 5. This scaling for the MEA 0 experiments is quantified in Table 5.8 and compared with the variation in a_{cat} of the different patterns. These results suggest that as a_{cat} increases a larger fraction of the surface is available to provide adsorbed CO to the TPB. More data on the effect of pattern geometry on CO electrochemical reaction are presented from MEA 5 results at T = 700, 725 and 750 °C and CO/CO_2 combination (p_{CO} = 0.267; p_{CO2} = 0.067). The experiments were conducted at OCV and 200 mV overpotential.

Table 5.8 – Scaled impedance and geometrical scale of the Ni patterned in group B of Table 2.2 being exposed to CO/Ar fuel at $T = 750$ °C for two different experiments.

Pattern width (µm)	Geometrical scaled a_{cat}/ a_{cat} of 10 µm	Observed scaling a_{cat} / a_{cat} of 10 µm MEA 0	Observed scaling a_{cat} / a_{cat} of 10 µm MEA 5
10	1.0	1.0	1.0
25	2.5	2.0	1.3
50	5.0	3.1	1.6
100	10.0	3.5	1.65

Figure 5.17 shows that at V_{OCV}, $R_{pol,a}$ varies with a_{cat}. Considering the fact that in MEA 5 the l_{TPB} is equal for all patterns and only a_{cat} is varying there is a dependency between the $R_{pol,a}$ and the a_{cat}. Applying overpotential to the patterns causes the $R_{pol,a}$ to vary substantially less a_{cat}. Comparing these results with the above shown impedance spectra at V_{OCV} and $\eta_{tot} = 100$ mV suggests that with increasing $\eta_{tot} \geq 200$ mV, CO electrochemical oxidation rates begins to depend more linearly with l_{TPB}.

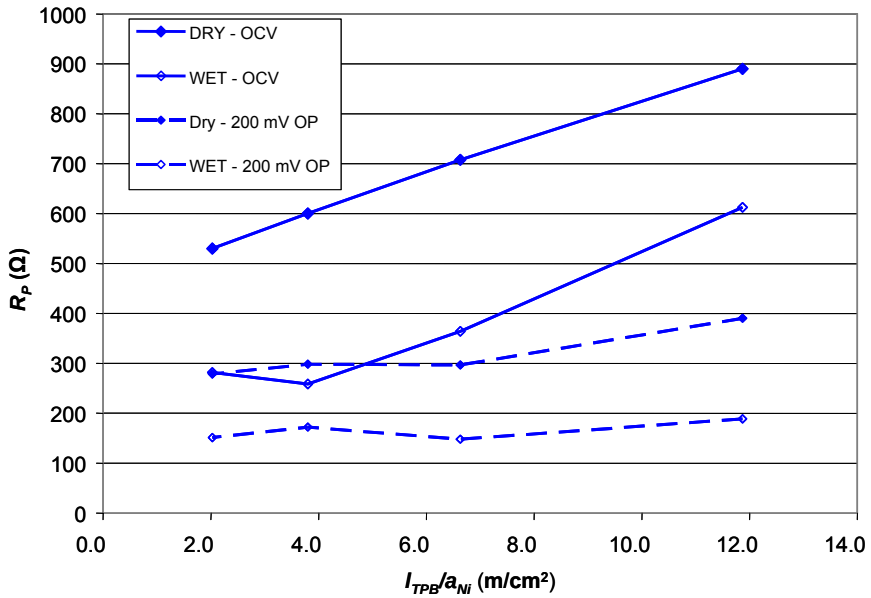

Figure 5.17 – $R_{pol,a}$ for 25 µm pattern at 700 °C, V_{OCV} and $\eta_{tot} = 200$ mV; dry: $p_{CO} = 0.267$, $p_{CO2} = 0.066$; wet: $p_{CO} = 0.260$, $p_{CO2} = 0.065$, $p_{H2O} = 0.025$

5.5.4. Effect of CO_2 Concentration

Like concentration water while using H_2 as fuel, concentration of CO_2 plays a role while using CO as fuel. Concentration of CO_2 will lead to the slower or faster equilibrium in equations involving dissociative adsorption/desorption as well as affecting the site fraction of species and their surface converges. To study the effect of CO_2 concentration MEA 13 has been exposed to a different of CO_2 concentration ranging from p_{CO2} = 0.0017 to 0.0833 at constant T. Figure 5.18 shows the changes in current density while p_{CO2} is varying.

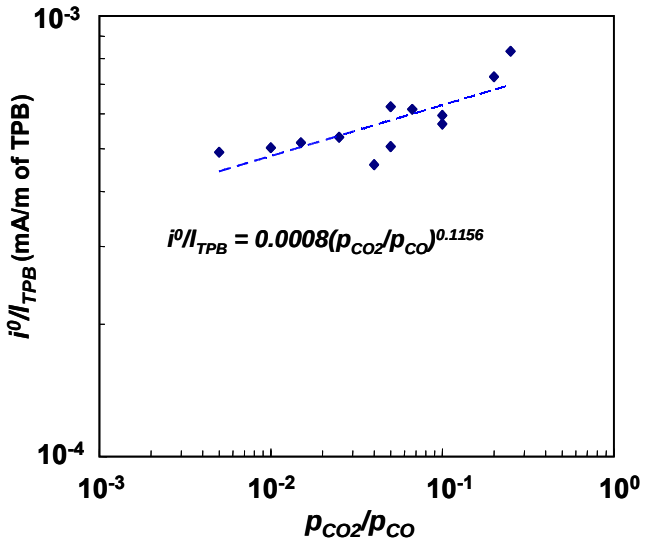

Figure 5.18 – i^o variation vs. p_{CO2}/p_{CO} in the range of 0.005 to 0.5at T = 775 °C.

If p_{CO} is constant in the MEA 13 experiments, the i^0 equation can be written in terms of the p_k of the reactants and products as suggested here:

$$\frac{i^0}{l_{tpb}} = k\left(\frac{p_{CO2}}{p_{CO}}\right)^n \qquad \text{(Eq. 5.1)}$$

where n will be the related to β_f the same way that Mizusaki et al. [4] have driven this value for H_2 reaction. Figure 5.19 shows two cases done on MEA 13 under constant p_{CO} dry case (no humidity is introduced) and constant p_{H2O} (p_{CO} is varying).

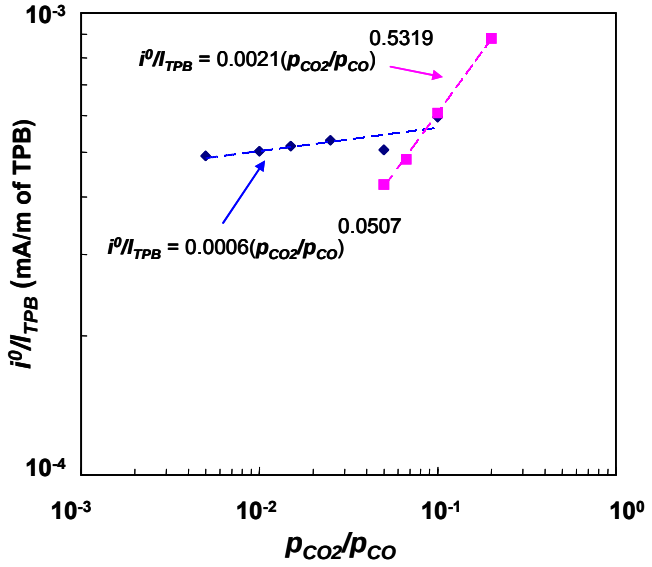

Figure 5.19 – i^o variation with change in p_{CO2}/p_{CO} in two cases of constant p_{H2O} = 0.03 and constant p_{CO} = 0.32 at T = 775 °C.

β_f for the dry feed does not match the β_f value achieved earlier from the fitting the data to Butler-Volmer equation. The reason could be due to the inaccuracy of the mass flow controllers at the very low partial pressures that caused inaccurate assessment of p_k.

5.6. Suggested CO Electrochemical Reaction on the Ni Surface

Figure 5.20 shows the dependency of the $R_{pol,a}$ to a_{cat} (proportional to pattern line widths) for different T and V_{OCV}. For wet CO feeds at 700 °C, area specific $R_{pol,a}$ increases with smaller pattern widths to a point at which it flattens out with increasing pattern width. This dependency with pattern line width reduces with increasing T to 725 °C and almost fades away with increasing the temperature to 750 °C.

This suggests that unlike H_2, range of working temperatures contribute in domination of the rate determining step process in CO electrochemical oxidation. At open circuit, when temperature is high, charge transfer is the only rate determining step since there is since as long as the l_{TPB} remains the R_{pol} remains constant. While in lower temperature other resistances (such as adsorption/desorption, or surface diffusion) which are area related compete as of rate limiting step.

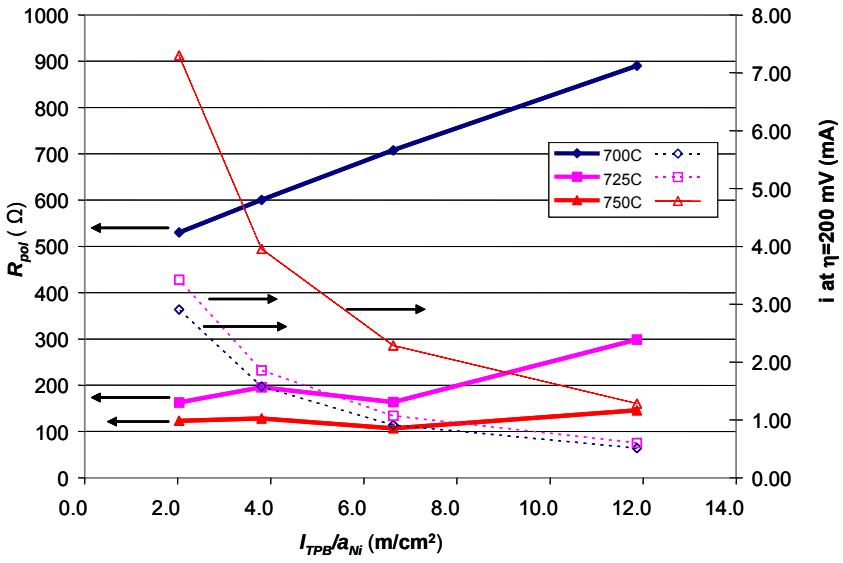

Figure 5.20 – Group B pattern at V_{OCV} and different T; Fuel: p_{CO} = 0.260, p_{CO2} = 0.065, p_{H2O} = 0.025; left axis: R_{pol}; right axis: Cell current at η_{tot} =200 mV

The other discussion in term of the describing the CO electrochemistry at the Ni surface is related to the relaxation frequencies. The impedance fit results for the MEA 12 are listed in the Table 5.6. Plotting the calculated high relaxation frequencies versus cell overpotential for different temperature shows that at applied η_{tot} = 300 mV the ω_{Hi} increases approximately 7-8X for the dry and wet cases respectively. Figures 5.21a and 5.21b show this trend. Interestingly there is a 30% increase in ω_{Hi} at each given temperature and overpotential between dry and wet case. In other word in presents of small amount of H_2O charge transfer reaction occurs faster. This could be due to the process of the water-gas-shift on the Ni surface.

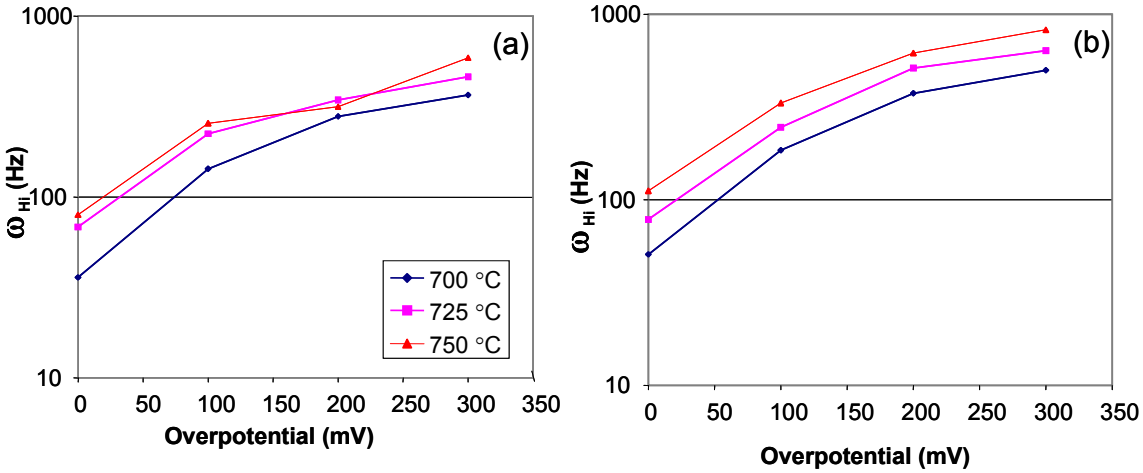

Figure 5.21 – High relaxation frequencies as a function of cell overpotential at different *T* calculated from the fitting parameters from MEA 12 data; a) p_{CO} = 0.267, p_{CO2} = 0.067, b) p_{CO} = 0.260, p_{CO2} = 0.065, p_{H2O} = 0.025.

Looking at the low relaxation frequencies on the other hand reveals that the second process is less affected by overpotential than in humidity. Figure 5.22a shows an almost constant ω_{Low} at all *T*'s and η_{cell}'s for the dry CO/CO_2 fuel. In the wet fuel

stream there are approximately 5 times bigger values for the OCV which can be due to the produced H_2 in water-gas-shift reaction. This higher ω_{Low} drops to almost the same values as of dry case with applying overpotential and stays almost constant again. Being almost independent from the applied overpotential suggest that this process is a non-electrochemical reaction and most likely surface diffusion since the adsorption/desorption rate could be affected by the cell voltage and species consumption and production.

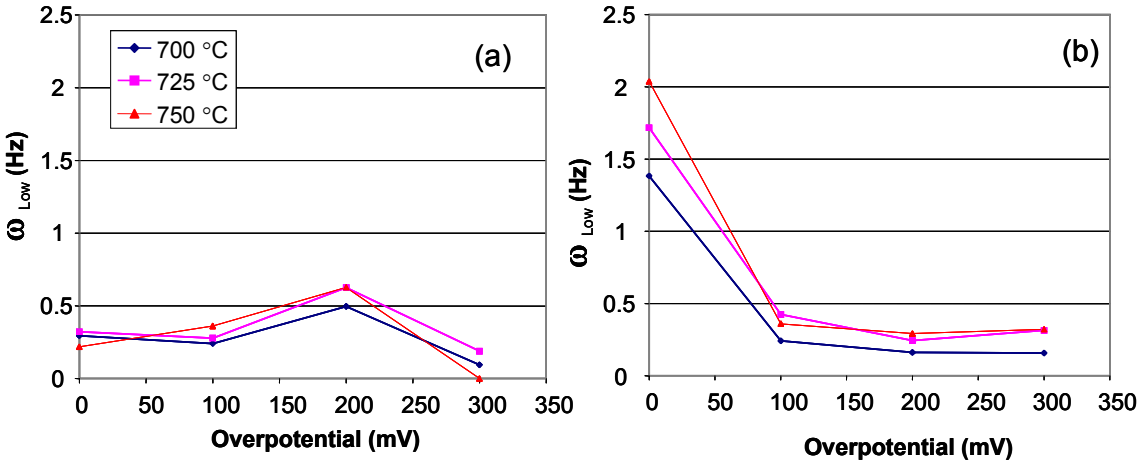

Figure 5.22 – Low relaxation frequencies as a function of cell overpotential at different T calculated from the fitting parameters from MEA 12 data; a) $p_{CO} = 0.267$, $p_{CO2} = 0.067$, b) $p_{CO} = 0.260$, $p_{CO2} = 0.065$, $p_{H2O} = 0.025$.

Figures 5.23 shows possible pathways of CO/CO_2 electrochemical oxidation on the Ni surface of SOFC without and with presence of humidity. All the result discussed above show a complex CO electrochemistry on the Ni anode. A mechanism that extracts the important processes illustrated in Figure 5.23 will be presented in chapter 6. Quantifying critical potential rate-limiting processes in that

mechanism will allow for a numerical patterned anode model (discussed in chapter 6) to be used to explore which process dictate electrochemical oxidation of CO for a variety of conditions on Ni/YSZ anodes.

To summarize the result of this chapter on CO electrochemical oxidation on Ni anode of SOFC's, the following considerations can be listed:

- CO electrochemical oxidation is slower than H_2 electrochemical oxidation

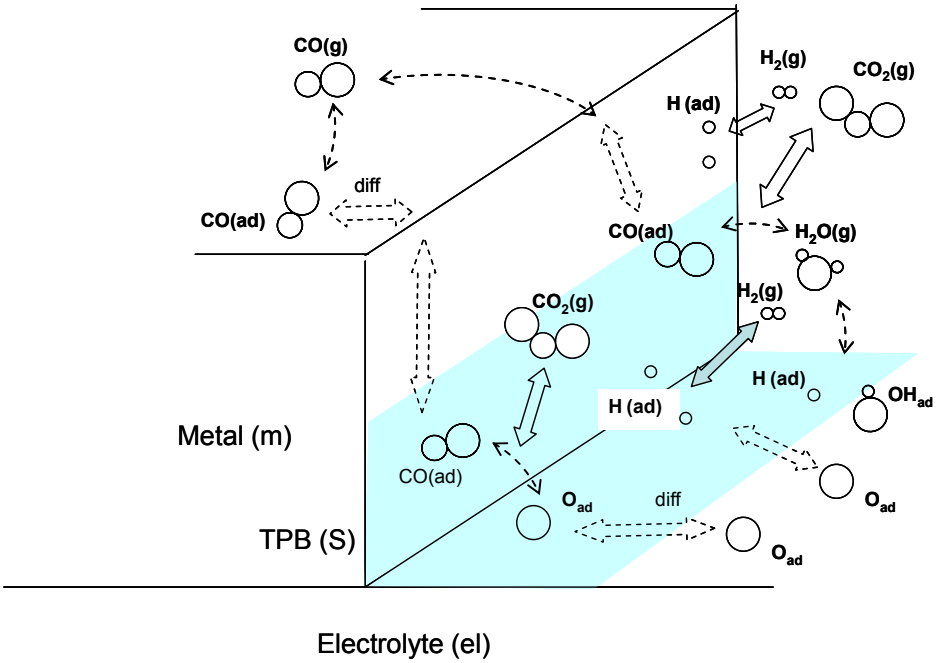

Figure 5.23 – Schematic drawing of TPB vicinity showing the possible CO electrochemical reaction; with and without presence of water

- Impedance data and curve fits reveal two distinct controlling processes in CO oxidation; one associated with charge transfer and the other involving adsorption/desorption and/or surface diffusion
- Addition of small amounts of H_2O to CO anode feeds enhances the charge transfer processes but has little effect on the other (physical) processes

6. Modeling Three Phase Boundary Processes

Many recent SOFC simulation studies assume that in conventional Ni/YSZ porous SOFC anodes, gaseous CO is converted to H_2 through water-gas-shift reaction and all charge transfer electrochemical reactions in the anode involve H_2 as the fuel source. The validity of this assumption is called into question when considering the relative electrochemical performance in past studies of CO vs. H_2 oxidation in porous Ni/YSZ anodes. In these past studies, the activation overpotentials $\eta_{act,an}$ of the anode charge transfer processes were clouded by the complex porous media transport in the thick porous anode. Since the pattern anode MEA's eliminate the porous media transport processes and concentration gradients in the gas phase, it is useful to model the patterned anode geometries with their well-defined l_{TPB} and compare model predictions with possible surface chemistry mechanisms to assess $\eta_{act,an}$ as a function of fuel composition and operating conditions. A patterned anode model was developed in this study as explained in this chapter to evaluate a proposed mechanism for CO electrochemical oxidation on Ni/YSZ anodes and to attempt to explain the role of H_2O in accelerating the CO oxidation reactions on the Ni/YSZ surfaces.

In this regard, Figure 5.23 provided an illustration of some of the reaction and diffusion processes in CO electrochemical oxidation that occur near the TPB. Any number of these processes may play a critical role in governing the rate of the oxidation process. Figure 5.23 also illustrates the current understanding of the H_2 electrochemical oxidation mechanisms in Ni/YSZ anodes as discussed earlier in chapters 1 and 4. However, Figure 5.23 does not show how the CO and H2 oxidation

processes may be coupled through heterogeneous reactions on the Ni metal surface. This modeling effort wanted to provide a preliminary exploration into trying to unravel the uncertain nature of CO electrochemistry on Ni metal and also to assess how it is impacted by the heterogeneous surface reactions derived from the presence of H_2O.

The experimental results discussed in chapter 5 led to proposed mechanism (presented later in this chapter) for the electrochemical CO oxidation in Ni/YSZ anodes. To investigate the importance of different reaction steps, a numerical model of the patterned anodes with detailed kinetics and surface transport has been developed to compare experimental results (particularly on CO oxidation in chapter 5) with model predictions (as a function of critical reaction rate and surface diffusion parameters). The numerical model involves integrating the governing non-linear differential equations (presented below) of the patterned anodes with respect to time to find steady-state voltages and surface site fractions to predict the η_{anode} vs. current per length of three-phase boundary. Linearization of the model about the steady-state solutions allows for rapid calculation of impedance spectra as presented below.

The numerical model of the patterned anode allows for investigation of how the steady state and frequency-dependent response to an excitation input is influenced by various physical, chemical, and thermodynamic parameters. Parameters such as E_{act} to charge transfer, heats of adsorption, sticking coefficients, and charge transfer coefficients can be manipulated to assess their impact upon the predicted patterned anode performance.

At the TPB interface, fuel molecules (CO and H_2) are oxidized by the O^{2-} ions from the electrolyte surface to generate products (CO_2 and H_2O). The kinetics of these processes can be studied experimentally by electrochemical impedance spectroscopy (EIS) [96] and voltammetry. Interpretation of EIS data with equivalent circuit fitting is useful for observing trends, but it does not allow for clear physical and chemical interpretation of the equivalent circuit elements and, thus, for identifying kinetic or transport rate parameters necessary for modeling the overall oxidation process. Some researchers have begun to relate EIS measurements to detailed kinetic models but to date all of these studies have been only for H_2 electrochemical oxidation [68, 69, 114]. This work will build on that past work by developing a patterned anode model and use it here for analyzing the CO electrochemical oxidation processes, both in dry and wet conditions.

6.1. Model Development (State Space Model)

The governing equation for surface coverage of species as a function of time on an electrode or electrolyte surface both away and near the TPB can be written in the general form of equations 6.1-a and 6.1-b respectively.

$$\frac{\partial\left(\Gamma_{surf}\theta_{k,surf}\right)}{\partial t} = W_k\left(\dot{s}_{k,surf}\right) - \frac{l_{tpb}}{a_{surf}}\frac{D_{k,surf}}{\delta_{surf}}\Gamma_{surf}\left(\theta_{k,surf} - \theta_{k,tpb}\right) \qquad \text{(Eq. 6.1-a)}$$

$$\frac{\partial\left(\Gamma_{surf}\theta_{k,tpb}\right)}{\partial t} = W_k\left(\dot{s}_{k,surf} + \frac{l_{tpb}}{a_{surf}}\dot{s}_{k,tpb}\right) + \frac{l_{tpb}}{a_{surf}}\frac{D_{k,surf}}{\delta_{surf}}\Gamma_{surf}\left(\theta_{k,surf} - \theta_{k,tpb}\right) \qquad \text{(Eq. 6.1-b)}$$

$\dot{s}_{k,surf}$ refers to non-charge transfer reactions that occur on only one surface both near and away from the TPB, and $\dot{s}_{k,tpb}$ refers to charge transfer reactions which occur across the TPB and are strong functions of activation overpotential $\eta_{act,an}$. The surface coverage equations and voltage equations, along with the rate of the current generated at the TPB are the state equations and can be shown in the mathematical form of:

$$\dot{\theta}_k(\theta,i,t) = f(\theta_k,i,t) \qquad \text{(Eq. 6.2)}$$
$$\eta(i,t) = g(\theta,i)$$

The state-space model can be used to transfer these state equations from the time domain to frequency domain by an infinitesimal oscillation around the steady state surface coverage. The coverage equation can be considered linear around this oscillation region and the equation 6.2 can be linearized around the steady state point $\dot{\theta}(0,\eta) = \dot{\theta}^*(\eta)$ to get the equations 6.3.

$$\delta\dot{\theta}(t,p) = A(p)\delta\theta(t,p) + B(p)\delta i(t) \qquad \text{(Eq. 6.3)}$$
$$\delta\eta(t,p) = C(p)\delta\theta(t,p) + D(p)\delta i(t) + i$$

By means of Laplace transform the linearized equations can be shifted from the time domain into the frequency domain to generate the transfer functions as in equations sets of 6.4.

$$\eta(s,p) = Y(s,p)i(s) \qquad \text{(Eq. 6.4)}$$
$$Z(s) = C(s\text{I-}A)^{-1}B + D$$

In which the matrices A, B, C, and D are:

$$A = \left.\frac{\partial f}{\partial \theta}\right|^{*} \qquad B = \left.\frac{\partial f}{\partial i}\right|^{*}$$

$$C = \left.\frac{\partial g}{\partial \theta}\right|^{*} \qquad D = \left.\frac{\partial g}{\partial i}\right|^{*}$$

A MATLAB-based code has been developed for the stepwise model previously explained. As it can be seen from the flowchart in Figure 1.5 this code involves in taking some preliminary suggested electrochemical reaction steps and the initial guessed values as input. This code uses the open source chemical/electrochemical solver code, CANTERA, to calculate the chemistry of the surfaces including coverage, rate of production of species, reaction constant and stoichiometric values. In the following section an overlook of the state space model is explained.

6.1.1. Model Governing Equations

To avoid tailor making the model for each new suggested sets of stepwise electrochemical reaction, the generalized form of the reaction are being used. The boundary conditions at the electrode surface will depend upon the chemical reactions occurring at the surface. For a given reaction, there will be K_g gas-phase species and K_s surface species participating as reactants and/or products. These reactions can be written in form of:

$$\sum_{k=1}^{K_s} \nu_{ki,f} R_{k,s} + \sum_{k=1}^{K_g} \nu_{ki,f} R_{k,g} \Leftrightarrow \sum_{k=1}^{K_s} \nu_{ki,r} R_{k,s} + \sum_{k=1}^{K_g} \nu_{ki,r} R_{k,g} \qquad \text{(Eq. 6.5)}$$

where ν_{ki} is the stoichiometric coefficient for a given surface species $R_{k,s}$ or gas-phase species $R_{k,g.}$ The rate of formation ω_k in moles/cm^2 of catalyst/sec for a given surface species $R_{k,s}$ is given by the following equations.

$$\omega_{ki} = \left(\nu_{ki,f} - \nu_{ki,r}\right)\left(k_{i,f} \prod_{k=1}^{K_s}\left(\frac{\theta_k \Gamma}{\sigma_k}\right)^{\nu_{ki,f}} \prod_{k=1}^{K_g}\left(\frac{P\overline{W}Y_k}{W_k RT}\right)^{\nu_{ki,f}} - k_{i,r} \prod_{k=1}^{K_s}\left(\frac{\theta_k \Gamma}{\sigma_k}\right)^{\nu_{ki,r}} \prod_{k=1}^{K_g}\left(\frac{P\overline{W}Y_k}{W_k RT}\right)^{\nu_{ki,r}} \right)$$

$$\omega_k = \sum_{i=1}^{I} \omega_{ki} \qquad \text{(Eq. 6.6)}$$

where $k_{i,f}$ and $k_{i,r}$ are the forward and reverse rate constants (units depending on number of reactants) of the i^{th} reaction, θ_k is the fraction of surface sites occupied by species k, Γ is the surface site density (mol/cm^2) and σ_k sites occupied by a single k molecule. P and T are gas phase pressure and temperature, W_k the molecular weight of species k, and R is the universal gas constant. In some applications Γ can change due to high temperature sintering, i.e., reconfiguring of the catalyst surface, but these effects will be ignored in this discussion.

$$k_{i,f} = A_{i,f} T^{\beta_{i,f}} \exp\left(\frac{-E_{i,f}}{RT}\right) \qquad k_{i,r} = A_{i,r} T^{\beta_{i,r}} \exp\left(\frac{-E_{i,r}}{RT}\right) \qquad \text{(Eq. 6.7)}$$

$k_{i,r}$ and $k_{i,f}$ and thus $E_{i,f}$ and $E_{i,r}$ can be related via the equilibrium constant when appropriate. $A_{i,f}$, $\beta_{i,f}$, and $E_{i,f}$ are the forward pre-exponential, temperature exponent, and activation energy respectively.

For adsorption reactions and other reactions between surface-adsorbed species, the activation energies may be surface coverage (i.e., θ_k) dependent. In that case, we

must multiply the above expressions by a term related to the surface coverage effects. In some cases, it may be more convenient to express the adsorption reaction rate in terms of sticking coefficient. The following equation is used for the forward reaction rate constant in the adsorption reactions.

$$k_{i,f} = \frac{\sigma_i}{1-\sigma_i/2}\ \gamma_i^{-m}\sqrt{\frac{RT}{2\pi W_k}} \qquad \text{(Eq. 6.8)}$$

in which, γ_i is the sticking coefficient and m is the sum of the number of sites needed for adsorption.

For reversible reactions, Cantera utilizes user-specified forward reaction rate coefficients and thermodynamics to calculate the reverse reaction rate coefficients, as described by Goodwin [69]

$$\frac{k_{i,f}}{k_{i,r}} = \exp\left(-\frac{\Delta G^o_{rxn,i}}{\overline{R}T}\right)\ \prod_{k=1}^{nsp_g}\left(\frac{P\overline{W}Y_k}{W_k RT}\right)^{-\nu^*_{ki}} \qquad \text{(Eq. 6.9)}$$

where $\overline{R}$ is the universal gas constant, $\Delta G^o_{rxn,i}$ is the reference change in Gibbs free energy and ν^*_{ki} is the net stoichiometric coefficient of species k for reaction i.

Reaction rates for all charge-transfer reactions are described by Butler-Volmer kinetics. As described by Bessler et al.[106] these expressions obey mass-action kinetics, with

$$k_{f,CT} = k^*_f \exp\left(\frac{\alpha_f n_{elec} F\ \Delta\Phi}{\overline{R}T}\right) \qquad \text{(Eq. 6.10)}$$

$$k_{r,CT} = k_r^* \exp\left(\frac{-\alpha_r n_{elec} F \ \Delta\Phi}{\overline{R}\, T}\right) \qquad \text{(Eq. 6.11)}$$

where k_f^* and k_r^* are the forward and backward Arrhenius rate coefficients, respectively, α_f and α_r are the forward and backward symmetry parameters, respectively, n is the number of electrons transferred in the reaction, F is the Faraday constant, and $\Delta\Phi$ is the change in electric potential for the charged species as it transfers across the phase boundary. Substituting for α_r and performing some algebraic simplifications, equations 6.10 and 6.11 will yield a Butler-Volmer equation for the Faradaic current density:

$$i_F = i^0\left[\exp\left(\frac{\alpha_f n_{elec} F\, \eta}{\overline{R}\, T}\right) - \exp\left(\frac{-(1-\alpha_f) n_{elec} F\, \eta}{\overline{R}\, T}\right)\right] \qquad \text{(Eq. 6.12)}$$

where i^o is the exchange-current density and can be written in the form of:

$$i_o = l_{tpb}\ k_f^{*\alpha_f} k_r^{*\alpha_r} \prod_k \left[X(k)\right]^{\nu_f(k)\alpha_r} \prod_j \left[X(j)\right]^{\nu_r(j)\alpha_f} \qquad \text{(Eq. 6.13)}$$

with k and j summed over all reactant and product species, respectively.

The reaction rate parameters used in this study come from a variety of sources. In order to ensure thermodynamic consistency (which is critical to the calculation of correct open circuit voltages), these kinetic parameters were used to estimate the thermodynamics of the involved surface species, as described earlier. The thermodynamics and forward reaction rate were then supplied to the simulation as input parameters. The forward and backward kinetic parameters for various reactions on an activated nickel SOFC catalyst were taken from Janardhanan & Deutschmann

[115]. The kinetics and thermodynamics for charge-transfer reactions on a Ni-YSZ anode and for reactions on a YSZ electrolyte were taken from Goodwin [69]. Finally, the rate parameters for CO2 adsorption on Ni surface were based on data by Derrouiche et al. [116]. Table 6.1 shows the CO chemical and electrochemical reactions with their corresponding rate coefficients. All reaction equations, rate parameters, and sources are listed in Table 6.2.

Table 6.1 – Thermodynamics of species at 25°C and 700°C

	$h^0_{k,25^\circ C}$ (kJ/gmol)	$s^0_{k,25^\circ C}$ (J/gmol*K)	$h^0_{k,700^\circ C}$ (kJ/gmol)	$s^0_{k,700^\circ C}$ (J/gmol*K)
Gas Phase Species				
O_2	0.0	205.15	21.77	
CO	-110.53	197.66	-89.73	233.64
CO_2	-393.51	213.79	0	267.81
H_2	0.0	130.68	19.88	165.42
H_2O	-241.83	188.83	-216.93	231.62
Ni Surface Species				
$[]_{Ni}$	0.0	0.0	17.43	30.55
O_{Ni}	-237.48	19.36	-209.16	68.66
C_{Ni}	-46.03	-1.60	-18.69	46.91
CO_{Ni}	-251.53 + $50\theta_{CO}$	127.48	-213.30+ $50\theta_{CO}$	194.02
$CO_{2,Ni}$	-419.49	123.42	-370.11	208.01
H_{Ni}	-40.61	28.33	-13.23	76.25
OH_{Ni}	-214.62	75.75	-179.29	137.07
H_2O_{Ni}	-302.62	87.58	-260.28	160.92
YSZ Bulk and Surface Species				
$[]_{YSZ(b)}$	0.0	0.0	41.59	72.88
$O^{2-}_{YSZ(b)}$	-183.52	28.74	-131.04	120.37
$[]_{YSZ(b)}$	0/0	0.0	41.59	72.88
O^{2-}_{YSZ}	-183.52	28.74	-131.04	120.37
OH^-_{YSZ}	-245.73	46.20	-183.21	155.19
H_2O_{YSZ}	-291.89	49.30.	-229.70	164.97

Table 6.2 – CO chemical/electrochemical reactions and reaction rate coefficients

Reaction # and Equation		A or σ (gmol,cm,s)	β	E_{act} (kJ/gmol)	Ref
Adsorption and Desorption Reactions on Ni					
$1_{a,f}$	$H_2 + 2[]_{Ni} \rightarrow 2H_{Ni}$	0.01	0	0	[115]
$1_{a,r}$	$2H_{Ni} \rightarrow H_2 + 2[]_{Ni}$	2,545e19	0	81.21	[115]
$2_{a,f}$	$H_2O + []_{Ni} \rightarrow H_2O_{Ni}$	0.1	0	0	[115]
$2_{a,r}$	$H_2O_{Ni} \rightarrow H_2O + []_{Ni}$	3.732e12	0	60.79	[115]
$3_{a,f}$	$CO + []_{Ni} \rightarrow CO_{Ni}$	0.5	0	0	[115]
$3_{a,r}$	$CO_{Ni} \rightarrow CO + []_{Ni}$	3.563e11	0	$141.0 - 50.0\theta_{CO}$	[116]
$4_{a,f}$	$CO_2 + []_{Ni} \rightarrow CO_{2,Ni}$	0.0001	0	0	[115]
$4_{a,r}$	$CO_{2,Ni} \rightarrow CO_2 + []_{Ni}$	6.447e8	0	25.98	[115]
$5_{a,f}$	$O_2 + 2[]_{Ni} \rightarrow 2O_{Ni}$	0.01	0	0	[115]
$5_{a,r}$	$2O_{Ni} \rightarrow O_2 + 2[]_{Ni}$	4.283e23	0	474.95	[115]
Reversible Reactions on Ni Surface					
6_a	$H_{Ni} + O_{Ni} \leftrightarrow OH_{Ni} + []_{Ni}$	5.0e22	0	97.9	[115]
7_a	$H_{Ni} + OH_{Ni} \leftrightarrow H_2O_{Ni} + []_{Ni}$	3.0e20	0	42.7	[115]
8_a	$OH_{Ni} + OH_{Ni} \leftrightarrow H_2O_{Ni} + O_{Ni}$	3.0e21	0	100.0	[115]
9_a	$CO_{Ni} + []_{Ni} \leftrightarrow C_{Ni} + O_{Ni}$	1.354e22	-3.0	$116.12 - 50.0\theta_{CO}$	[115]
10_a	$CO_{Ni} + O_{Ni} \leftrightarrow CO_{2,Ni} + []_{Ni}$	2.0e19	0	$123.6 - 50.0\theta_{CO}$	[115]
Adsorption, Desorption and Surface Reactions on YSZ					
1_e	$H_2O + []_{YSZ} \leftrightarrow H_2O_{YSZ}$	0.01	0	0	[69]
2_e	$O^{2-}_{YSZ(b)} + []_{YSZ} \leftrightarrow []_{YSZ(b)} + O^{2-}_{YSZ}$	5.0e11	0	83.91	This work
2_{ct}	$2OH^-_{YSZ} \leftrightarrow O^{2-}_{YSZ} + H_2O_{YSZ}$	5.0e21	0	50.0	This work
Charge Transfer Reactions at Ni/YSZ TPB					
1_{ct}	$H_{Ni} + O^{2-}_{YSZ} \leftrightarrow []_{Ni} + OH^-_{YSZ} + e^-_{Ni(b)}$	1.0e14	0	90.0 $\beta_f = 0.5$	[69]
2_{ct}	$H_{Ni} + OH^-_{YSZ} \leftrightarrow []_{Ni} + H_2O_{YSZ} + e^-_{Ni(b)}$	1.0e14	0	90.0 $\beta_f = 0.5$	[69]
3_{ct}	$CO_{Ni} + O^{2-}_{YSZ} \leftrightarrow CO_{2,Ni} + []_{YSZ} + 2e^-_{Ni(b)}$	2.5e12	0	71.0 $\beta_f = 0.5$	This work

By having the reaction rate coefficients from Table 6.2, the rate constant of each reaction can be calculated from CANTERA.

6.1.2. Solution Approach

With the general reaction equation at the anode surface, considering the Longmuir law for the surface coverage, the governing equations of surface species site fractions $\theta_{k,a}$ at the TPB of the anode side include net charge transfer reaction rates $q_{i,a}$ and diffusion from anode or electrolyte surface can be written in the form of equation 6.14.

$$\Gamma \frac{\partial \theta_{k,a}}{\partial t} = \sum_{i,a} \left(\nu_{k,i} q_{i,a} \right) + \left(\frac{l_{tpb}}{A_a} \right) D_{k,a}^{0} \Gamma \frac{\left(\theta_{k,tpb} - \theta_{k,a} \right)}{\Delta x} \qquad \text{(Eq. 6.14)}$$

Considering Longmuir law, then the open site fraction can be written in form of: $\theta_{s,a} = 1 - \sum_{k} \left(\theta_{k,a} \right)$.

In equations 6.14, $q_{i,a}$ depends on anodic overpotential which can be varied in an oscillatory manner,

$$q_{i,a} \approx l_{tpb} \left[k_{i,f}^{0} \exp\left(-\frac{\beta_f F \eta_a}{\overline{R}T} \right) \prod (\Gamma \theta_{k,a}) - k_{i,r}^{0} \exp\left(-\frac{(1-\beta_f) F \eta_a}{\overline{R}T} \right) \prod (\Gamma \theta_{k,a}) \right] \qquad \text{(Eq. 6.15)}$$

where $\eta_a = \eta_a^{*} + A_{\eta,a} \exp(j\omega t)$

The response to the oscillation can be approximated by linearization of the governing equations around the steady state point.

The governing equation of the electronic charge also provides basis for current response: $i_F = \sum_i \left(q_{i,ct} \sum_k \left(\nu_{k,i} z_k \right) \right)$ which the linearized equation around the steady state point leads to: $\Delta i_F = \sum_i \left(\Delta q_{i,ct} \sum_k \left(\nu_{k,i} z_k \right) \right)$.

From the above analysis, the governing equation for the voltage difference between the electrocatalyst and the electrolyte can be written as follows:

$$C_{dl} \frac{\partial \left(\phi_{cat} - \phi_{elec} \right)}{\partial t} = i_{ext} - F \frac{l_{tpb}}{a_{mem}} \sum_k \left(z_k \dot{s}_{k,tpb} \right) \qquad \text{(Eq. 6.16)}$$

And as it was shown in previous section, the impedance of the system can be achieved by:

$$Z_a(\omega) = \frac{\eta_a(\omega)}{\Delta i_{elec}(\omega)} \qquad \text{(Eq. 6.17)}$$

To solve all these equation in one system the boundary conditions needs to be defined. At the open circuit the net rate of the production for electrochemical and non electrochemical species are equal to zero. So this can help us to solve the rate of production equations in one system to get the coverage as well as open circuit voltage at the same time for steady state situation.

For non electrochemical reactions at steady state: $\nu_{ki} RR_i = 0$ and, for both electrochemical and non-electrochemical reaction at steady state: $\nu_{ki} RR_i + \nu_{ki} RR_i^* = 0$. Also the net amount of the charge produced must be zero: $z_k \nu_{ki} RR_i^* = 0$

Solving all these equations together will lead to steady state value of species production at open circuit.

6.2. Exploring CO Electrochemical Mechanisms with State Space Model

The suggested CO electrochemical mechanism in chapter 5 has been taken as the base for running the developed model. Although the model has not completely fit the experimental result by the time this thesis is preparing, theses result follows the trend of the electrochemical and physical models suggested in the previous chapters. Some of these results are shown here.

6.2.1. Model of *V-i* Linear Sweep Voltammetry

The anodic overpotential in the cell at each current density applied for the model is closely following the same trend as of the experimental results both for dry and wet cases. Except for the $T = 775$ °C in dry case, in most of the cases model is predicting the experimental result within a reasonable offset of <5%. This discrepancy could be due to non-charge transfer processes. The modeling result of the impedance spectra in the following gives a higher approval to this idea. Figures 6.1-a and 6.1-b show the side-by-side plots of the experimental data and model estimated data for the range of operating temperature of the cell ($T = 725 – 775$ °C) and applied current density to the cell (0 – 0.04 Amp/cm^2 of Ni).

Having close to uniform slope of the *V-i* curve at η_{anode} >0.2 V show that the charge transfer process is not affected with the offset produced by the model. The value of β calculated from the model is plotted in the Figure 6.2 and the values are with a reasonable margin of error comparable with the experimental results shown in the Table 5.3.

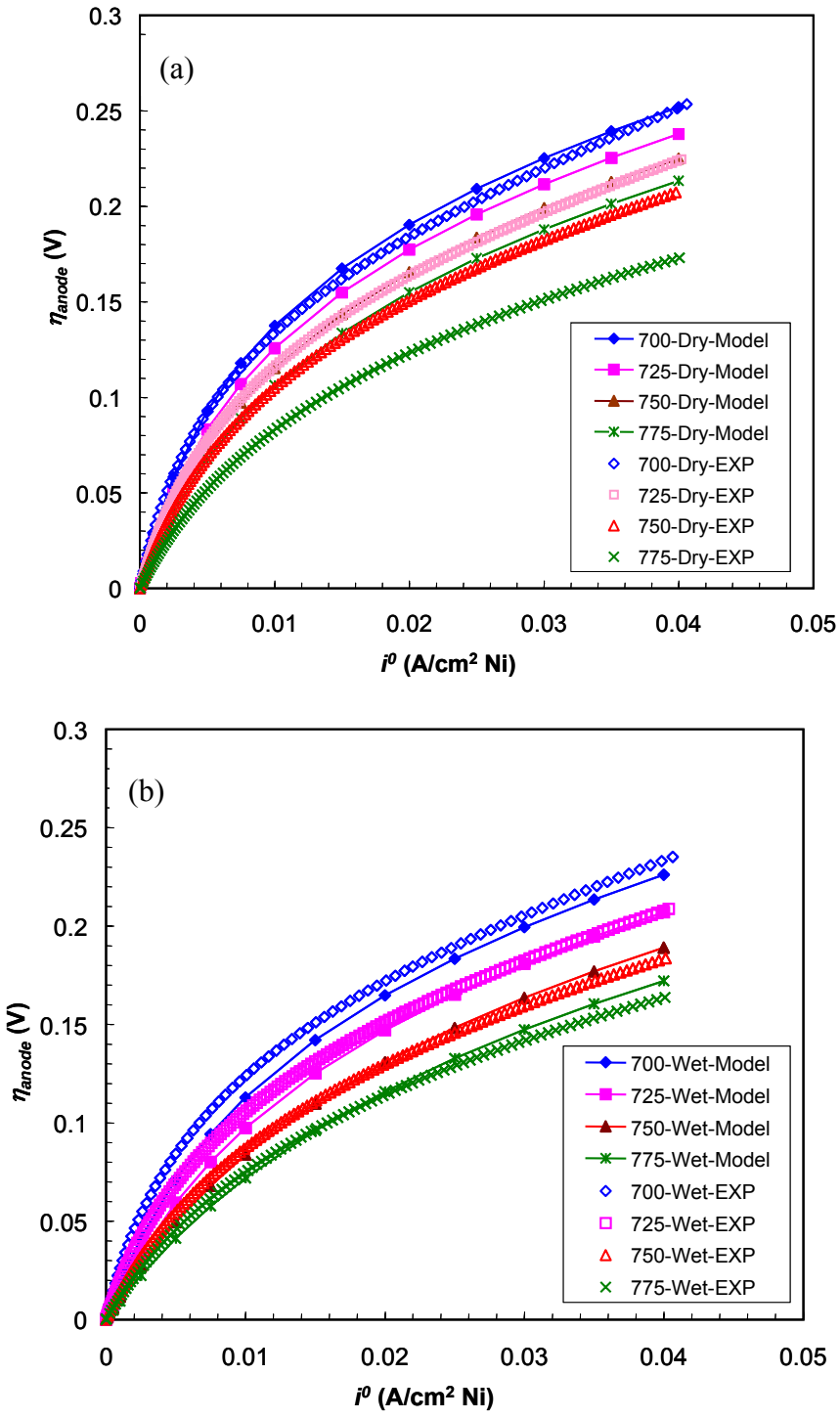

Figure 6.1 – Comparison of the *V-i* plot resulted from the model and experimental data for the range of the $T = 725 - 775$ °C under different applied current densities; a) $p_{CO} = 0.267$, $p_{CO2} = 0.067$, b) $p_{CO} = 0.260$, $p_{CO2} = 0.065$, $p_{H2O} = 0.025$.

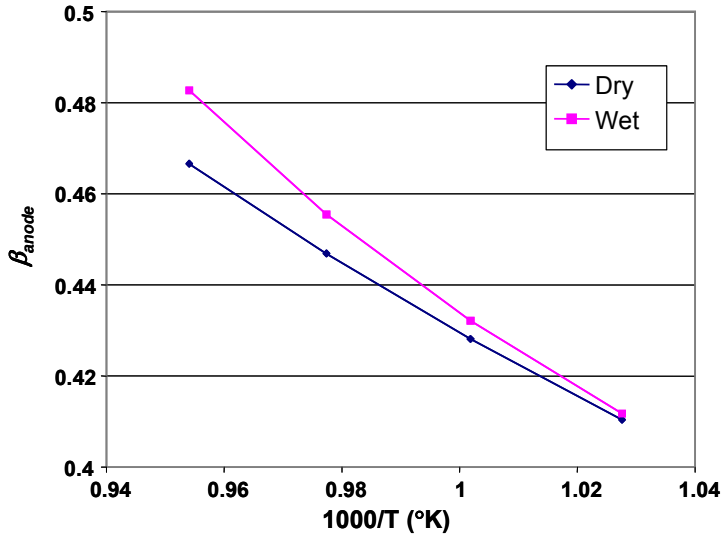

Figure 6.2 – Value of β_{anode} resulted from the modeled electrochemical reaction of the CO oxidation on the Ni surface; dry: $p_{CO} = 0.267$, $p_{CO2} = 0.067$; wet: $p_{CO} = 0.260$, $p_{CO2} = 0.065$, $p_{H2O} = 0.025$.

6.2.2. Surface Coverage of Species

As presented earlier in this chapter, the equations of the surface coverages were solved to get the steady state values of the surface coverage of all species. The coverage of the CO, CO_2 and O are shown in the Figure 6.3-a through 6.3-c for various i^0 per a_{cat}. These values are shown at the near TPB region which has been defined in the code as the region that charge transfer reaction occurs.

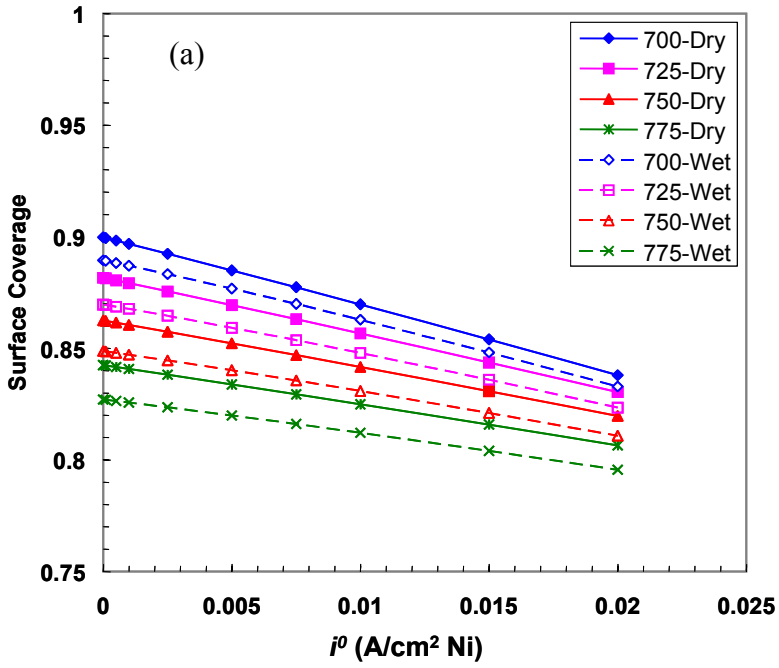
(a)
Surface Coverage
1
0.95
0.9
0.85
0.8
0.75
0
0.005
0.01
0.015
0.02
0.025
i⁰ (A/cm² Ni)
700-Dry
725-Dry
750-Dry
775-Dry
700-Wet
725-Wet
750-Wet
775-Wet

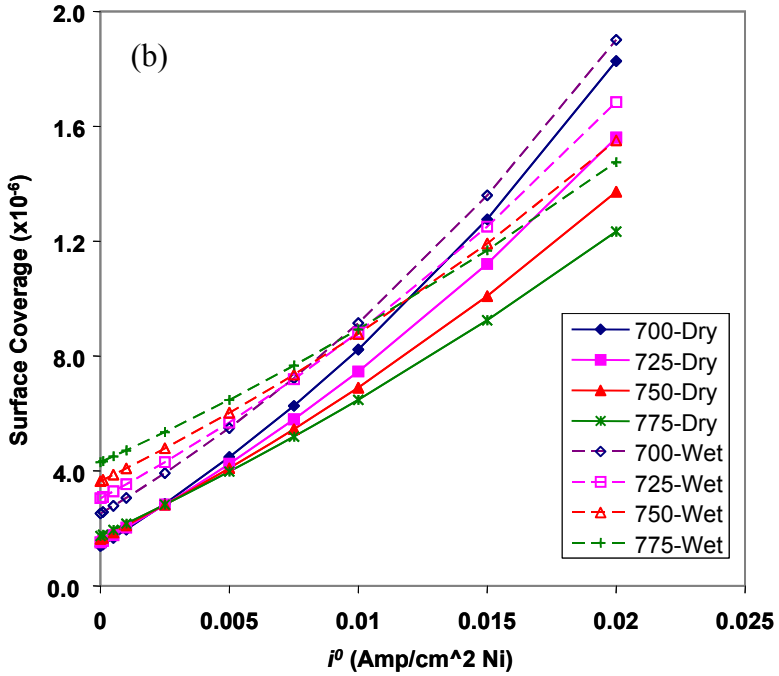
(b)
Surface Coverage (x10⁻⁶)
2.0
1.6
1.2
8.0
4.0
0.0
0
0.005
0.01
0.015
0.02
0.025
i⁰ (Amp/cm^2 Ni)
700-Dry
725-Dry
750-Dry
775-Dry
700-Wet
725-Wet
750-Wet
775-Wet

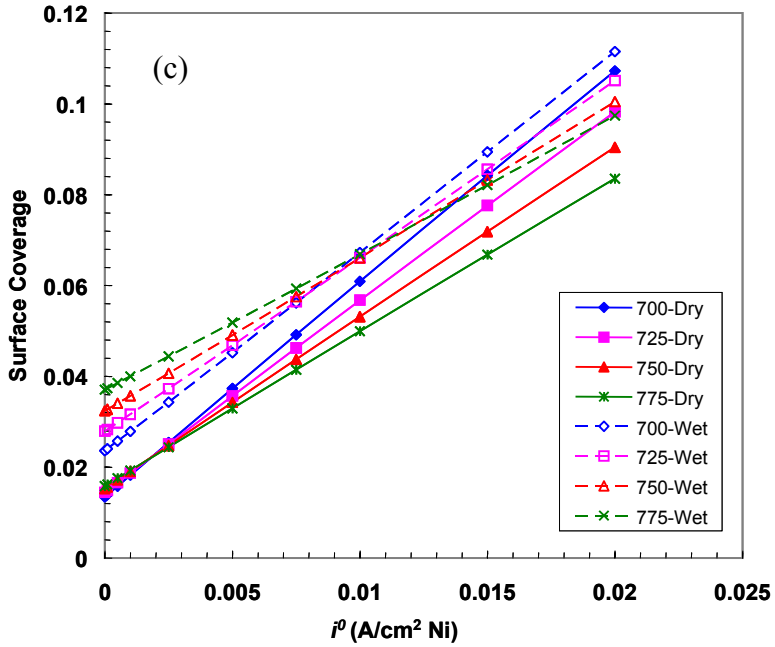

Figure 6.3 – Concentration of the surface species at the TPB region in the steady state mode while cell has undergone electrochemical reaction under different applied current densities; a) CO(Ni); b) CO_2(Ni); c) O(Ni)

Figure 6.3-a shows that the CO at the TPB drops almost linearly with the increase of the current density. This drop is steeper at lower temperature than the higher temperature for the dry cases versus the wet case, which suggests that in wet case there is possible water-gas-shift reaction happening at the surface which makes some sites to be covered with H molecules and being consumed instead of CO, while in higher temperature CO could be a consumed in wet case as fast as in dry. Figure 6.3-b confirms this fact furthermore. Since CO electrochemical oxidation is fast enough in higher temperatures, there is less time for water-gas-shift reaction at the surface so the rate of the production of CO_2 is almost linear as in rate of consumption of the CO. As the rate of reaction of CO gets slower in lower temperature, water-gas-shift reaction will help to produce more CO_2 so the rate of the production of CO_2 is no more linear. Surface coverage of O at the TPB region increases with drawing more current from

the cell which shows that when the CO sites are getting freed more O molecules will replace the free sites. The increase in surface O also is linear to the rate of current density increase.

6.2.3. Model of Electrochemical Impedance Spectroscopy

Figures 6.5-a and 6.5-b show impedance spectra from the preliminary modeling result and experimental data for the range of overpotentials of 0 to 100 mV at the T = 725 °C.

Although the impedance spectra from the model could fairly estimate the R_{CT}, the second loop seen in the result was about 6 times smaller than experimental results. It was discussed in previous chapters that this second loop is mainly in associate with either transport of species in term of surface diffusion or adsorption/desorption of the species at the surface. The fact that relaxation frequency of the charge transfer process in the model was about one order of magnitude higher than the experimental result may cause the above mentioned difference between the second loops in impedance spectra. This means that the model could be dominated with the higher frequency mode and will not be able to capture the processes happening with the lower relaxation frequencies.

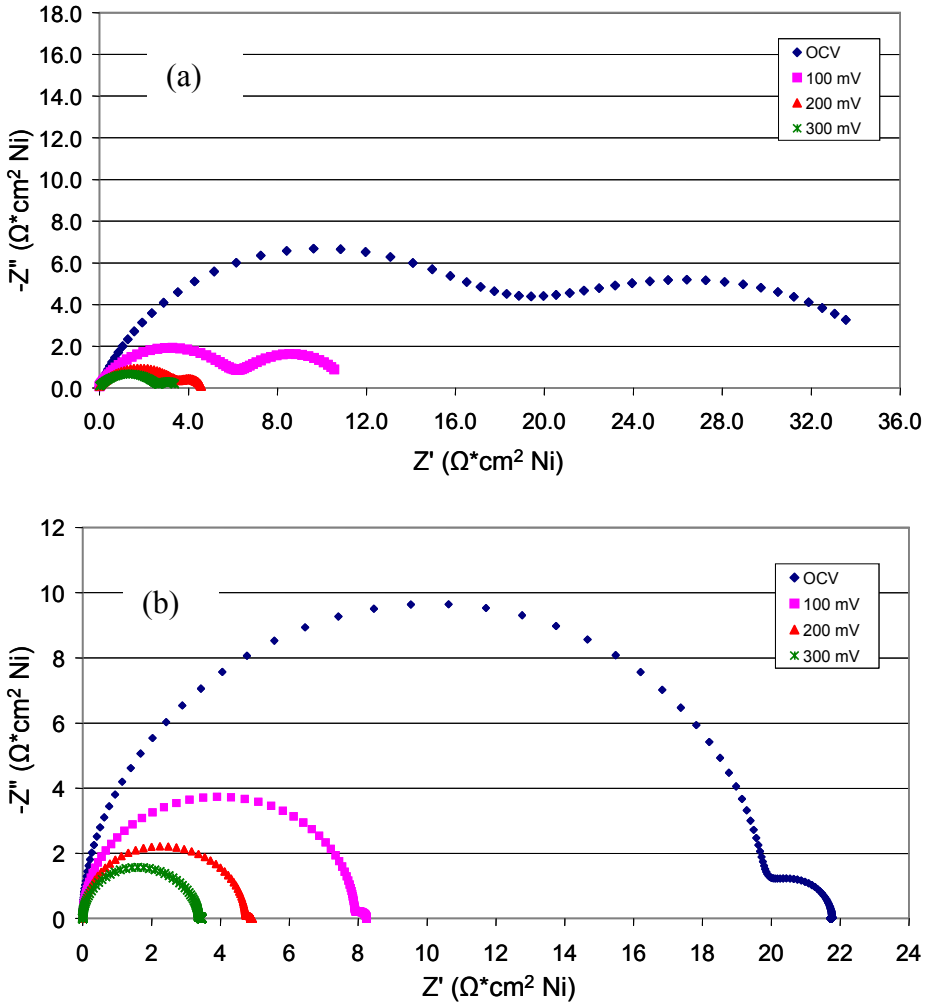

Figure 6.4 – Impedance spectra of MEA 12 at T = 725 °C and different η_{tot} p_{CO} = 0.267, p_{CO2} = 0.067; a) Experimental data; b) Model result.

The other difference which can be seen between the experimental and modeling result is the more suppressed semicircles in the experimental data which refers to the bigger values of "*n*" in the CPE element as in the equivalent circle. This could be due to the effect of considering the double layer as a pure capacitance and it needs to be more explored by replacing the C_{dl} by a CPE.

7. Conclusions

Ni patterned anode where sputtered on the surface of the single crystal YSZ disc to form a single cell SOFC. The goal of the study was to address the CO chemical/electrochemical reaction at the surface of the Ni anode on the SOFC by enforcing the electrochemical reaction happening within the bounded region of interest, i.e. TPB, in the determined pattern geometry. To achieve the goal several step were taken. The first step was to build structurally stable patterns that can tolerate the working condition including the high working temperature; being exposed to different chemical species, some corrosive like CO; and undergoing electrical and chemical reaction. In addition to the working environment, the cell was needed to bear the working conditions for days, while the experiments where doing. The next step before focusing on the CO electrochemical oxidation was to reproduce some results of the previously well-experimented H_2 as of basis of the comparison.

After fulfilling these steps the next stage was to arrange series of experiments to address the CO electrochemical oxidation on the surface of the Ni in SOFC's. Table 7.1 summarized the range of the parameters and variables that CO electrochemical experiments have been performed under.

Table 7.1- Summary of the working conditions for the CO electrochemical oxidation experiments reported in chapter 6

Parameter	Range of variation	Purpose of the experiment
Width of the pattern (μm)	10 – 25 – 50 – 100	▪ To investigate the geometrical effects including l_{TPB}, a_{Ni}, a_{YSZ}, a_{elec} ▪ To understand the diffusion length and TPB regions
Cell working temperature, T, (°C)	700 to 775	To understand the dependency of each process to temperature and calculated the activation barriers
Cell overpotential, η_{cell}	0, 100, 200, 300	To understand the possible charge transfer reaction and effect of applied voltage on each processes
Fuel partial pressure (bar)		To understand the possible surface diffusion barriers
Partial pressure of water, (bar)	0 and ~0.03	To investigate the effect of humidity in surface water-gas-shift reaction

After performing all the designed experiments, several tools were developed to achieve the desired physical parameters such as activation energy barriers, charge transfer coefficients and rate of the proposed reactions. These models which were capable of capturing the physics, thermodynamics and electrochemistry of the experiments are:

Equivalent Circuit Model:

By modeling the electrochemical/physical processes occurring during the CO electrochemical reaction, a tool was prepared to provide an equivalent physical meaning to each process. This model provided impedance spectra finely matching the experimental results on EIS. By means of this model important parameter such as bulk, charge transfer and polarization resistance as well as relaxation frequencies corresponding to each process could be captured.

Tafel Fit Model:

By approximating the charge transfer equation by Butler-Volmer equation, a complex model, capable of achieving activation, transport and ohmic overpotential,

was developed to fit the results of the sweep voltammetry. In addition to the calculated overpotential this model was able to provide us with very important parameters including current densities and charge transfer coefficients.

Detailed Electrochemistry Model (State Space Model):

Using the experimental results and empirical modeling of those result leaded to propose steps on CO electrochemical reaction on Ni anode which were listed in Table 6.2. A detailed electrochemistry model which developed to regenerate the experimental results based on these reaction steps was developed using a MATLAB platform and linked to CANTERA for doing the electrochemical calculations. This model is capable of producing all the data produced from the experiments and empirical models.

To conclude the CO electrochemical oxidation steps on Ni pattern anode of the SOFC, intensive experimental data, two sets of empirical models and one detailed electrochemical model provided a base to reveal the electrochemistry of the CO oxidation on the Ni surface of the SOFC's. Summary of what has been learnt from this research is listed below.

7.1. Summary of Significant Findings

Along with pursuing the goal of performing consistent and reproducible data some important knowledge were achieved. The first and the most important finding was while working under high temperatures (700 to 800 °C) a thicker anode deposition (~ 1 μm) prevents the anode of being agglomeration . Few other lessons learnt from the working with patterned Ni anode were, not to expose the Ni to pure CO for a long period of time, and not to apply high anodic overpotentials (> 0.4 mV).

By following these protocols preparing and experimenting Ni patterned anode was possible and wide range of experiments were performed with those.

The set of experiments and models were used to evaluate uncertain parameters such as surface diffusion rates and surface thermodynamics. Patterned Ni anodes have provided basis for understanding role of CO oxidation. These results and findings are listed in the bullet format in the following:

.i. Rate limiting processes primarily confined to region very near tpb.

.ii. Combination of the η_a and T play a role in the rate limiting process; at lower η_a and T both charge transfer and either of surface diffusion or adsorption processes act as rate liming processes while in higher η_a or higher T only charge transfer appears to be the rate limiting process.

.iii. Addition of H_2O to CO/CO_2 mixtures increases i for a given η_a to the reduction in low frequency (non-electrochemical) resistances.

.iv. Addition of H_2O to CO/CO_2 makes the charge transfer process faster.

.v. CO electrochemical oxidation is likely adsorption-limited on patterned anode as all resistances are impacted significantly by η_a.

.vi. 2.3% H_2O does not provide adequate boost in CO-produced current that the rate of the charge transfer to be comparable with H_2 electrochemical oxidation.

.vii. With applying higher η_a, charge transfer process happens faster while the adsorption/desorption and surface diffusion are not affected much by increased η_a.

7.2. Recommendations for Further Research

The focus of this research was revealing the CO electrochemical oxidation on *Ni* pattern anode and to address this experimental and modeling were used. Considering the limited time and budget this thesis has not studied the other simple fuels such as methane. In general the whole patterned anode study can be done for other type of fuels either isolated or as syngas, although there are more to investigate on CO electrochemical oxidation.

There are a couple of recommended research do pursue on CO oxidation on Ni patterned anode. One of the future researches could be to investigate in more detail the effect of water partial pressure to the higher level than studied in this research. This will provide more insight about the water-gas-shift reaction at the Ni surface. Conducting electrochemical experiments using 3 probes instead of 2 probes will provide more isolated anodic related result, although with patterned anode that would be a big challenge. One limitation in this research was limitation to the overpotential due to using Ni as anode. Switching from Ni to other catalysts such as Pt provides the mean to applying more overpotential and to cover the whole range of current from the open circuit to the short circuit current. By this improvement the study of the generated power densities could be also viable. The other challenging experimental setup could be to design a rig capable of doing in-situ surface spectroscopy. Having this tool will provide more information about the intermediate species on the surface. Also some more species related data could be achieved by using tagged CO or H_2O molecule specially while studying the water-gas-shift reaction at the surface. The

other recommendation is to apply very high and very low frequencies while applying EIS measurement to capture possible extra fast or slow processes.

There are some more recommendations for further modeling activities as well. To capture effects of the adsorption/desorption and surface diffusion, some further work on the mechanism involving sensitivity studies and tweaking of the surface thermodynamics particularly for YSZ surfaces will be critical for optimizing Ni/YSZ anode design for operation with CO rich streams.

Bibliography

1. Blomen, L.J.M.J. and M.N. Mugerwa, *Fuel Cell Systems Explained*. 1993, New York: Plenum Publishing Corporation. 1-2.
2. Ishihara, T., N.M. Sammes, and O. Yamamoto, *High Temperature Solid Oxide Fuel Cells Fundamentals, Design and Application*, ed. S.C. Singhal and K. Kendall. 2003, Oxford, UK: Elsevier Advanced Technology. 83-117.
3. Larminie, J. and A. Dicks, *Fuel Cell Systems Explained*. 1st ed. Vol. 1. 2000: John Wiley & Sons. 308.
4. Mizusaki, J., et al., *Kinetic Studies of the Reaction at the Nickel Pattern Electrode on YSZ in H_2-H_2O Atmospheres.* Solid State Ionics, 1994. **70/71**: p. 52-58.
5. Bieberle, A., L.P. Meier, and L.J. Gauckler, *The Electrochemistry of Ni Pattern Anodes Used as Solid Oxide Fuel Cell Model Electrodes.* Journal of The Electrochemical Society, 2001. **148**(6): p. A646-A656.
6. Manning, P.S., et al., *The Kinetics of Oxygen Transport in 9.5 mol% Single Crystal Yttria Stabilised Zirconia.* Solid State Ionics, 1997. **100**: p. 1-10.
7. Chou, Y.-S. and J.W. Stevenson, *Long-term Thermal Cycling of Phlogopite Mica-based Compressive Seals for Solid Oxide Fuel Cells.* Journal of Power Sources, 2005. **140**: p. 340-345.
8. Yang, Z., K.D. Meinhardt, and J.W. Stevenson, *Chemical Compatibility of Barium-Calcium-Aluminosilicate Based Sealing Glasses with the Ferritic Stainless Steel Interconnect in SOFCs.* Journal of the Electrochemical Society, 2003. **150**(8): p. A1095-A1101.
9. Bram, M., et al., *Deformation Behavior and Leakage Tests of Alternate Sealing Materials for SOFC Stacks.* Journal of Power Sources, 2004. **138**: p. 111-119.
10. Dongare, M.K., et al., *Synthesis and Characterization of Copper-Stabilized Zirconia as an Anode Materal for SOFC.* Solid State Ionics, 2002. **152-153**(2002): p. 455-462.
11. Kindermann, L., et al., *Chemical Interactions between La-Sr-Mn-Fe-O Based Perovskites and Yttria-Stabilized Zirconia.* Journal of American Ceramic Society, 1997. **80**(4): p. 909-914.
12. Primdahl, S., B.F. Sorensen, and M. Mogensen, *Effect of Nickel Oxide/Yttria-Stabilized Zirconia Anode Precursor Sintering Temperature on the Properties of Solid Oxide Fuel Cells.* Journal of American Ceramic Society, 2000. **83**(3): p. 484-494.
13. Knauth, P. and H. L. Tuller, *Solid-State Ionics: Roots, Status, and Future Prospects.* Journal of American Ceramic Society, 2002. **85**(7): p. 1654.
14. Proctor, I.A., A.L. Hopkin, and R.M. Ormerod, *Development of Anodes for Direct Electrocatalytic Oxidation of Methane in Solid Oxide Fuel Cells.* International Journal of Ionics, 2003. **3&4**: p. 242-247.
15. Itome, M. and A. Nelson, *Methane Oxidation over M-8YSZ and M-CeO_2/8YSZ (M=Ni, Cu, Co, Ag) Catalysts.* Catalysis Letters, 2006. **106**(1-2): p. 21-27.

16. Laosiripojana, N., W. Sangtongkitcharoen, and S. Assabumrungrat, *Catalytic Steam Reforming of Ethane and Propane over CeO_2-doped Ni/Al_2O_3 at SOFC Temperature: Improvement of Resistance toward Carbon Formation by Redox Property of Doping CeO_2.* Fuel, 2006. **85**: p. 323-332.
17. Sasaki, K. and J. Maier, *Re-analysis of defect equilibria and transport parameters in Y2O3-stabilized ZrO2 using EPR and optical relaxation.* Solid State Ionics, 2000. **134**: p. 303-321.
18. Blomen, L.J.M.J. and M.N. Mugerwa, *Fuel Cell Systems*, ed. L.J.M.J. Blomen and M.N. Mugerwa. 1993, New York: Plenum Press.
19. Poulsen, F.W., *Defect chemisty modelling of oxygen-stoichiometry, vacany concentrations, and conductivity of $(La_{1-x}Sr_x)_yMnO_{3\pm\delta}$.* Solid State Ionics, 2000. **129**: p. 145-162.
20. Souza, R.A.D. and J.A. Kilner, *Oxygen Transport in $La_{1-x}Sr_xMn_{1-y}Co_yO_{3+/-\delta}$ Pervoskites.* Solid State Ionics, 1999. **126**: p. 153-161.
21. Z. Shao, S.M.H., *A High-Performance Cathode for the Next Generation of Soid Oxide Fuel Cells.* Nature, 2004. **431**: p. 170-173.
22. Zhu, W.Z. and S.C. Deevi, *A Review on the Status of Anode Materials for Solid Oxide Fuel Cells.* Materials Science and Engineering, 2003. **A362**: p. 228-239.
23. Vassen, R., D. Simwonis, and D. Stover, *Modeling of the Agglomeration of Ni-particles in Anodes of Solid Oxide Fuel Cells.* Journal of Materails Sceience, 2001. **36**: p. 147-151.
24. He, H., et al., *Characterization of YSZ-YST Composites for SOFC Anodes.* Solid State Ionics, 2004. **175**: p. 171-176.
25. Tao, S. and J.T.S. Irvine, *Investigation of the Mixed Conducting Oxide ScYZT as a Potential SOFC Anode Material.* Journal of The Electrochemical Society, 2004. **151**(4): p. A497-A503.
26. Liu, M., et al., *Use of Metal SUlfides as Anode Catalysts in H_2S-Air SOFCs.* Journal of The Electrochemical Society, 2003. **150**(8): p. A1025-1029.
27. Lee, S.I., et al., *Cu-Co Bimetallic Anodes for Direct Utilization of Methane.* Journal of The Electrochemical Society, 2005. **8**(1): p. A48-A51.
28. Vernoux, P., E. Djurado, and M. Guillodo, *Catalytic and Electrochemical Properties of Doped Lanthanum Chromites as New Anode Materials for Solid Oxide Fuel Cell.* Jouranl of American Ceramic Society, 2001. **84**(10): p. 2289-2295.
29. Lin, Y.B., Z.L. Zhan, and S.A. Barnett, *Improving the stability of direct-methane solid oxide fuel cells using anode barrier layers.* Journal Of Power Sources, 2006. **158**(2): p. 1313-1316.
30. Laosiripojana, N., W. Sutthisripok, and S. Assabumrungrat, *Synthesis Gas Production from Dry Reforming of Methane ove CeO_2 Doped Ni/Al_2O_3: Influence of The Doping Ceria on The Resistance Toward Carbon Formation.* Chemical Engineering Journal, 2005. **112**: p. 13-22.
31. Park, S., J.M. Vohs, and R.J. Gorte, *Direct Oxidation of Hydrocarbons in a Solid Oxide Fuel Cell.* Nature, 2000. **404**: p. 265-67.

32. Sasaki, K., K. Watanabe, and Y. Teraoka, *Direct-Alcohol SOFCs: Current-Voltage Characteristics and Fuel Gas Compositions.* Journal of The Electrochemical Society, 2004. **151**(7): p. A965-A970.
33. Van-herle, J., Y. Membrez, and O. Bucheli, *Biogas as a Fuel Source for SOFC Co-Generators.* Journal of Power Sources, 2004. **127**: p. 300-312.
34. Zhou, Z.F., et al., *Direct Oxidation of Jet Fuels and Pennsylvania Crude Oil in a Solid Oxide Fuel Cell.* J. of Power Sources, 2004. **133**: p. 181-187.
35. Douvartzides, S., F. Coutelieris, and P. Tsiakaras, *Exergy Analysis of A Solid Oxide Fuel Cell Power Plant Fed by Either Ethanol or Methane.* Journal of Power Sources, 2004. **131**: p. 224-230.
36. Bebelis, S. and S. Neophytides, *AC Impedance Study of Ni-YSZ Cermet Anodes in Methane-Fuelled Internal Reforming YSZ Fuel Cells.* Solid State Ionics, 2002. **152-153**: p. 447-453.
37. Suzuki, T., et al., *Anode Supported Single Chamber Solid Oxide Fuel Cell in CH_4-Air Mixture.* Journal of The Electrochemical Society, 2004. **151**(9): p. A1473-A1476.
38. Lin, Y., et al., *Direct Operation of Solid Oxide Fuel Cells with Methane Fuel.* Solid State Ionics, 2005. **176**: p. 1827-1835.
39. Zha, S., et al., *GDC-Based Low-Temperature SOFC's Powered by Hydrocarbon Fuels.* Journal of The Electrochemical Society, 2004. **151**(8): p. A1128-A1133.
40. Chen, F., et al., *Pre-reforming of Propane for Low-temperature SOFC's.* Solid State Ionics, 2004. **166**: p. 269-273.
41. Feng, B., C.Y. Wang, and B. Zhu, *Catalysts and Performances for Direct Methanol Low-Temperature (300 to 600 C) Solid Oxide Fuel Cells.* Electrochemical and Solid-State Letters, 2006. **9**(2): p. A80-A81.
42. Assabumrungrat, S., et al., *Thermodynamic Analysis of Carbon Formation in A Solid Oxide Fuel Cell with a Direct Internal Reformer Fuelled by Methanol.* 2005. **139**: p. 55-60.
43. Van-herle, J., et al., *Process Flow Model of Solid Oxide Fuel Cell System Supplied with Sewage Biogas.* Journal of Power Sources, 2004. **131**: p. 127-141.
44. Omosun, A.O., et al., *Modelling System Efficiencies and Costs of Two Biomass-Fuelled SOFC Systems.* Journal of Power Sources, 2004. **131**: p. 96-106.
45. Wei, G.L., et al., *High-Performance Anode for H2S-Air SOFCs.* Journal of The Electrochemical Society, 2004. **2**: p. A232-A237.
46. Aguilar, L., et al., *A Solid Oxide Fuel Cell Operating on Hydrogen Sulfide (H_2S) and Sulfur-Containing Fuels.* Journal of Power Sources, 2004. **135**: p. 17-24.
47. McIntosh, S., et al., *An Examination of Carbonaceous Deposits in Direct-Utilizatin SOFC Anodes.* Journal of The Electrochemical Society, 2004. **151**(4): p. A604-608.
48. He, H., J.M. Vohs, and R.J. Gorte, *carbonaceous Deposits in Direct Utilization Hydrocarbon SOFC Anode.* Journal of Power Sources, 2005. **144**: p. 135-140.

49. Maiya, P.S., et al., *Maximizing H_2 Production by Combined Partial Oxidation of CH4 and Water Gas Shift Reaction.* Applied Catalysis A: General, 2000. **196**: p. 65-72.
50. Ihara, M., et al., *Effect of the Steam-Methane Ratio on Reactions Occuring on Ni/Yttria-Stablized Zirconia Cermet Anodes Used in Solid Oxide Fuel Cells.* J. of The Electrochemical Society, 1999. **146**(7): p. 2481-2487.
51. Bessler, W.G., J. Warnatz, and D.G. Goodwin, *The influence of equilibrium potential on the hydrogen oxidation kinetics of SOFC anodes.* Solid State Ionics, 2007. **177**(39-40): p. 3371-3383.
52. Bieberle, A. and L.J. Gauckler, *State-Space Modeling of the Anodic SOFC System Ni, H_2-H_2O/YSZ.* Solid State Ionics, 2002. **146**: p. 23-41.
53. Zhu, H., et al., *Modeling Elementary Heterogeneous Chemistry and Electrochemistry in Solid-Oxide Fuel Cells.* Journal of American Ceramamic Society, 2005. **152**(12): p. A2427-A2440.
54. Zhao, F. and A.V. Virkar, *Dependence of polarization in anode-supported solid oxide fuel cells on various cell parameters.* Journal Of Power Sources, 2005. **141**(1): p. 79-95.
55. Coutelieris, F.A., S. Douvartzides, and P. Tsiakaras, *The Importance of the Fuel Choice on the Efficiency of a Solid Oxide Fuel Cell System.* J. of Power Sources, 2003. **123**: p. 200-205.
56. Liese, E.A. and R.S. Gemmen, *Performance Comparison of Internal Reforming against External Reforming in a Solid Oxide Fuel Cell, Gas Turbine Hybrid System.* Transaction of ASME, 2005. **127**: p. 8690.
57. Nakagawa, N., H. Sagara, and K. Kato, *Catalytic Activity of Ni-YSZ-CeO_2 Anode for the Steam Reforming of Methane in a Direct Internal-Reforming Solid Oxide Fuel Cell.* J. of Power Sources, 2001. **92**: p. 88-94.
58. Vernoux, P., J. Guindet, and M. Kleitz, *Gradual Internal methane Reforming in Intermediate Temperature Solid Oxide Fuel Cells.* Journal of TheElectrochemical Society, 1998. **145**(10): p. 3487-3492.
59. Aguiar, P., D. Chadwick, and L. Kershenbaum, *Effect of Methane Slippage on an Indirect Internal Reforming Solid Oxide Fuel Cell.* Chemical Engineering Science, 2004. **59**: p. 87-89.
60. Zhu, H.Y., et al., *Anode barrier layers for tubular solid-oxide fuel cells with methane fuel streams.* Journal Of Power Sources, 2006. **161**(1): p. 413-419.
61. Holtappels, P., et al., *Reaction of CO/CO_2 Gas Mixture on Ni-YSZ Cermet Electrodes.* Journal of Applied Electrochemistry, 1998. **29**: p. 561-568.
62. Costa-Nunes, O., R.J. Gorte, and J.M. Vohs, *Comparison of the Performance of Cu-CeO_2-YSZ and Ni-YSZ Composite SOFC Anodes with H_2, CO, and Syngas.* J. of Power Sources, 2004. **141**: p. 241-249.
63. Lee, S., J.M. Vohs, and R.J. Gorte, *A Study of SOFC Anodes Based on Cu-Ni and Cu-Co Bimetallics in CeO_2-YSZ.* journal of The Electrochemical Society, 2004. **151**(9): p. A1319-A1323.
64. Goffe, R.A. and D.M. Mason, *Electrocatalytic Oxidation of Hydrocarbons on A Stabilized-Zirconia Electrolyte Employing Gold or Platinum Electrodes.* Journal of Applied Electrochemistry, 1981. **11**: p. 447-452.

65. Mizusaki, J., et al., *Preparation of Nickel Pattern Electrodes on YSZ and Their Electrochemical Properties in H_2-H_2O Atmospheres.* Journal of The Electrochemical Society, 1994. **141**(8): p. 2129-2134.
66. De-Boer, B., *SOFC ANODE - Hydrogen Oxidation at Porous Nickel and Nickel/YSZ Cermet Electrodes*. 1998, Universiteit Twente.
67. Bieberle, A., *The Electrochemistry of Solid Oxide Fuel Cell Anodes: Experiments, Modeling, and Simulation*. 2000, Swiss Federal Institute of Technolgoy: Zurich. p. 232.
68. Bessler, W.G., *A New Approach for SOFC Impedance from Detailed Electrochemical Reaction-Diffusion Models.* Solid State Ionics, 2005.
69. Goodwin, D.G. *A Pattern Anode Model With Detailed Chemistry*. in *Solid Oxide Fuel Cell IX (SOFC-IX)*. 2005.
70. Weber, A., et al., *Oxidation of H_2, CO and methane in SOFCs with Ni/YSZ-cermet anodes.* Solid State Ionics, 2002. **152-153**: p. 543-550.
71. Mizusaki, j., et al., *Kinetics of the Electrode Reaction at the CO-CO_2, Porous Pt/Stabilized Zirconia Interface.* Solid State Ionics, 1992. **53-56**: p. 126-134.
72. Lauvstad, G.O., R. Tunold, and S. Sunde, *Electrochemical Oxidation of CO on Pt and Ni Point Electrodes in Contact with an Yttria-Stabilized Zirconia Electrolyte - I. Modeling of Steady-State and Impedance Behavior.* Journal of The Electrochemical Society, 2002. **149**(12): p. E497-E505.
73. Lauvstad, G.O., R. Tunold, and S. Sunde, *Electrochemical Oxidation of CO on Pt and Ni Point Electrodes in Contact with an Yttria-Stabilized Zirconia Electrolyte - II. Steady-State and Impedance Measurements.* Journal of The Electrochemical Society, 2002. **149**(12): p. E506-E514.
74. Holtappels, P., et al., *Reaction of CO/CO_2 Gas Mixture on Ni-YSZ Cermet Electrodes.* Journal of Applied Electrochemistry, 1999. **29**: p. 561-568.
75. Matsuzaki, Y. and I. Yasuda, *Electrochemical Oxidatin of H_2 and CO in a H_2-H_2O-CO-CO_2 System at The Interface of A Ni-YSZ Cermet Electrode and YSZ Electrolyte.* Journal of The Electrochemical Society, 2000. **147**(5): p. 1630-1635.
76. Grgur, B.N., N.M. Markovic, and P.N. Ross, *The Electro-oxidation of H_2 and H_2/CO Mixtures on Carbon-Supported Pt_xMo_y Alloy Catalysts.* journal of The Electrochemical Society, 1999. **146**(5): p. 1613-1619.
77. Becker, B.P., *Nickel Patterned Anode Stability In SOFC Environments With H_2, CO and CH_4 Fuel Feeds*, in *Mechanical Engineering Departement*. 2005, University of Maryland: College Park.
78. Holtappels, P., L.G.J. de Haart, and U. Stimming, *Reaction of Hydrogen Water Mixtures on Nickel-Zirconia Cermet Electrodes I. DC Polarization Characteristics.* Journal of the Electrochemical Society, 1999. **146**(5): p. 1620-1625.
79. Laosiripojana, N. and S. Assabumrungrat, *The Effect of Specific Surface Area on the Activity of Nano-scale Ceria Catalysts for Methanol Decomposition with and without Steam at SOFC Operating Temperatures.* Chemical Engineering Science, 2006. **61**: p. 2540-2549.

80. Klein, J.M., et al., *Modeling of a SOFC Fuelled by Methane: From Direct Internal Reforming to Gradual Internal Reforming.* Chemical Engineering Science, 2007. **62**: p. 1636-1649.
81. Horita, T., et al., *Imaging of Oxygen Transport at SOFC Cathode/Electrolyte Interfaces by A Novel Technique.* Journal of Power Sources, 2002. **106**: p. 224-230.
82. Mizusaki, J., et al. in *3rd International Symposium on Solid Oxide Fuel Cells*. 1993: The Electrochemical Society Inc.
83. J.Mizusaki, et al., *Kinetic Studies of the Reaction at the Nickel Pattern Electrode on YSZ in H_2-H_2O Atmospheres.* Solid State Ionics, 1994. **70/71**: p. 52-58.
84. Bieberle, A. and L.J. Gauckler, *Reaction Mechanism of Ni Pattern Anodes for Solid Oxide Fuel Cells.* Solid State Ionics, 2000. **135**: p. 337-345.
85. Sukeshini, A.M., et al. *CO and CH_4 Electrochemical Oxidation on Ni Patterned Anodes*. in *Solid Oxide Fuel Cells IX (SOFC-IX)*. 2005: Electrochemical Society, INC.
86. Sukeshini, A.M., et al., *Electrochemical Oxidation of H_2, CO and CO/H_2 Mixtures on Patterned Ni Anodes on YSZ Electrolytes.* Journal of The Electrochemical Society, 2006. **153**(4): p. A705-A715.
87. Kim, H., et al., *Direct Oxidation of Liquid Fuels in a Solid Oxide Fuel Cell.* Journal of the Electrochemical Society, 2001. **148**(7): p. A693-A695.
88. Mogensen, M. and K. Kammer, *Conversion of Hydrocarbons in Solid Oxide Fuel Cells.* Annual Review of Material Research, 2003. **33**: p. 321-331.
89. Liu, J. and S.A. Barnett, *Operation of Anode-Supported Solid Oxide Fuel Cells on Methane and Natural Gas.* Solid State Ionics, 2003. **158**: p. 11-16.
90. Walters, K.M., et al., *Homogeneous Kinetics and Equilibrium Predictions of Coking Propensity in The Anode Channels of Direct Oxidation Solid Oxide Fuel Cells Using Dry Natural Gas.* Journal of Power Sources, 2003. **123**: p. 182-189.
91. Jiang, Y. and A.V. Virkar, *Fuel Composition and Diluent Effect on Gas Transport and Performance of Anode-Supported SOFC's.* Journal of The Electrochemical Society, 2003. **150**(7): p. A942-951.
92. Boaro, M., J.M. Vohs, and R.J. Gorte, *Synthesis of Highly Porous Yttria-Stabilized Zirconia by Tape-Casting Methods.* Jouranl of American Ceramic Society, 2003. **86**(3): p. 395-400.
93. Liu, J. and S.A. Barnett, *Thin Yttrium-Stabilized Zirconia Electrolyte Solid Oxide Fuel Cells by Centrifugal Casting.* Jouranl of American Ceramic Society, 2002. **85**(12): p. 3096-3098.
94. Hu, J.T., H. Jantunen, and A. Uusimaki, Journal of Euoropean Ceramamic Society, 2004. **24**: p. 1111.
95. Pomfret, M.B., J.C. Owrutsky, and R.A. Walker, *High-temperature Raman spectroscopy of solid oxide fuel cell materials and processes.* Journal Of Physical Chemistry B, 2006. **110**(35): p. 17305-17308.
96. Macdonald, J.R., *Impedance Spectroscopy*. 1987, New York: John Wiley & Sons, Inc.

97. Varma, R. and J.R. Selman, *Techniques for Characterization of Electrodes and Electrochemical Processes*. 1991: John Wiley & Sons, Inc.
98. Jiang, S.P. and S.P.S. Badwal, *Hydrogen Oxidation at the Nickel and Platinum Electrodes on Yttria-Tetragonal Zirconia Electrolyte.* Journal of The Electrochemical Society, 1997. **144**(11): p. 3777-3784.
99. Hirschenhofer, J.H., et al., *Fuel Cell Handbook*. 4th ed. 1998. 2-2.
100. Sidwell, R.W. and W.G. Coors. *Thermodynamic Limits of Electrical Efficiency in Hydorcarbon Fueled SOFC Using Internal Reforming*. in *Electrochemical Society - Solid Oxide Fuel Cells IX*. 2005. Quebed: Electrochemical Society, Pennington, NJ.
101. Pomfret, M.B., J.C. Owrutsky, and R.A. Walker, *High Temperature Raman Spectroscopy of Solid Oxide Fuel Cell Materals and Processes.* Journal of Physical Chemistry. B., 2006. **110**: p. 17305-17308.
102. Kundig, E.P., et al., *Binary Carbonyls of Platinum, $Pt(CO)_n$ (where n=1-4). A Comparative Study of the Chemical and Physical Properties of $M(CO)_n$ (where M = Ni, Pd, or Pt; n = 1-4).* Journal of American Chemical Society, 1973. **95**(22): p. 7234-7241.
103. Kotzian, M., et al., *Optical Spectra of Transition Metal Carbonyls - $Cr(CO)_5$, and $Ni(CO)_4$.* Journal of American Chemical Society, 1989. **111**(20): p. 7687-7696.
104. Adler, S.B., *Reference Electrode Placement in Thin Solid Electrolytes.* Journal of the Electrochemical Society, 2002. **149**(5): p. E166-E172.
105. Bessler, W.G., S. Gewies, and J. Warnatz. *Impedance Simulations of SOFC Patterned and Cermet Anodes from Detailed Electrochemical Model*. in *Solid Oxide Fuel Cells IX (SOFC-IX)*. 2005.
106. Bessler, W.G., J. Warnatz, and D.G. Goodwin, *The Influence of Equilibrium Potential on the Hydrogen Oxidation Kinetics of SOFC Anodes.* Solid State Ionics, 2007. **177**: p. 3371-3383.
107. Primdahl, S. and M. Mogensen, *Oxidation of Hydrogen on Ni/yttria-stabilized zirconia Cermet Anodes.* Journal of the Electrochemical Society, 1997. **144**(10): p. 3409-3419.
108. Raz, S., et al., *Characterization of Adsorbed Water Layers on Y_2O_3-doped ZrO_2.* Solid State Ionics, 2001. **143**(2): p. 181-204.
109. Pomfret, M.B., et al., *Structural and Compositional Characterization of Yttria-Stabilized Zirconia: Evidence of Surface-Stabilized, Low-Valence Metal Species.* Analytical Chemistry, 2005. **77**: p. 1791-1795.
110. Williford, R.E. and L.A. Chick, *Surface Diffusion and Concentration Polarization on Oxide-Supported Metal Electrocatalyst Particles.* Surface Science, 2003. **547**: p. 421-437.
111. Zhu, H. and R.J. Kee, *A General Mathematical Model for Analyzing the Performance of Fuel-cell Memberane-electrode Assemblies.* Journal of Power Sources, 2003. **117**: p. 61-74.
112. Ishchuk, V.P., et al., *Heterogeneous Exchange of Oxygen of Solid Oxide Electrolyte in Co-Co2 Atmosphere.* Kinetics and Catalysis, 1980. **21**(3): p. 528-533.

113. Etsell, T.H. and S.N. Flengas, *Overpotential Behavior of Stabilized Zirconia Solid Electrolyte Fuel Cells.* Journal of the Electrochemical Society, 1971. **118**(12): p. 1890.
114. Hassel, B.A.v., B.A. Boukamp, and A.J. Burggraaf, *Electrode Polarization at the Au, O_2 (g)/Yttria Stablized Zirconia Interface. Part I: Theoretical Cosiderations of Reaction Model.* Solid State Ionics, 1991. **48**: p. 139-154.
115. Janardhanan, V.M. and O. Deutschmann, *CFD Analysis of A Solid Oxide Fuel Cell with Internal Reforming: Coupled Interactions of Transport, Heterogeneous Catalysis and Electrochemical Processes.* Journal of Power Sources, 2006. **162**: p. 1192-1202.
116. Derrouiche, S. and D. Bianchi, *Heats of Adsorption of the Linear and Bridged CO Species on A Ni/Al_2O_3 Catalyst by Using the AEIR Method.* Applied Catalysis A: General, 2006. **313**: p. 208-217.